

Chapter 2: Principles of Drilling and Excavation

Gang Han
Global Drilling, Hess Corporation
500 Dallas St, Houston, TX, USA
Phone: (713)609-5480, e-mail: ghan@hess.com

Maurice B. Dusseault
Department of Earth and Environmental Sciences, University of Waterloo
200 University Avenue West, Waterloo, ON, Canada, N2L 3G1
Phone: (519) 888-4590, email: mauriced@uwaterloo.ca

Emmanuel Detournay
Department of Civil Engineering, University of Minnesota
500 Pillsbury Drive, S.E., Minneapolis, MN 55455
Phone: (612) 625-3043, email: detou001@tc.umn.edu

Bradley J. Thomson
Jet Propulsion Laboratory (JPL), California Institute of Technology
4800 Oak Grove Dr, Pasadena, CA 91109
Phone: (818)393.6307; email: Bradley.J.Thomson@jpl.nasa.gov

Kris Zacny
Honeybee Robotics Spacecraft Mechanisms Corp.
460 W. 34th Street, New York, NY 10001
Phone: (646)459-7812 email: zacny@honeybeerobotics.com

2.1	Introduction	3
2.2	Physical Properties of Rocks	3
2.2.1	Terrestrial rocks	3
2.2.1.1	<i>Rock Properties Related to Rock Failure and Breakage</i>	3
2.2.1.2	<i>Elastic Properties</i>	4
2.2.1.3	<i>Strength Properties</i>	7
2.2.1.4	<i>Transport Properties</i>	10
2.2.1.5	<i>Determination of Failure Related to Rock Properties</i>	11
2.2.2	Extraterrestrial Rocks	19
2.2.2.1	<i>Lunar Drill Core Samples</i>	19
2.2.2.2	<i>Mechanical Properties Inferred from Penetrometer Data</i>	21
2.2.3	Influence Factors for Rock Mechanical Properties	23
2.2.3.1	<i>Rock Lithology and Grain Size</i>	23

2.2.3.2	<i>Cement Type and Contact Patterns</i>	25
2.2.3.3	<i>Stress Level</i>	25
2.2.3.4	<i>Loading Rate</i>	28
2.2.3.5	<i>Anisotropy</i>	28
2.2.3.6	<i>Humidity or Fluid Saturation</i>	29
2.2.3.7	<i>Temperature</i>	33
2.3	Stresses and Energy in Drilling	34
2.3.1	Stress in Sedimentary Basins	34
2.3.1.1	<i>Definitions, Total and Effective Stresses</i>	34
2.3.1.2	<i>Stress Boundary Conditions</i>	36
2.3.1.3	<i>Stress Orientations</i>	38
2.3.1.4	<i>Stress Magnitude Estimation</i>	43
2.3.1.5	<i>Pore Pressures - $p_o(z)$</i>	46
2.3.1.6	<i>Typical Stress Distributions with Depth</i>	46
2.3.1.7	<i>Thermal and Pressure Effects on Reservoir Stresses</i>	52
2.3.2	Stresses around a Borehole	53
2.3.2.1	<i>Elastic Stresses around a Borehole</i>	53
2.3.2.2	<i>Elastic Stresses around a Borehole with Fluid Flow</i>	55
2.3.2.3	<i>Inelastic Stresses around a Borehole with Fluid Flow</i>	57
2.3.2.4	<i>Heating and Cooling the Borehole</i>	58
2.4	Theories of rock breakage	60
2.4.1	Percussive	60
2.4.1.1	<i>History</i>	60
2.4.1.2	<i>Pros and Cons</i>	61
2.4.1.3	<i>Physics of Rock Breakage in Percussion Drilling</i>	62
2.4.1.4	<i>Rock Failure Mechanisms during Percussion Drilling</i>	66
2.4.1.5	<i>Effect of Cutter Shapes and Interactions</i>	71
2.4.2	Rotary drilling	71
2.4.2.1	<i>Rotary Drilling with Drag Bits</i>	72
2.4.2.2	<i>Linear constraint on the drilling response</i>	78
2.4.2.3	<i>Complete Drilling Response</i>	81
2.4.3	Percussive-Rotary	85
2.4.4	Other drilling methods	85
2.4.5	Drilling Efficiency	86
2.4.5.1	<i>Index for Drilling Efficiency</i>	86
2.4.5.2	<i>Static and Dynamic Variables to Improve Drilling Efficiency</i>	87
2.5	Summary/Conclusions	91
2.5.1	Underground Rocks and Stresses	92
2.5.2	Drilling Theories	93
2.5.3	Effect of environment on the drilling	94
2.6	Acknowledgement	95
2.7	Nomenclature	95
2.8	References	96
2.7.1	Internet links	106

2.1 Introduction

Predicting the performance of drills requires analytical capabilities that accounts for the tool's characteristics, rock properties and behavior, the temperature, and other parameters. Also, it necessitates understanding the effect of the applied forces, details of the bit, and the interaction with the drilled rock. This chapter covers the principles of drilling and excavation, both analytically and experimentally, and the requirements for optimization of the drilling operation.

2.2 Physical Properties of Rocks

2.2.1 Terrestrial rocks

The vast array of terrestrial rocks can be simplified into a few basic types. One useful classification scheme is to group rocks via their mode of origin, specifically into igneous, sedimentary, and metamorphic rock types. Igneous rocks are those that solidified directly from a molten state, of which basalt is the prime example. Such rocks can be glassy if quickly cooled, or fully crystalline if allowed to cool slowly. Sedimentary rocks, in contrast, are composed of individual mineral or lithic fragments that have been transported and deposited in layers or strata. These strata have been compacted or re-cemented to form a rock-like mass. Finally, metamorphic rocks are igneous or sedimentary rocks that have altered during burial by heat and/or pressure. The original rock fabric, textures, and mineral assemblages are gradually replaced or overprinted as metamorphism progresses.

2.2.1.1 Rock Properties Related to Rock Failure and Breakage

Rock response to external loading depends not only on the level of applied loads, but also on rock properties. Based on their functionalities, there are three categories of rock properties often used in the analysis of rock behavior:

- Elastic properties such as Young's modulus, shear modulus, bulk modulus, Poisson's ratio, bulk compressibility, grain or matrix compressibility, etc. They define rock elastic deformation;
- Strength properties describing the loading limit a rock could afford and its plastic behavior. There are several strength variables such as cohesive strength, tensile strength, compressive strength, internal friction angle, etc.; and,
- Transport properties, e.g. rock porosity and permeability, describe the ability of fluid to pass through a rock.

These properties are essential for any analytical or numerical effort to describe or predict rock mechanical behavior. The reliability of their values is at least as important as the prediction method itself, if not more so. Rock properties from these categories are not independent. Often, it is found that they are related to each other either directly or indirectly. For example, rocks with high strength are likely to have high modulus, low Poisson's ratio, and low porosity. In this section, we will first describe each rock property and its connection with others; then, we will briefly discuss the two methods generally applied to determine its value.

2.2.1.2 Elastic Properties

Elastic properties, such as Young's modulus (E), bulk modulus (K), shear modulus (G), and Poisson's ratio (ν), are used to describe elastic deformation of rock under loading. For isotropic rocks in which the properties do not vary with direction, the elastic stress-strain relationship can be written as

$$\sigma_{xx} = (\lambda + 2G)\varepsilon_{xx} + \lambda\varepsilon_{yy} + \lambda\varepsilon_{zz}, \sigma_{xy} = 2G\varepsilon_{xy} \quad (2-1a)$$

$$\sigma_{yy} = \lambda\varepsilon_{xx} + (\lambda + 2G)\varepsilon_{yy} + \lambda\varepsilon_{zz}, \sigma_{yz} = 2G\varepsilon_{yz} \quad (2-1b)$$

$$\sigma_{zz} = \lambda\varepsilon_{xx} + \lambda\varepsilon_{yy} + (\lambda + 2G)\varepsilon_{zz}, \sigma_{xz} = 2G\varepsilon_{xz} \quad (2-1c)$$

where λ and G are the two independent Lamé elastic constants, and subscripts x, y, z are the three Cartesian coordinates. G is also called the shear modulus as it governs shear deformation. The engineering parameters E and ν are related to the two Lamé constants through

$$E = \frac{G(3\lambda + 2G)}{\lambda + G} \quad (2-2)$$

$$\nu = \frac{\lambda}{2(\lambda + G)} \quad (2-3)$$

Meanwhile the shear modulus (G) and bulk modulus (K) are related to Young's modulus and Poisson's ratio through

$$G = \frac{E}{2(1 + \nu)} \quad (2-4)$$

$$K = \frac{E}{3(1 - 2\nu)} \quad (2-5)$$

Their values for some typical rocks are listed in **Table 1**.

TABLE 1: Laboratory Mechanical Properties of Rocks [Lama and Vutukuri, 1978]

Rock	Location& Description	ρ (g/cm ³)	E (GPa)	G (GPa)	ν	UCS (MPa)	σ_T (MPa)	Remarks
Chalk	USA, Niobrara	1.28	1.24	3.03		0.83		Smoky Hill formation
Claystone	Idaho, Palisades Dam, USA	2.20	2.83	0.04		8.27		Weathered, porous, calcareous, montmorillonite matrix
Dolomite	Oneota, USA	2.45	43.9*	0.34*		86.9	4.41	Porous, massive, fg, 50% of fracture
	Mankato, USA		51.71		0.25	105.5	13.1 (R)	$\phi=9.5$
Gneiss	Euclides da Cunda Dam, Brazil	2.79	78.4		0.22	32.4		
	Dworshak Dam, USA	2.79	53.6*		0.34	162	6.89	Mg-fg, foliations at 45°. At 50% fract.
Granite	Grand Coulee, Wash. USA	2.61	8.96		0.11	64.81		Slightly altered
	USA	2.66	44.20	16.89		244.07		R=18.62-25.5

			27.37*	15.17*		226.15	7.10	
Limestone	Kansas City, Mo. USA	2.10	25.7		0.20	50.6		
	Quebec, Canada		77.22		0.33	293.72		
	Saligo, Mine, Tenn. USA	2.73	27.17* 30.7	11.7*	0.22* 0.28	173.0	5.52(R)	$\phi=3.4$, fg.
Mudstone	Bulgaria, Bistrica		0.55		0.28	1.41	0.15	
	Nokanam	2.35				10.8		$\phi=6.0\%$, silty
Quartz	Kans. OK. USA	2.72	1.71		0.20	328.88	33.78	$\phi=2.0\%$ secant at 50
Quartzite	Baraboo, USA	2.62	88.4		0.11	320.10	11	Massive, fg
	Rivett, Canada		10.69		0.27	78.6	10.34(R)	Fg, competent
Sandstone	Chambers, Ariz., USA	2.60	11.03		0.31	32.82		$\phi=25\%$ tan. 50%
	Bridge Canyon Dam, Ariz. USA	2.39	27.58		0.04	90.32	5.17	Ferruginous, mg. Massive, grain = 0.06-2.0mm
	Pa. USA	2.20	8.27* 16.4	4.69*	0.11* 0.27	86.9	4.1 (R)	$\phi=12\%$
	USA	#1 #2 #3	6.0*	3.2*	0.06*	71.71	3.12 (R)	$\phi=16\%$, weakly cemented, mg
			6.7*	3.2*	0.05*	55.15	5.19(R)	
			8.8*	4.4*	0.03*	53.09	5.59(R)	
Shale	Utah, USA	2.81	58.19*	26.61*	0.09*	215.81	17.24(R)	$\phi=0.9\%$
	Johathan mine, Ohio, USA	2.56	11.1*	7.9*	0.29	75.2	2.07	Kaolinite and sericite
	Saligo mine, Tenn. USA	2.30	13.44* 11.93	7.10*	0.02* 0.22	110.3	2.76(R)	Kaolinite and quartz, $\phi=1.7\%$
Shale+ Sandstone	Estancia Valley, USA		4.21		0.39	69.3		Secant at 21 MPa
Siltstone	Ala. USA +shale	2.76	53.23*	25.30*		256.48	18.62(R)	$\phi=0.8\%$
	Ala. USA + shale + sandstone	2.76	39.92	22.68		184.78	15.17(R)	$\phi=1.7\%$

Note: fg, fine grained; cg, coarse grained; mg, medium grained; *, dynamic tested; **, saturated or wet; R, test in bending; #1, #2, #3, the directions of loading.

Young's Modulus, E , is also called the “modulus of elasticity”, “tangent modulus”, or “stiffness”. It is the ratio between stress and strain when rock behaves elastically (**Figure 1**). For a linear rock, its value is a constant, and so stress and strain are related by $\sigma = E\varepsilon_a$, where σ is the axial loading stress and ε_a is the rock strain (i.e. fractional change in length) in the axial loading direction. For a nonlinear rock, the tangent modulus must be defined as

$$E = \frac{d\sigma}{d\varepsilon_a} \quad (2-6)$$

Table 1 lists some values of Young's Modulus for different rocks.

According to Voigt [1910], the Young's modulus of a “composite” rock can be approximated by:

$$\frac{1}{E_{eff}} = \frac{V_a}{E_a} + \frac{V_b}{E_b} + \frac{V_c}{E_c} + \dots \quad (2-7)$$

where V_a , V_b , V_c are the percentages of different minerals in the rock and E_a , E_b and E_c are the Young's modulus of the respective minerals. Reuss [1929] provided another method to estimate the effective stiffness of multi-minerals rock:

$$E_{eff} = V_a E_a + V_b E_b + V_c E_c + \dots \quad (2-8)$$

Voigt's average assumes uniform strain of the mineral aggregates, whereas Reuss' average assumes uniform stress or pressure in the aggregate. Therefore, the former gives the upper limit and the latter gives the lower limit, and the actual stiffness value will be somewhere between them [Lama and Vutukuri, 1978].

Poisson's ratio, ν , is defined as the ratio between the radial (or lateral) and axial (or longitudinal) strain increments during uniaxial loading, as shown in **Figure 1**:

$$\nu = -\frac{d\epsilon_r}{d\epsilon_a} \quad (2-9)$$

It varies over a wide range of possible values in rock: from 0 to 0.5 in principle. Most minerals have values in the range of 0.1-0.3, but cracks tend to lower the value of ν , while liquid saturation causes ν to increase.

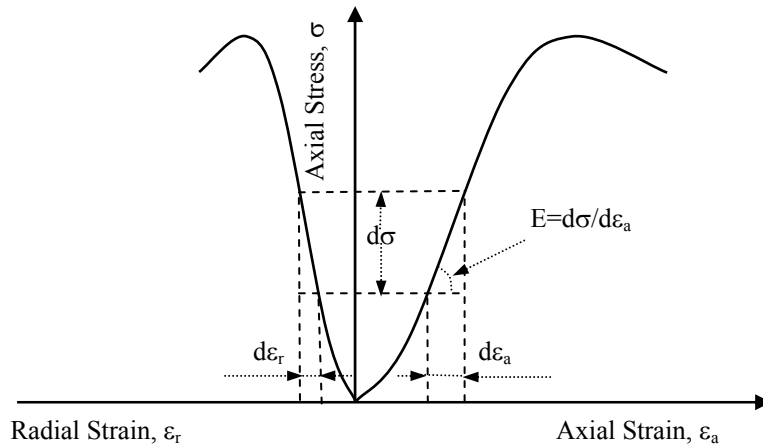


FIGURE 1: Typical rock response during a uniaxial loading test

Rock Compressibility, C , may be defined as either linear or volumetric compressibility. Volumetric compressibility is also defined as the inverse of bulk modulus (K):

$$C_b = -\frac{1}{V} \left(\frac{\partial V}{\partial P} \right)_T = \frac{1}{\rho} \left(\frac{\partial \rho}{\partial P} \right)_T \quad (2-10)$$

where V is specific volume at a given pressure P and temperature T , and ρ is the density. The negative sign indicates the compression is taken to be positive. Bulk compressibility depends on the compressibility of individual grains, pores and cracks. It could range from 0.191 GPa^{-1} for a weak formation to 0.036 GPa^{-1} for an extremely strong one [Ghalambor et al., 1994].

Shear modulus, G , is the ratio between shear stress and shear strain during elastic shear deformation. Because rock more often fails in shear mode, as a result of the difference between loading and confining stresses, it is an important parameter to quantify how much shear deformation a rock undergoes before a shear-failure plane forms (such as the one shown in **Figure 2**).

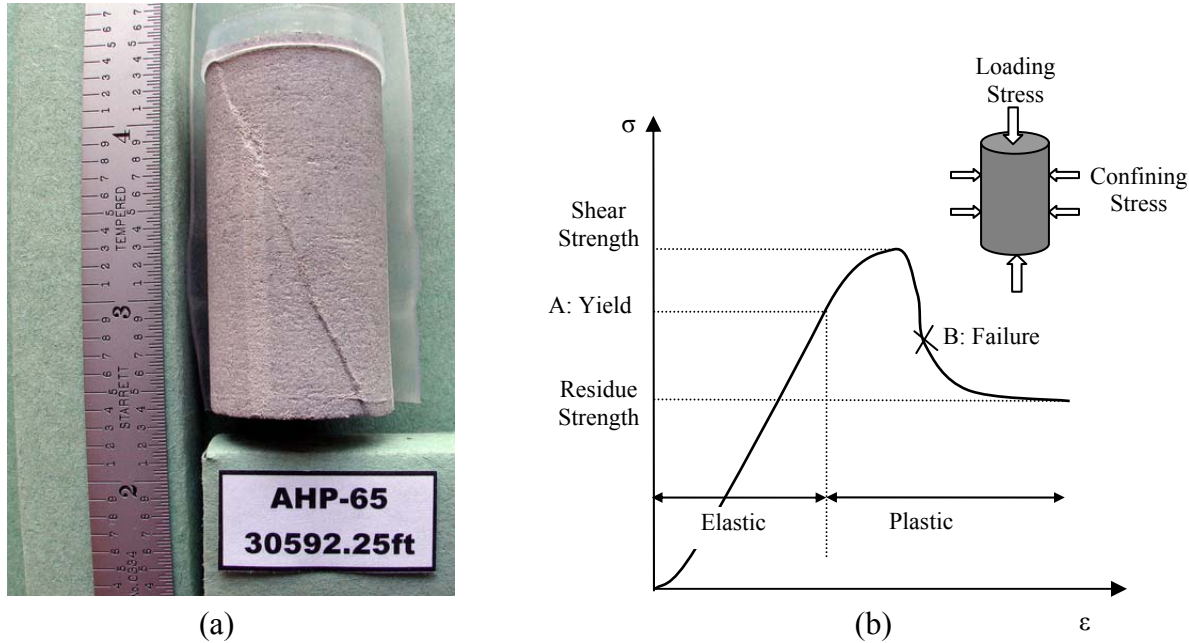


FIGURE 2: a): Failed rock sample after a triaxial test: the core is one of the deepest from Gulf of Mexico, 30592.25ft beneath a drilling platform. b): typical stress-strain response in a triaxial test

2.2.1.3 Strength Properties

When subject to external loading, rock may lose its integrity if the applied force exceeds the rock strength. This leads to rock breakage during drilling and excavation, as well as collapse of borehole, tunnel, or cavern. Rock mechanical strength is the most crucial rock property in stability analysis, and it appears in different forms: shear strength, uniaxial compressive strength (UCS), tensile strength, and residual strength.

Shear strength, also called compressive strength, is the maximum compressive stress that a rock can sustain. The resistive forces come from two contributions: one is the cohesive resistive force (cohesive strength); the other is the frictional resistive force (frictional strength). Cohesion comes from not only mineral cementation from quartz, calcareous, and ferruginous materials and cohesive bonding such as capillary force, but can also be due to the intergranular fabric, which is

an intrinsic property of the contacts among particles. This interlocking mechanism among particle grains must be overcome before grains can slide. Because mineral cements are brittle, strains leading to cohesion loss can be as small as 0.3% [Santarelli and Brown, 1989].

Figure 2a shows a sample of failed rock after a confined triaxial test. The sample is one of the deepest from Gulf of Mexico, 30592.25ft beneath a drilling platform. It is clearly shown that a shear-induced fracture diagonally extends through the sample. **Figure 2b** illustrates a typical rock mechanical response in a triaxial test, where rock is confined radially and loaded axially. Usually there are two parts of stress-strain curve showing nonlinear trends upon loading [Han et al., 2004]: when the rock is initially loaded, and it deforms elastically; when the load exceeds a certain level, and the rock starts to yield and behave plastically. At the grain scale, the initial stress increase may result in the closure of existing fractures and rearrangement of sand particles to form a denser and stiffer rock. Plastic responses such as yield (point A) and failure (point B), however, involve larger-scale behaviours such as deterioration of cementation, generation of micro-fissure arrays, and grain sliding along a macroscopic plane. Also, this response may accompany grain-scale effects such as plastic grain deformation and crushing at elevated stress level.

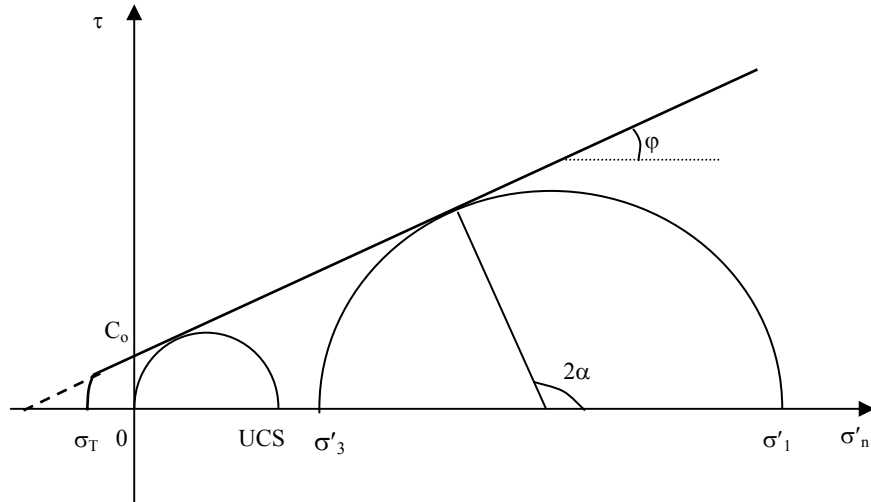


FIGURE 3: Mohr-Coulomb Failure Criteria

Various criteria have been developed to estimate the maximum loading a rock could afford in a compressional mode [Jaeger et al., 2007]. The most widely accepted empirical relationship that captures both frictional and cohesive strength factors is the “Mohr-Coulomb” (M-C) failure criterion

$$\tau = c_o + \sigma'_n \tan \varphi \quad (2-11)$$

where τ is the shear strength, φ is the internal friction angle, and c_o is the rock’s cohesive strength. The effective normal stress σ'_n is the difference between the rock total stress σ_n and the pore pressure P : $\sigma'_n = \sigma_n - \alpha P$, where α is called Biot’s poroelastic constant. In a 2D Cartesian coordinate system, the M-C criterion can be written as

$$\sigma'_1 = 2c_o \tan \beta + \sigma'_3 \tan^2 \beta \quad (2-12)$$

where σ'_1 and σ'_3 are the largest and smallest principal stresses, β is the failure angle related to the friction angle through:

$$\beta = (\pi/4) + (\varphi/2) \quad (2-13)$$

Another form of the M-C criterion is:

$$\sigma'_1 - N\sigma'_3 + S = 0 \quad (2-14)$$

where $S = -\frac{2\cos(\varphi)c_o}{1-\sin(\varphi)}$ and $N = \frac{1+\sin(\varphi)}{1-\sin(\varphi)}$.

Uniaxial Compressive Strength (UCS)

As shown in **Figure 3**, UCS is the peak stress that rock can sustain during a uniaxial compression test with no lateral confinement, i.e. when the confining stress is zero. Usually, it is treated as a benchmark for sand stability because of its ease of measurement. Rock is assumed to be more stable if its UCS is higher. **Table 1** lists some UCS values of various rocks. It can be estimated from Eq. 2-15, by setting the confining stress σ'_3 to zero:

$$UCS = \frac{2\cos(\varphi)c_o}{1-\sin(\varphi)} \quad (2-15)$$

Tensile Strength

When rock is loaded in tension, the maximum resistance to prevent rock from being pulled apart is called the tensile strength. Based on the modified Griffith criterion [Jaeger et al., 2007], the ratio between tensile strength, σ_T , and UCS is

$$UCS = 4\left(\sqrt{\mu^2 + 1} - \mu\right)\sigma_T \quad (2-16)$$

where the coefficient of friction is given by $\mu = \tan \varphi$, φ is friction angle of the Coulomb criterion (often close to 30° for sandstone). Tensile strength is generally much smaller than compressive strength, which indicates rock more easily fails in tension than in compression. Tensile strength values of some rocks are listed in **Table 1**.

Residual Strength

Another strength concept defined in **Figure 2** is rock residual strength: the strength the rock has after losing its cohesive strength component and original structure integrity. This strength is important to evaluate rock post-failure behavior.

In both crystalline igneous rocks and in sedimentary rocks, there is often a disparity between the strength of an intact rock sample and the strength of individual mineralogical constituents. Rock strength is affected by numerous internal factors, including grain size, mineral cement type, contact patterns, original cracks and fissures, anisotropy, as well as external conditions such as water saturation, stress state, loading path and so on. This leads to great difficulties in obtaining accurate rock strength data, especially for in-situ conditions.

The modulus of toughness, M_t , represents the maximum amount of energy a unit volume of rock can absorb without fracture and it can be estimated through [Bell, 1978]

$$M_t = \frac{2}{3} \times UCS \cdot \varepsilon_f \quad (2-17)$$

where ε_f is the strain at rock failure, and UCS is the Uniaxial Compressive Strength. In a lab test this energy is measured as the area under the stress-strain curve, which represents the work required to fail the test specimen.

2.2.1.4 Transport Properties

Transport properties mainly refer to rock porosity and permeability, which determine rock fluid flow conductivity. Permeability can be defined by Darcy's law,

$$k = \frac{Q\mu}{A(\Delta P / \Delta L)} \quad (2-18)$$

where Q is the volume flow rate per unit time, μ is fluid viscosity, $\Delta P / \Delta L$ is the pressure gradient in the direction of flow, and A is the cross-sectional area perpendicular to the flow direction. For viscous fluids such as oil or water flowing through the pores, the fluid tends to “stick” to the walls of the pores, developing a thin static boundary layer at the mineral surface. For gases, however, a phenomenon termed “slippage” occurs, which gives rise to an apparent dependence of permeability on pressure, known as the Klinkenberg effect.

Many approaches have been proposed to describe the relationship of permeability to porosity and other rock properties. These approaches can be classified into two categories [Dullien, 1979]: geometrical permeability models that treat fluid flow in porous media as a network of closed conduits, and statistical permeability models in which a probability law is applied. Among the geometrical models, the Carman-Kozeny model is popular because of its simplicity:

$$k = \frac{\phi^3}{5(1-\phi)^2 S^2} \quad (2-19)$$

where S is the specific surface area, defined as $S = \sqrt{\frac{\phi_i^3}{5(1-\phi_i)^2 k_i}}$, and ϕ_i and k_i are porosity and permeability under initial conditions. This model holds relatively well for unconsolidated and weakly consolidated spherical particulate assemblies, if the packing density is not too small [Le Pennec et al., 1998].

For sandstones in hydrocarbon reservoirs below the yield level during hydrostatic and nonhydrostatic loading, Holt [1990] recommended the following correlation

$$K = \frac{a^2}{45} \frac{\phi^3}{(1-\phi)^2} \quad (2-20)$$

where a is the particle radius.

However, it should be noted that permeability can easily deviate from above equations, and of course relative permeability in multi-phase cases cannot easily be based on such a relationship. For example, Davies and Davies [2001] showed there is no consistent relationship of porosity with permeability for sand samples from the Gulf of Mexico and southern California when porosity exceeds 20%. As a matter of fact, permeability is not only dependent on porosity and specific surface area, but also on the size distribution, skewness, the topographical arrangement of capillaries, and the amount and location of interstitial fine-grained minerals.

Porosity can be used as an indication of strength. In ceramics with uniform grain size, laboratory measurements show that there is a correlation between UCS and porosity (ϕ) [Sarda et al., 1993]:

$$UCS = \sigma_o \cdot e^{-\beta\phi} \quad (2-21)$$

For alumina this correlation covers the porosity range of 2-62%, and the value of β is 8 or 9 depending on the orientation of the pores with respect to the loading direction. They proposed a correlation for porosity up to 30% when quartz content varies from 48% to 99%:

$$UCS = 258 \cdot e^{-9\phi} \quad (2-22)$$

Smorodinov et al. [1970] related rock compressive strength, σ_c , with porosity ϕ or density ρ for a group of carbonate rocks (porosity between 0.11% and 37.4%):

$$\sigma_c = 2590 \times e^{-0.091\phi} \quad (2-23a)$$

$$\sigma_c = 0.88 \times e^{2.85\rho} \quad (2-23b)$$

Despite the efforts to relate rock strength with porosity, the correlations are completely empirical. In many cases it is difficult to draw any as a wide scatter in strength versus porosity exists [e.g. Plumb, 1994]. Therefore these empirical correlations should not be used unless verified with laboratory tests.

2.2.1.5 Determination of Failure Related to Rock Properties

Based on the magnitude of stress perturbation and its rate of change, strength determination can be divided into static (or experimental) methods and dynamic (or logging-derived correlation) methods. Lab and log data could be complementary to each other, if both are available, since none of them could be claimed superior than the other. The most reliable approach to determine rock strength is through triaxial tests of core samples in laboratory. However it is time-consuming and costly. The core samples are often not readily available and usually damaged to some unknown extent during coring, handling, and transporting processes.

Well logs can reflect in-situ stress conditions and provide continuous profiles that reveal the trend of formation properties. Unfortunately, since no logging tool directly yields static strength

value, dynamic methods have to face tremendous difficulties to interpret and calibrate, and “...no one should be offended by the statement that it is far from being solved, even today.” [Raaen et al., 1996].

Static method

Static methods directly measure the rock sample under laboratory conditions after cores are recovered from specific depths. In order to retrieve the maximum information of rock deformation behavior, many kinds of experiments may be implemented, e.g. uniaxial compression test, uniaxial tension test, biaxial compression test, triaxial compression test, hydrostatic test, etc.

Introduction to Rock Testing

Useful measuring of strength and deformation of rocks in the laboratory depends on having high-quality core and good technique. Although many properties are needed for fully coupled analysis, here we focus only on strength and deformation. Other properties can also be measured, such as porosity, mineral density and bulk density, coefficient of thermal expansion, transport properties such as thermal conductivity, permeability, acoustic velocities, electromagnetic properties, and so on.

Index Testing

An Index Test is a quick test carried out on rock to classify it into categories, to yield an estimate strength and stiffness, or to serve as an empirical assessment of the material response. For example, the potential response of shale to aqueous solutions of different chemistry can be empirically assessed by immersion of intact shale pieces or drill chips into prepared solutions in small beakers, and the degree of swelling or slaking after a set period of time can be noted [Dusseault et al., 1983].

Index tests should be carried out systematically on core or drill cuttings so that a consistent picture can be developed, and also for quality control and correlation to other data. Cuttings can be tested with Brinell hardness [Schmitt et al., 1994] or dispersion methods, as well as micro-acoustic measurements. Core or core fragments are usually tested by one or more of the following methods: penetration tests of various types, elastic rebound tests using a calibrated steel mandril, point load tests for strength estimates, and core scratch tests to provide a continuous strength estimate measure along the core axis.

Strength Testing

Tensile strength is difficult to measure reliably because the value is highly sensitive to the size and orientation of internal flaws (microcracks), to the nature of preparation of the rock surface, and to the state of core damage. All types of beam bending tests are suspect, direct tensile testing is too difficult, so the standard rock mechanics test of tensile strength is an indirect tensile strength measure based on compression of a disk-shaped segment of core, with a length about 40% the diameter, usually a minimum of 75 mm in diameter.

UCS – Uniaxial Compression Testing

The standard quick test of core strength is the uniaxial compression test (UCS). Cylindrical specimens of L:D ratio ~2:1 are prepared from high quality core samples so that the ends are flat,

parallel, and prepared to a specified degree of surface finish. These specimens are mounted in a compression frame and subjected to an increasing compressive load applied at a consistent specified rate so as to achieve strain-weakening in about 5 minutes (ISRM standards).

If large amounts of core are available, systematic UCS tests are carried out, partly as strength estimates, partly to help correlate with tests such as the core scratch test, and partly to help extrapolate triaxial test data on a limited number of specimens to the larger core data base. It is common practice to take the average of five (5) UCS tests from the same lithostratigraphic unit.

Shear Testing of Interfaces

There are circumstances where the shear strength along a bedding plane, a lithological interface (sand/shale interface), or a joint surface is needed. The simplest is the direct shear test without pore pressure control but with variable normal load and vertical deformation measurement (**Figure 4**).

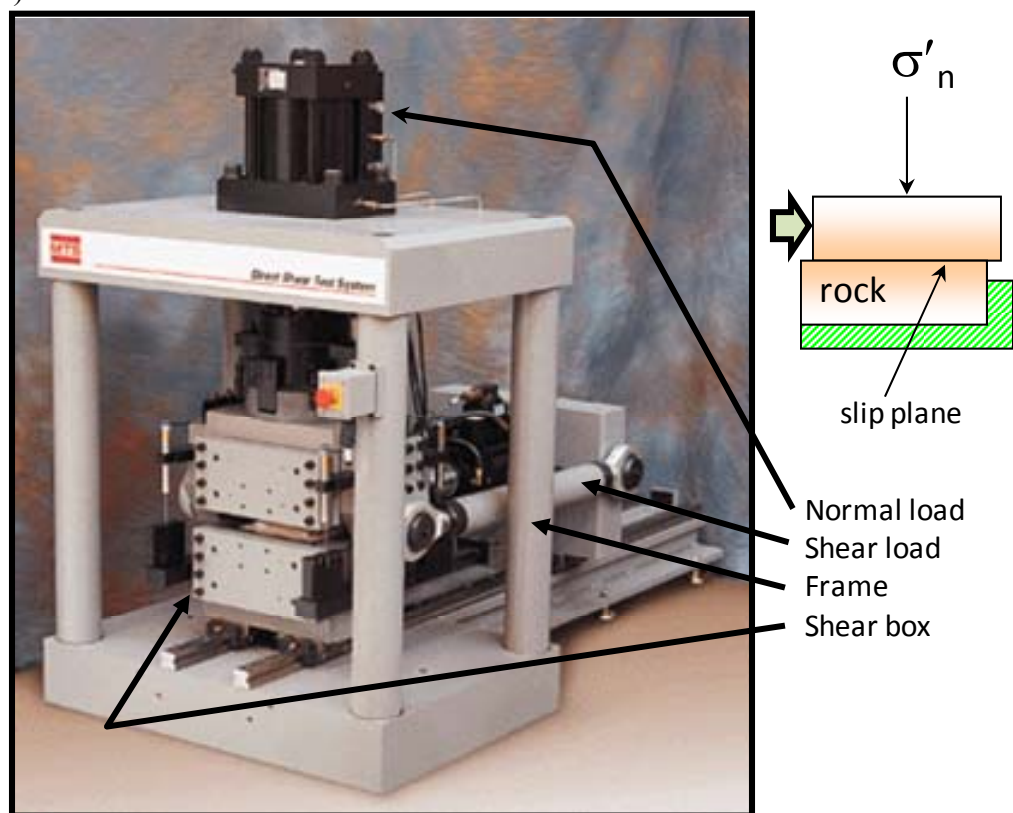


FIGURE 4: Direct shear test of a rock joint (photo MTS Labs)

The interface is prepared and mounted in a horizontally split shear box so that the interface will be at the enforced slip plane. A normal load is placed across the interface, and shear load is applied parallel to the future slip plane by a constant displacement rate of the lower half of the box. The small vertical movements at 90° to the shear direction are measured and related to the potential to dilate (or contract) during shear.

Three to five tests on “identical” specimens of the interface are preferred, but seldom possible from core. Normal effective stresses used during testing might be, for example, values of 1, 2, 4, 8 and 15 MPa. It is common to simply carry out one test at a standard chosen normal

stress, obtain peak and ultimate strengths, and use these to generate a shear yield criterion to use in analysis.

Triaxial Testing

Triaxial tests are the “gold standard” for strength and deformation; entire conferences, books and many papers exist [e.g. Donaghe et al., 1988; Paterson and Wong, 2005; ISRM website]. Three to five cylindrical specimens of L:D = 2:1 are used to determine the standard full Mohr-Coulomb yield criterion over a range of stresses. The group should be as homogeneous as feasible, given the core available. In petroleum engineering, it is common practice to subcore a 25-40 mm diameter plug from a larger core, though larger specimens are of interest if the equipment is available for reasons of scale effects. Precise volume and weight measurements are taken from each specimen, and non-destructive tests such as acoustic velocity are applied. The core chunks sawed from each end of the specimen are used for slake-dispersion behavior for shales, point load tests, oriented thin-section preparation, and other index tests.

Figure 5 shows a real cell, and **Figure 6** shows the specimen disposition and a cross section of a triaxial cell. In a cell such as shown, capabilities include full pore pressure control, axial and radial displacements for deformability, acoustic measurements, cyclic load response, and even thermal expansion to temperatures as much as 200°C.

A careful consistent methodology is followed while measuring all parameters such as resistance, expansion, and changes in velocities. Typically, the specimens are failed at 3 to 5 different values of effective confining stress, such as 0.5, 1, 3, 8 and 15 MPa. During all aspects of the test program, quality control practices are followed to assure that the outcome consists of reliable and useful data. The strength data are now considered suitable to use in design and analysis.

Deformation Properties

Deformation data are collected during triaxial tests. Pre-yield axial and radial deformation data, especially those from unload-reload cycles, are converted to values of Young’s modulus and Poisson’s ratio. Because tests are carried out at different confining stresses, the non-linear relationship $E - \sigma'_3$ can be explored as well. The elastic and strength anisotropy of shale and other anisotropic rocks is studied with specimens taken at different orientations. If the major goal of a test program is to obtain highly reliable and systematic deformability data, special test conditions and procedures may be stipulated.

The volume change behavior of sandstones can be measured through pore liquid volume monitoring in triaxial tests, but because boundary conditions in a test cell are quite different from those *in situ*, determining constrained dilation behavior for field applications is far more challenging than simple testing. Compaction behavior or laterally constrained modulus tests ($\varepsilon_x = \varepsilon_y = 0$) are carried out in one-dimensional compaction cells, which can also be used to explore permeability relationships at different strain conditions. Such testing is rarely done for drilling or borehole stability assessment. Deformation tests of shales under ionic diffusion of different species or for thermal conductivity and compressibility require special equipment modifications of uniaxial or triaxial compression cells.

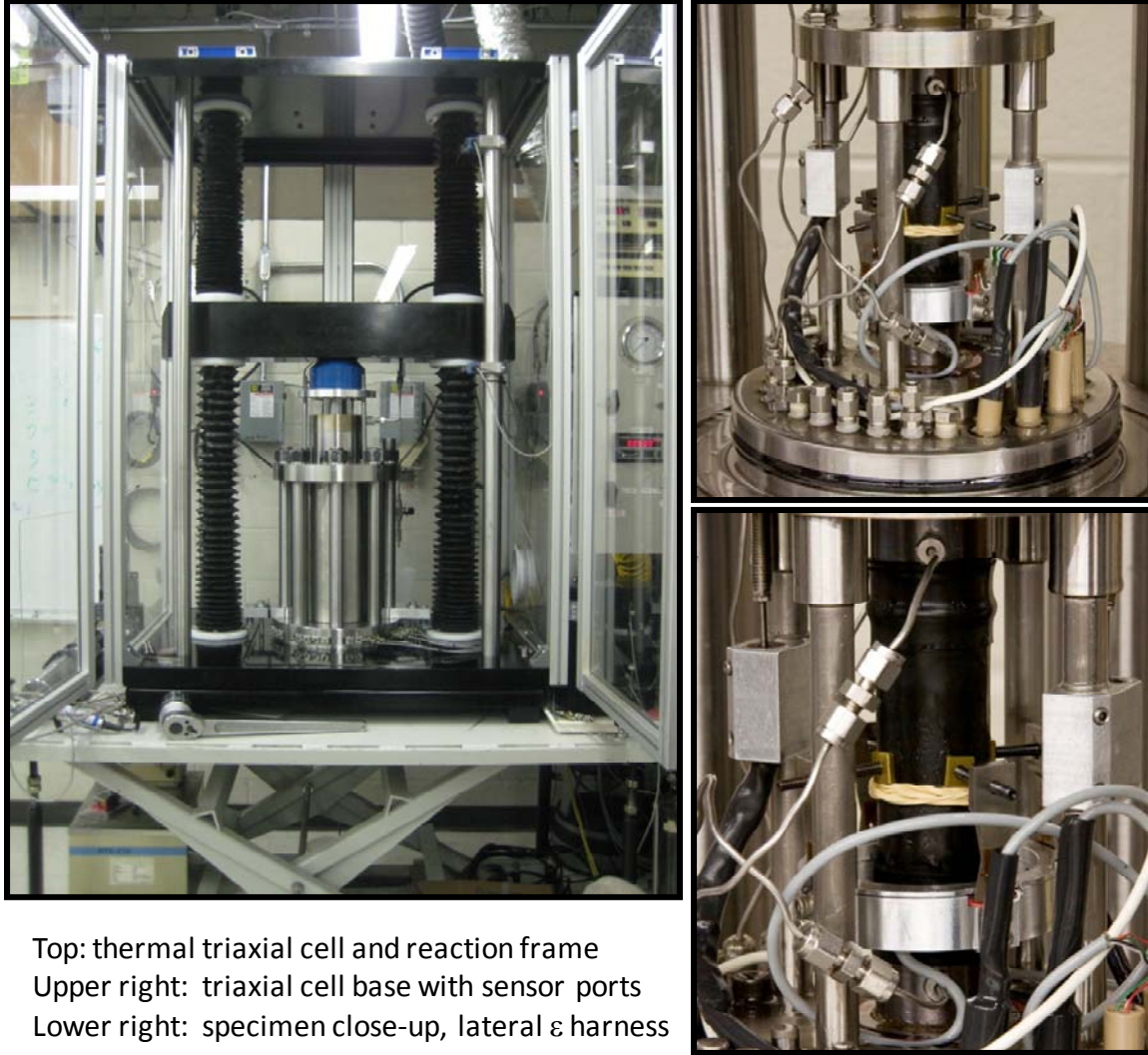


FIGURE 5: A high capability triaxial apparatus, courtesy Metarock Laboratories

Creep Tests

Salt and ductile shales exhibit time-dependent deformation when subjected to significant differential loads, even if temperatures and pressures are kept constant. Salt can squeeze into a borehole during drilling, shale can deform to cause a tight hole that traps equipment in the hole during trips to change the bit. Evaluating creep behavior over a range of temperatures and confining stresses requires special creep testing procedures and triaxial cells that can maintain constant loading for weeks, perhaps months [Dusseault and Fordham, 1994]. Cylindrical specimens are prepared with flat ends, mounted in a cell (**Figure 6**) and loaded differentially. Deformation data over time are taken for a series of tests at different stress and temperature conditions to delineate the creep behavior over the range of interest.

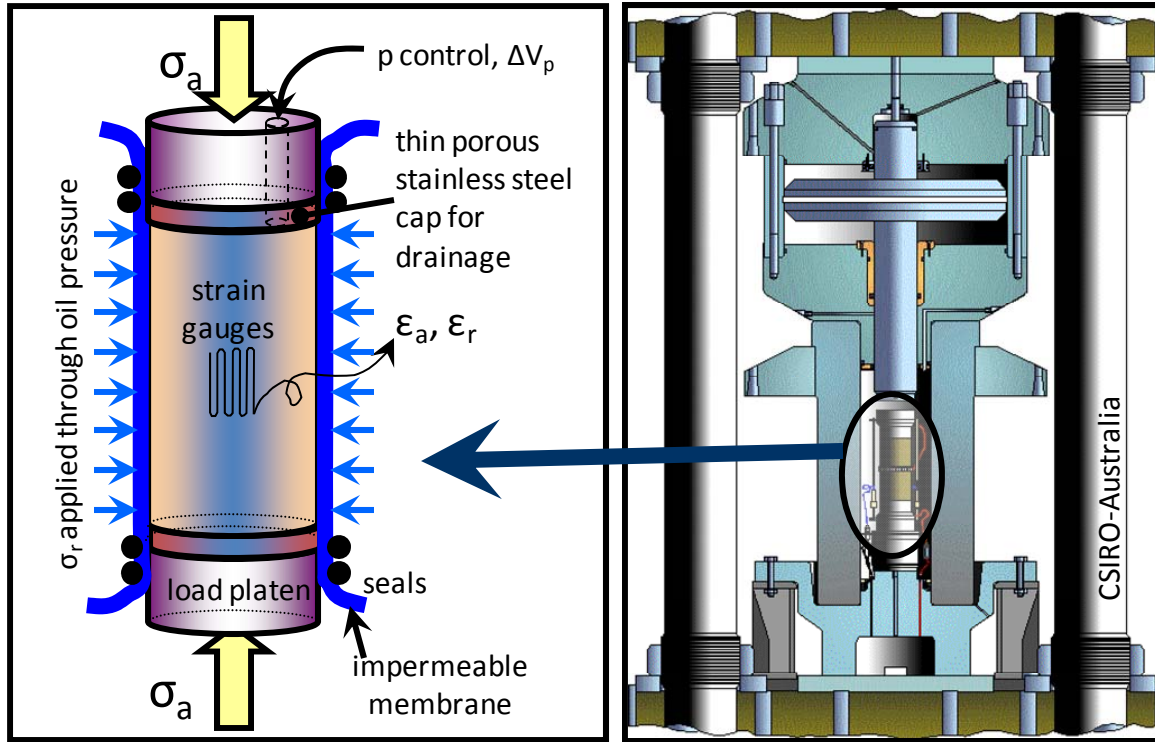


FIGURE 6: Mounted test specimen and a cross-section of a triaxial cell

Dynamic method

In oil and gas industries, elastic constants are often related to sonic compressional wave velocity, shear wave velocity, bulk density, and shale content. There are four logs usually used: gamma ray, sonic, density and neutron. Density logs give rock bulk density, while shaliness can be roughly related to the gamma ray response. A neutron-density crossplot is deployed to determine total porosity, effective porosity, and clay volume [Schlumberger, 1987]. Two types of sonic waves are focused on: a compressional wave that is most sensitive to rock density, Young's modulus, and Poisson's ratio; a shear wave that responds to rock shear modulus. Fluid saturation influences both sonic wave velocities. The high fluid saturation tends to reduce the apparent formation density, stiffness, and strength, and increase rock bulk compressibility. Hence in a multi-phase flow system introductions of a neutron log and an electrical log are also required.

The rock properties that can be inferred from logs are shear modulus, Young's modulus, bulk compressibility and Poisson's ratio. Based on acoustic travel velocities (compressional wave velocity v_c and shear wave velocity v_s) and bulk density (ρ_b), King [1969] developed the followings:

$$\text{Young's modulus: } E = \frac{\rho_b v_s (3v_c^2 - 4v_s^2)}{v_c^2 - v_s^2} \quad (2-24a)$$

$$\text{Shear modulus: } G = \rho_b v_s^2 \quad (2-24b)$$

$$\text{Poisson's ratio: } \nu = \frac{v_c^2 - 2v_s^2}{2(v_c^2 - v_s^2)} \quad (2-24c)$$

$$\text{Bulk compressibility: } C_b = \frac{1.0}{\rho_b(v_c^2 - \frac{4}{3}v_s^2)} \quad (2-24d)$$

Besides v_p and v_s used directly to determine rock elastic properties, the simple velocity ratio v_p/v_s may indicate whether formations are consolidated or unconsolidated and if gas or oil is present. Gardner and Harris [1968] showed that v_p/v_s values greater than 2.0 were characteristic of water-saturated unconsolidated sands, and values less than 2.0 indicated either a well-consolidated rock or the presence of gas in unconsolidated sand. Gregory [1976] has confirmed this conclusion, and found the ratio varies from 1.42 to 1.98 for water-saturated rocks and from 1.30 to 1.69 for gas-saturated rocks. Furthermore, the effect of increasing the gas saturation is to decrease v_p/v_s by 3 to 30 percent in consolidated rocks. Stress level was found to reduce the acoustic velocity ratio to some extent, but the effect was not always consistent or predictable over a wide range of porosity.

From Logs to Strength

Unfortunately rock strength cannot be measured by logs. However, it can be estimated based on the elastic properties interpreted from log data. Various empirical correlations have been attempted, some examples are:

- Tokle et al. [1986] combined different logs into one equation to determine the UCS:

$$\text{UCS} = a\text{GR}' + b\text{DT}' + c\text{RHOB}' + d\text{NPHI}' + e\text{CAL}' + f\text{ROK}' + \dots \quad (2-25)$$

where a, b, c, d, e, f are constants to be determined statistically by regression analysis; GR is natural gamma in API units; DT is the acoustic travel time in microsec/ft; RHOB is the bulk density in g/cc; NPHI is the neutron porosity (dimensionless); CAL is the hole caliper in inches; and ROK is a “rock number” obtained from a numerically calculated lithology log as a recombination of several other logs. The superscript, ', means those log parameters are normalized and dimensionless.

- “VOLVAN”, described by Coates et al. [1982], calculated a shear strength through

$$\sigma_c = \frac{1.125E(1 - V_{sh}) + 2.0EV_{sh}}{C_b 10^{10}} \quad (2-26)$$

while C_b is rock bulk compressibility, and shale content V_{sh} is derived through Gamma ray logs.

- Bruce [1990] calculated UCS from bulk compressibility, shear and compressive sonic velocities, and gamma ray data from a near-by well, with the gamma ray data first converted to a volume of clay log:

$$\text{UCS} = a \times 0.026 \times 10^{-6} E K_b (0.008 V_{sh} + 0.0045(1 - V_{sh})) \quad (2-27a)$$

where $a = 2\cos\phi/(1-\sin\phi)$, ϕ is internal friction angle, unit is ANSI standard. Tensile strength is calculated from:

$$T = UCS / 12 \quad (2-27b)$$

- Coats and Denoo [1981] derived shear strength from

$$\sigma_c = \frac{0.025 \times 10^6}{C_b} \times UCS \quad (2-28)$$

The sand strength UCS can be determined by using Mohr's circle analysis:

$$UCS = 0.087 \times 10^{-6} EK_b (0.008 V_{sh} + 0.0045 (1 - V_{sh})) \quad (2-29)$$

It should be noted that, since all of the currently available methods are based on empirical correlations that have been developed and calibrated to geographically limited areas, precautions should be used before trying them in a formation.

Static vs Dynamic

Rock mechanical properties derived at lab are often different from the ones from log measurements. Dynamic elastic constants are consistently higher than the static constants, especially for weak rocks and at low confining stresses. Besides core damages induced before it arrives at laboratory, which almost inevitably leads to uncertainties in lab data, the difference between static and dynamic measurements is also related to the effect of stress level, rock anisotropy, fluids, etc.

Certain mechanisms responsible for rock failure, such as the creation of shear bands, shear dilation, the crushing of grain contacts, pore collapse, etc., can only be activated with high loading force and large rock deformation. Even though these conditions could be fulfilled conveniently at lab, logging activity can only apply a much smaller dynamic load, and rock is nowhere near yield.

Many tests have witnessed the compressional and the shear wave velocities varying with increased confining stress [e.g. Morita et al., 1992]. The shear wave velocity declines at a lower stress level while the compressional wave velocity increases with higher confining stress before failure. Rock anisotropy tends to reduce as greater confining stress suppresses the onset of non-elastic behavior.

Fluid types and saturation in the cores tested in the laboratory may be quite different from the in situ conditions, which also contributes the difference between logging-derived rock properties and laboratory ones. The replacement of gas with brine substantially increases the compressional wave velocity and reduces the rate of increase with stress. Further, fluid saturation effects on compressional and shear wave velocities are much larger in low-porosity than in high porosity rocks [Gregory, 1976]. This observation is strengthened by elevated pressures but is absent at atmospheric pressure.

In some few cases, however, static data is very close to or even the same as dynamic results. For example the static and the dynamic moduli were closely in agreement if rock is at high hydrostatic confining pressures in excess of 30,000 psi [Simmons and Brace, 1965] or if a rock has very low and sparsely disseminated porosity, such as igneous rock or dense quartzite [Tixier et al., 1975].

2.2.2 Extraterrestrial Rocks

As surface exploration of neighboring planetary bodies continues to increase in scope and complexity, subsurface drilling will likely play a larger and more important role in future exploration. Drilling provides a means to retrieve samples from depths that are either impractical or impossible to obtain via other methods. In this section, we review the known physical and mechanical properties of planetary materials as determined by direct sampling and by penetrometry.

2.2.2.1 Lunar Drill Core Samples

Although information about the physical and mechanical properties of extraterrestrial materials are available from a number of different sources (including meteorites, *in situ* measurements from landed spacecraft, and inferences from remote measurements), the only returned cores from extraterrestrial drilling operations were collected by the Apollo astronauts and Soviet robotic spacecraft on the lunar surface. Lunar drill cores were collected from a total of nine locations: from the five Apollo sites (Apollo 11, 12, 14, 15, 16, and 17) and from three Luna sites (Luna 16, 20, and 24).

These drill cores provide the best estimates of the *in situ* material properties, such as bulk density, of the lunar regolith. (The traditional definition of a terrestrial soil is a mix of minerals and organics; since lunar surface material lacks organics, the term lunar regolith is preferred over lunar soil). Formed from repeated bombardment of micrometeorites over time, the lunar regolith is composed of lithic fragments, mineral fragments, and impact breccias, glasses, and agglutinates (impact glass-welded aggregate particles). Heterogeneous at all scales, the regolith is dominated by angular shards and rounded melt fragments with typical median grain diameters between about 45 to 100 μm [e.g., McKay et al., 1991 and references therein]. Some 10-20% of particles are less than 20 μm in diameter, representing a significant inhalation hazard as well as a problem for joints, seals, and other mechanical implements.

Among the most unexpected properties of the lunar regolith encountered during drilling is the degree of compaction in lower sections of the cores. Relative density (R_D) is a metric of degree of compaction relative to an idealized hexagonal close-packing arrangement of particles, with a R_D value approaching 0% corresponding to an exceptionally loose granular material and a R_D value approaching 100% corresponding to a very densely packed material [Carrier et al., 1973]. Although the parameter R_D has been superseded by the parameter maximum index density [ASTM, 2000], it nonetheless provides insight into the nature of lunar regolith. Below a depth of 10-20 cm, the lunar regolith has a relative density approaching 90% (**Figure 7a**). This value is far in excess of values found in typical terrestrial compacted soil and is attributed to the cumulative effects of shock compaction from repeated surface impact cratering [Carrier et al., 1991]. Such a high degree of compaction at depth necessitated a complete redesign of drill core collection methods used during the Apollo missions. Initially, core sampling was attempted with drive cores, which were hollow tubes physically hammered into place. Sample retrieval was difficult, and typical sample depths attained were <60 cm. Rotary drill cores were introduced in the Apollo 15 mission (**Figure 8a**), though again the high degree of compaction frustrated deep drilling. The joints between rotary drill sections were re-designed to accommodate a continuous auger (**Figure 8b**) on Apollo missions 16 and 17 (rather than a sectioned auger which prevented cuttings from escaping along the wall of the boring). In terms of bulk density, most cores average to $1.50 \pm 0.05 \text{ g/cm}^3$ for the uppermost 15 cm, and the density generally increases to $1.74 \pm 0.05 \text{ g/cm}^3$ for depths of 30 to 60 cm [Mitchell et al., 1974]. A few examples, such as the

Apollo 17 deep drill core, do not follow this trend and instead possess a dense uppermost section (**Figure 8b**). This variability highlights the heterogeneous depositional histories of the lunar regolith.

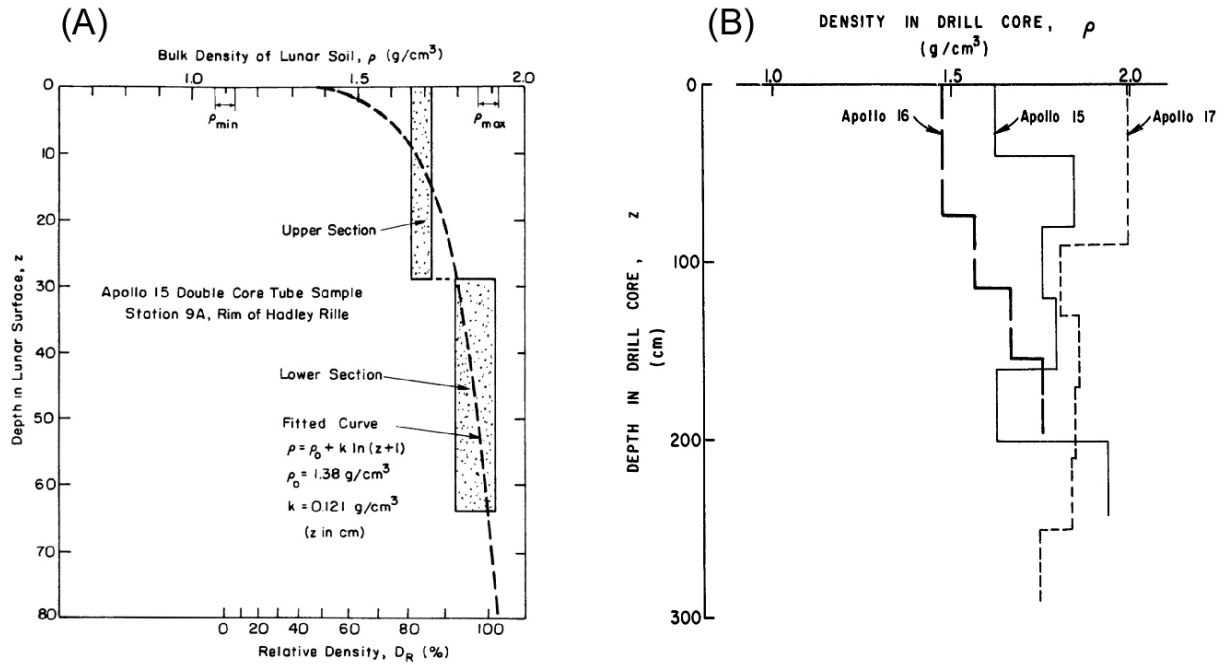


FIGURE 7: (A) Density versus depth plot for Apollo 15 drive core (samples 15010,15011). Each core tube segment is 30 cm. Lower horizontal axis is relative density (0-100%). Figure from Carrier et al. [1973]. (B) Bulk density versus depth in Apollo 15-17 drill cores [from Mitchell et al., 1974].

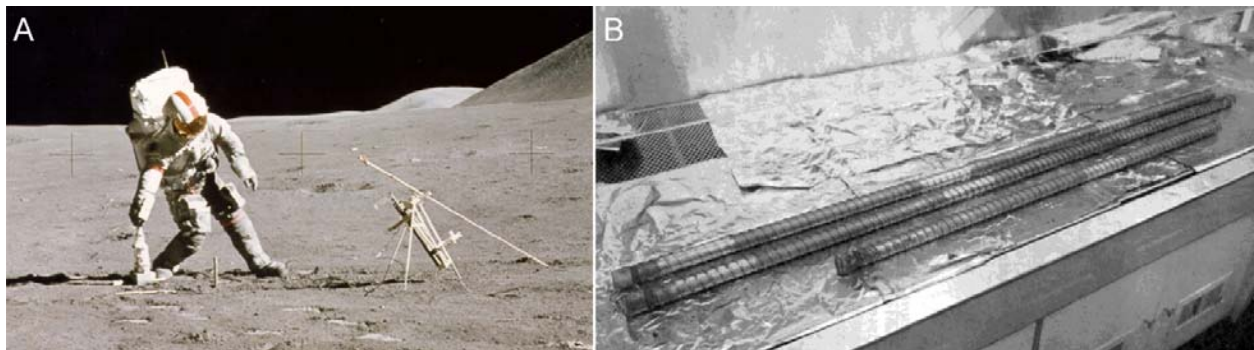


FIGURE 8: (A) Photo of Apollo 15 Commander David Scott setting up a deep drill. NASA photo AS15-87-11847. (B) Photo of Apollo 17 deep drill core in the Lunar Receiving Laboratory clean bench, NASA Johnson Space Center [from Duke and Nagle, 1974].

The longest drill core, retrieved from a depth of about 305 cm [Carrier, 1974], was collected at the Apollo 17 site. Using a rotary drill coring tube (**Figure 8b**), this sample required a drilling time of less than four minutes and attained subsurface penetration speeds of between 40-80 cm per minute [Mission Evaluation Team, 1973]. Petrologic, geochemical, and textural analyses of the core reveal it contains numerous layers and packets of layers that reflect a complex history of

depositional and excavational impact events [e.g., Taylor et al., 1979, Vaniman et al., 1979, Papike et al., 1982]. An image mosaic of a portion of the core (post-sectioning) is given in **Figure 9a**. Several measured properties of the core vary with regolith maturity, which is in turn a function of surface exposure time. For example, the intensity of the ferromagnetic resonance (I_s) is directly related to the abundance of extremely fine-grained metallic iron particles (Fe^0 , typical diameter ~ 300 Å), which are a product of micrometeorite impacts and space weathering [e.g., Morris et al., 1979]. Agglutinates are also the product of surface exposure, and the abundance of agglutinates [Taylor et al., 1979] has a high degree of covariance with the maturity parameter I_s/FeO (**Figures 9c-d**).

The manual and powered drilling conducted by the Apollo astronauts and the robotic drilling conducted by the Luna spacecraft were ultimately successful, giving us a window into the 3rd dimension, depth. The returned core samples also provide insight into the 4th dimension, i.e., time, since the regolith interacts with both the solar wind and cosmic rays in a depth-dependent manner. The experience gained during lunar surface drilling provides an invaluable guide for future drilling into planetary regolith environments, especially on atmosphereless bodies such as asteroids or the planet Mercury.

2.2.2.2 Mechanical Properties Inferred from Penetrometer Data

Although extraterrestrial drilling operations in excess of a few cm deep have yet to be conducted on bodies outside the Earth-Moon system, some inferences about the physical properties of surface materials relevant to drilling can be derived via indirect means. Perhaps the most basic physical property instrument is a surface penetrometer [e.g., Lorenz and Ball, 2001; Kömle et al., 2001]. The footpads of landed spacecraft can double as de facto penetrometers, and footpad penetration data have been returned from numerous successful soft landings. Examples include landed spacecraft on the Moon such as the Lunar Surveyor landers [Choate et al., 1968], from the Luna landers and Lunokhod rovers [Cherkssov et al., 1967; Kemurdzhian et al., 1978], from the Apollo landers [Carrier et al., 1991], and on Mars from the Viking landers [Moore et al., 1987]. Other examples of penetrometers include the arm-mounted devices on the Venera landers on Venus [Surkov et al., 1984], and a small piezoelectric sensor attached to the underside of the Huygens Probe on Titan, an icy moon of Saturn [Zarnecki et al., 2005].

When landing on unconsolidated materials, penetrometers can provide information about the surface layer properties such as cohesion and internal angle of friction. Typical lunar regolith cohesions measured via footpad penetrations were found to be in the range of 0.1 to 1.0 kPa, and the internal angles of friction ranged from 35-40° [Mitchell et al., 1974]. Given the heterogeneous nature of the lunar surface, however, it should be noted that measured values can vary greatly over short distances. On the Martian surface, several distinct types of soil-like materials were encountered with a range of strength parameters. Much of the regolith appears to be partially indurated, and disturbed indurated surfaces reveal mm to cm-sized clods or aggregates of particles (dubbed “blocky material”). Blocky material compressed by the Viking 1 Lander footpad was found to have a cohesion in the range of 5.5 to 7.1 kPa and an internal angle of friction around 30° [Moore et al., 1987]. Loose drift materials encountered by the footpads had a lower cohesion of 1.0 to 1.7 kPa and an angle of internal friction of about 20°, although the properties of fine material are non-uniquely determined in footpad penetration data due to the possible presence of hard substrates or rocks buried at depth [Moore et al., 1987].

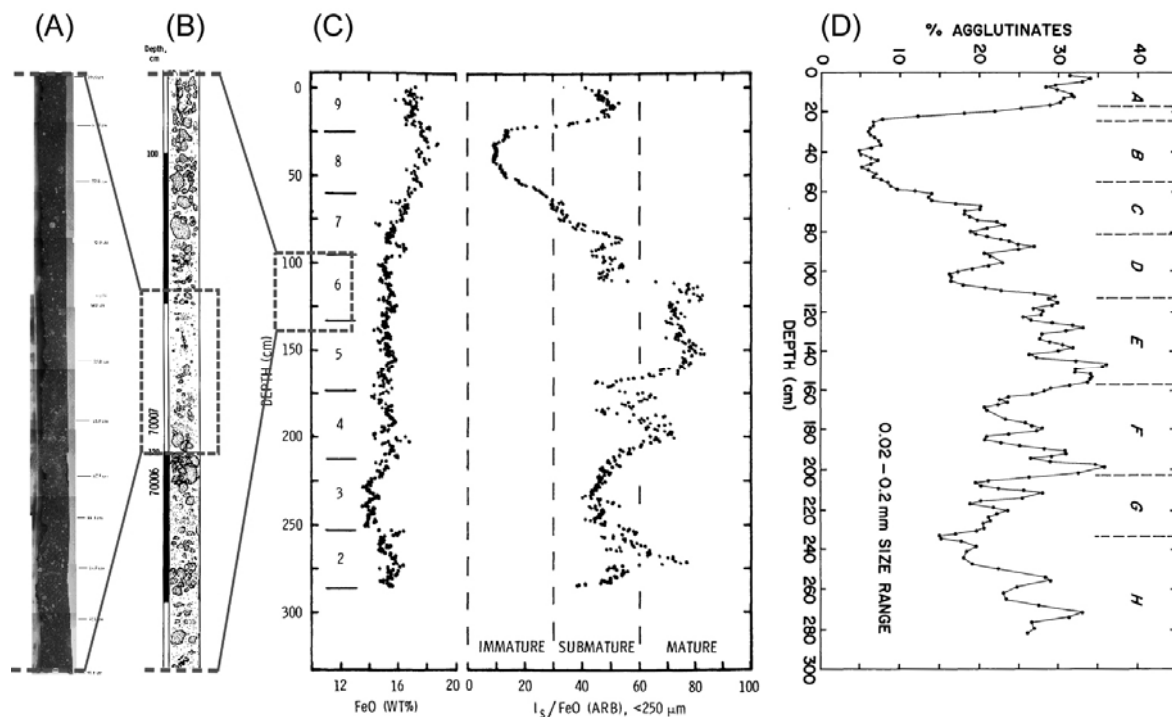


FIGURE 9: Data from Apollo 17 deep drill core (samples 70001-70009). **(A)** Mosaic of images of epoxy-encapsulated core segment (11 cm of lower portion of sample 70007; photograph courtesy C. Meyer, Johnson Space Center, 2008). **(B)** Portion of core sketch map based on X-radiography. Area given in (A) is outlined by dashed box [figure adapted from LSPET, 1973]. **(C)** Depth profiles of wt% FeO and I_s/FeO [from Morris et al., 1979]. Area given in (B) is outlined by dashed box. **(D)** Agglutinate content along the Apollo 17 drill core [from Taylor et al., 1979].

Knowledge about the *in situ* surface properties of the planet Venus are derived chiefly from Soviet Venera and Vega landers. Veneras 13 and 14 included ingenious penetrometers that consisted of a single-deployment arm mounted on the side of the spacecraft whose downward stroke served as a surface probe [Kemurdzhian et al., 1978]. Data returned from these instruments are consistent with surface material that has a load capacity of 26 to 100 kPa in the case of Venera 13 and 650-2500 kPa the case of Venera 14 [Surkov et al., 1984]. These former values are similar to terrestrial compacted sand, while the latter range is consistent with a volcanic tuff. Such low strength materials indicate that even in a volcanism-dominated planet such as Venus, surface modification processes operate to form a thin regolith layer [Basilevsky et al., 1985]. Shallow (~5 cm deep) surface drills were also employed by the Venera 13 and 14 to retrieve rock and/or soil cuttings for geochemical analyses conducted within the protected body of the landers. Reported analysis of the drill telemetry indicates that depths of penetration and motor currents are consistent with weathered porous basalt or compacted ash material similar to volcanic tuff [Surkov et al., 1984], although more detailed information about these shallow drill results are not available.

A surface penetrometer was also carried on the bottom of the Huygens probe (**Figure 10a-b**) that parachuted down through the thick atmosphere of the Saturnian moon Titan. Titan's surface is composed of water ice with a mean temperature less than 100 K. The Huygens's penetrometer

consisted of piezoelectric sensor tipped with a small (1.6 cm diameter) hemispherical knob that extended beneath the spacecraft forebody [Zarnecki et al., 2002]. Analysis of the recorded force versus penetration distance reveals an initial spike, possibly due a fracture of a surface crust or small ice pebble, followed by a region near-constant force until the rest of the Huygens craft came in contact with the surface (**Figure 10c**). This plateau region (value near 50 N over the ~2 cm projected surface area of the probe) yields a dynamic penetration resistance of 250 kPa, which is indicative of a weakly cohesive material consistent with lightly packed snow, wet sand or clay [Zarnecki et al., 2005].

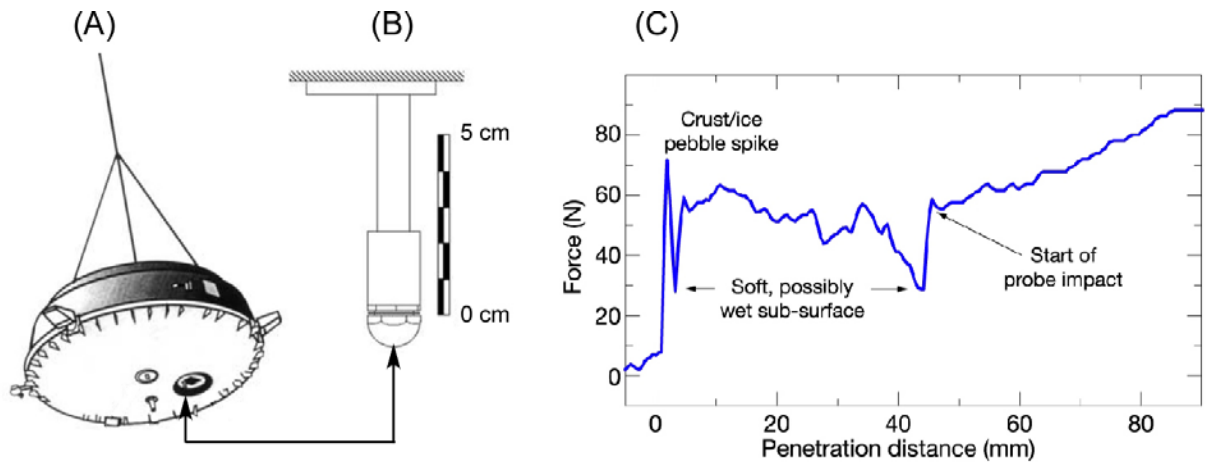


FIGURE 10: (A) Perspective diagram of the Huygens Probe in its descent configuration. Arrow points to Surface Science Package (SSP), from which penetrometer extends [from Lebreton and Matson, 2002]. (B) Diagram of penetrometer [from Zarnecki et al., 2002] (C) Recorded force versus penetration distance recorded by the Huygens' penetrometer [from Zarnecki et al., 2005].

2.2.3 Influence Factors for Rock Mechanical Properties

It is well known rock properties vary with internal and external conditions. For example, there is generally a trend of increased rock strength with depth. However it may be counteracted by local over-pressurization of the fluids resulting in reduced effective stresses and therefore less intense diagenesis, by uplifting and subsequent erosion, or by other tectonic activities. In what follows, factors that influence rock mechanical properties are discussed. These factors could be classified into two groups: intrinsic group such as grain size, cement type and contact pattern, in-situ stress level, temperature, original cracks and fissures, anisotropy, etc., and laboratory group such as specimen geometry, loading rate, coring method, and so on.

2.2.3.1 Rock Lithology and Grain Size

Rocks with different lithologies have different properties and mechanical behaviors. **Table 2** lists some properties from three rock categories, including igneous, metamorphic, and sedimentary rocks. Along with **Table 1**, it indicates that Young's modulus, rock rigidity (shear modulus) and strength of granite and siltstone are much higher than those of mudstone, claystone, sandstone and chalk. For rocks from hydrocarbon formations, shale is often stronger than sandstone while chalk from North Sea is relatively weak. Even though they are at large

formed with the same mineral, Quartz and quartzite are much stronger than sandstone, and limestone is usually stronger than chalk.

Different types of rocks have different grain size. In general, the grain size of salt is greater than that of granite, while diorite has larger grain size than does sandstone. Shale is the finest grained among the sedimentary rocks. For the sandstones from hydrocarbon formations, the grain diameter can easily be as large as 1mm, or as fine as 0.1mm. In fact, if deposit bed is in a channel gravel, pebbles larger than 2-5 mm can dominate the grain size. In general, the porosity and permeability of sands increase with larger grain size, which may lead to lower strength. Grain size distribution may also influence rock strength because a wider distribution gives tighter packing of grains and hence more contact points between grains. A denser rock pack results in higher dilatancy, which resists shear distortion.

TABLE 2: Engineering Properties of Intact Rocks [After Carmichael, 1982]

Rock type		Location	γ (N/m ³)	UCS (MPa)	v_p (Km/sec)	ν	G ($\times 10^{10}$ Pa)	E ($\times 10^{10}$ Pa)
Igneous	Granite	Woodstock, MD	2650	251	4510		2.54	5.46
		Lithonia, GA	2640	193	2710	-0.19	1.18	1.91
Metamorphic	Quartzite, ferruginous	Urals, USSR	2650	374		0.13	3.08	7
	Gneiss, granite	Mineville, NY	2750	212	3630		1.96	3.85
Sedimentary	Dolomite, siliceous	Jefferson City, TN	2770	245	5180		3.19	7.52
	Dolomite, Niagara	Unk, OH	2600	158		0.05	2.21	4.62
	Limestone	Barberton, OH	2690	197	4690		2.51	5.50
	Limestone	Ophir, UT	2780	193	5000	0.20	2.71	6.50
	Oil Shale	Rio Blanco, CO	2044	82.8		0.33		
	Quartzite	Bergstrom, TX	2610	64.5			2.76	
	Salt, diamond crystal	Jefferson Island, LA	2163	21.4			0.49	
	Sandstone, cemented ; Navajo	Huntington, UT	2880	124	2770	-0.07	0.945	1.75
	Sandstone, uncemented; Navajo	Huntington, UT	2130	55.9	2290	-0.05	0.586	1.12
	Sandstone, Carboniferous	Woodrow, PA	2150	66.9	1800	0.01	0.352	0.69
	Sandstone, Shaly; St. Peter	Omaha, NB	2344	37.3		0.05		0.719
	Shale, quartzose; mauv	Lee's Ferry, AZ	2690	123		0.08		1.65
	Shale	Ophir, UT	2810	216	4540	0.09	2.66	5.82
	Shale, siliceous	Ophir, UT	2800	231	4940	0.12	3.05	6.81
	Siltstone, Poorly cemented	Omaha, NB	2304	3.54		0.35		0.0125

Note: surface tension (γ), compressive strength (σ_c), compressional velocity (v_p), Poisson's ratio (ν), shear modulus (G), Young's modulus (E).

2.2.3.2 Cement Type and Contact Patterns

Cementation is another determinant factor affecting mechanical behavior of rock. The cemented sandstone is significantly higher than the uncemented one. Also the “carboniferous” one is about two times stronger than the “shaly” one. Since the cementation of most sandstones are to some extent a composite of different minerals, careful study should be carried on in order to better understand rock behavior as related to mineralogy.

Quartz overgrowth is a common cementing agent in sandstones. Quartz bonding between grains generally yields high strength, depending on the extent of the cementation and on its relative chemical stability. Carbonate cement can be relatively weaker than quartz cement and more reactive when contacted by unequilibrated brines. The absolute strength of carbonate-cemented sandstone, however, may be higher than a quartz-cemented one because of a higher contact area of cementing agents in the former. Also, under normal circumstance in sediments, carbonate can deposit much more rapidly than quartz because carbonate is far more soluble in water and can therefore be transported and precipitated faster.

Clay in sediments may appear different forms: if deposited after the sand matrix was formed, clay might not constitute part of load-bearing skeleton; if forms as bridges between grains, it can take part in load bearing. In the latter case, rock strength is expected to be relatively low because clay is not a strong cement and is generally sensitive to brines or geochemical changes.

Cementation texture or contact pattern mainly refers to the special arrangement of grains and cementing materials. Taylor [1950] considered two contact variations: the shape of the contact and the number of contacts per grain.

- There are five types of contact geometries classified as tangential, long, concavo-convex, sutured and floating (**Figure 11**). Usually long contacts are abundant and become more dominant with buried depth. Concavo-convex contacts are the next most popular and floating contacts are by no means uncommon.
- One grain is frequently surrounded by four others. The number of contacts shows an overall tendency to increase with depth, as porosity decreases.
- The cementation fabric also can show some hints about the rock deposit history. Ruistuen et al. [1996] indicated that their studied sandstone had undergone considerable compaction because of the fact that the grain-to-grain contacts among the particles are mainly long and concavo-convex, while extensive grain fracturing provides further evidence of compaction.

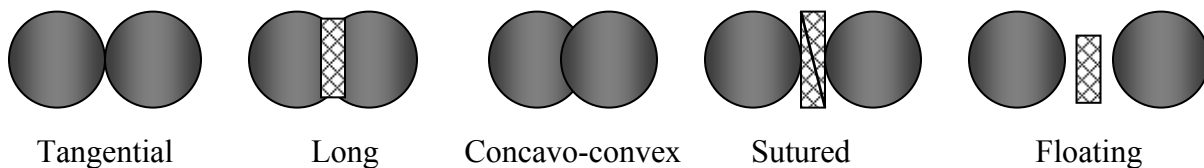


FIGURE 11: Various contact patterns between rock particles

2.2.3.3 Stress Level

As rock is buried deeper, in-situ stresses generally increase. An increasing confining stress has three effects: it increases rock compressive strength, reduces the brittle characteristics of the

stress-strain curve, and decreases the tendency to dilate [Lee and Seed, 1967]. In **Figure 12**, both rock modulus and strength increases significantly at higher confining stresses.

There are different empirical expressions for confining-stress-dependent rock stiffness when rock behaves elastically. For example, one approach widely used in soil mechanics is [Duncan and Chang, 1970].

$$E_i = K_E P_a \left(\frac{\sigma'_3}{P_a} \right)^n \quad (2-30)$$

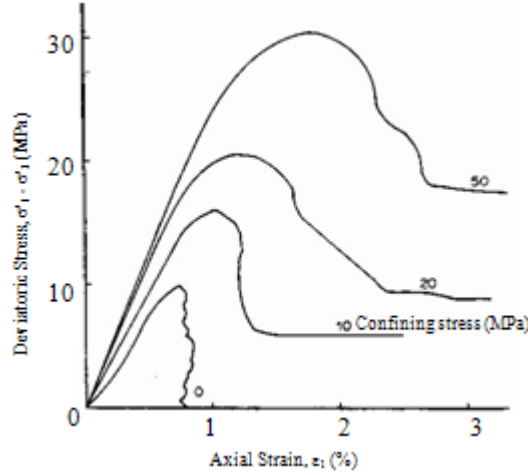


FIGURE 12: Triaxial compression tests with a sandstone at different confining stresses [after Santarelli and Brown, 1987].

where K_E is a dimensionless parameter, representing the Young's modulus E_i at atmospheric pressure P_a , and n is the exponential rate of E_i change with confining stress σ'_3 . This relationship implies that soil will lose its stiffness when the confining stress is zero. Rock, however, always retains some stiffness regardless of the level of confining stress before it is totally damaged (fragmented). Santarelli and Brown [1987] developed another empirical relation based on triaxial compression tests on carboniferous sandstones

$$E_i = E_a \left(1 + m_E \sigma_3'^{n_E} \right) \quad (2-31)$$

where E_a is the rock Young's modulus at atmospheric pressure, and m_E and n_E are constants determined from curve fitting.

The initial Poisson's ratio ν_i can be related to confining stress through a semi-logarithmic equation [Walsh and Brace, 1966]

$$\nu_i = \nu_a - D_\nu \log\left(\frac{\sigma'_3}{P_a}\right) \quad (2-32)$$

where ν_a is the rock Poisson's ratio at atmosphere pressure, D_ν is the rate of ν_i change with confining stress. This description implies that rock becomes less deformable when the confining stress increases.

It should be noted that the above descriptions only hold when rock behaves elastically. When rock starts to yield and accumulate non-reversible deformation, different correlations have been developed [Han et al., 2004].

Duncan and Chang [1970] assumed a typical triaxial stress-strain curve for sandstone fits a hyperbolic expression

$$\sigma'_1 - \sigma'_3 = \frac{A_E \varepsilon}{1 + B_E \varepsilon} \quad (2-33)$$

where A_E , B_E are constants derived from curving fitting, and their ratio A_E/B_E is the maximum stress the rock can sustain, and σ'_1 is the maximum effective stress. They related Young's modulus E to shear stress using:

$$E = \left[1 - \frac{R_f (1 - \sin \varphi) (\sigma'_1 - \sigma'_3)}{2c_o \cos \varphi + 2\sigma'_3 \sin \varphi} \right]^2 A_E \quad (2-34)$$

where C_o is rock cohesive strength; φ is friction angle; σ'_1 is the effective maximum stress; R_f is the failure ratio.

Similarly, Kulhawy and Duncan [1972] proposed the following equation for alteration of Poisson's ratio by shear damage

$$\nu = \frac{A_v}{(1 - B_v \varepsilon_1)^2} \quad (2-35)$$

where A_v , B_v are constants of a hyperbolic strain relationship, and the strain ε_1 in the direction of maximum effective stress (σ'_1) can be expressed as

$$\varepsilon_1 = \frac{\sigma'_1 - \sigma'_3}{A_E \left(1 - \frac{R_f (1 - \sin \varphi) (\sigma'_1 - \sigma'_3)}{2C_o \cos \varphi + 2\sigma'_3 \sin \varphi} \right)^2} \quad (2-36)$$

This expression indicates that Poisson's ratio increases with shear stress, and it increases faster if rock is more damaged. In other words, the rock becomes more deformable when microfractures are developed and plastic effects accumulate.

Other rock properties such as friction angle (φ) and bulk modulus (K) have been studied and their relations with confining stress are expressed in the form of [Byrne et al., 1987]

$$\varphi = \varphi_0 - D_\varphi \log\left(\frac{\sigma'_3}{P_a}\right) \quad (2-37)$$

and

$$K = K_B P_a \left(\frac{\sigma'_3}{P_a} \right)^n \quad (2-38)$$

where φ_0 is friction angle at atmosphere pressure, D_φ is the rate of φ change with confining stress, and K_B , n are constants derived from curve-fitting.

Even though the above correlations have been confirmed in the laboratory, they may not hold when other influence factors become dominant. For example, Poisson's ratio is affected by stress level, fissures, temperature, rate of loading, etc. The presence of fissures and pores decreases rock Poisson's ratio, but when fissures have a strong fabric and are oriented along the direction of applied stress, they may open up substantially with increasing axial compressive stress and lead to a large Poisson's ratio. Increase of effective confining stress lowers Poisson's ratio for weaker rocks, but for stronger rocks it may not have any influence [Lama and Vutukuri, 1978].

2.2.3.4 Loading Rate

Loading rate refers to the rate of strain change or the rate of stress change, which can be related to each other through: stress rate = strain rate \times Young's modulus, assuming the rock behaves elastically in uniaxial loading conditions. Most rock testing is carried out at a strain rate of the order of 10^{-3} s^{-1} to 10^{-4} s^{-1} . The influence of loading rate on rocks is different depending on the rock type. For sandstone, an increase in Young's modulus by 50% has been reported when the loading rate was increased from 0.18 to 0.70 MPa/s [Phillips, 1948]. Tests conducted on Berea sandstone, Barre granite, Tennessee marble, and Valder limestone showed that there is an increase in modulus with strain rate, ranging from $2.2 \times 10^{-4} \text{ s}^{-1}$ to $2.2 \times 10^{-8} \text{ s}^{-1}$, except that the modulus of Valder limestone remains almost constant [Peng, 1975]. The strain at failure increases for increased strain rate as rock strength increases. Results from norite, dolerite, Carrara marble and strong sandstone, however, show no marked effect of strain rate when it ranges from $10 \times 10^{-3} \text{ s}^{-1}$ to $10 \times 10^{-5} \text{ s}^{-1}$ [John, 1972]. For quartzite and weaker sandstone, the modulus of deformation increased slightly with increased stress rate. Lama and Vutukuri [1978] summarized "...it looks that homogeneous strong low porosity rocks showing linear elastic behavior will not be affected by increase in rate of loading, while for the others the modulus value will increase."

2.2.3.5 Anisotropy

The anisotropy of rock properties can be significant. In Tronvoll and Fjær's experiments [1993], Young's modulus, compressive strength and tensile strength were more than two times larger in the parallel-to-laminae direction, compared to those in the perpendicular direction. Also, the permeabilities tested by Holt [1990] could be as high as 1.5 Darcy in the parallel direction, while in the perpendicular direction values of only 0.1 to 0.5 Darcies were found. The main reason for the anisotropy is the stress levels at which rock forms and the origin fabric of the sediments after vertical compaction. Since the direction perpendicular to horizontal laminae tends to be the one of maximum principal stress, the grains have suffered more compaction in the vertical direction. As a consequence, there are more long and concavo-convex contacts deposited vertically, which leads to a preferable direction for rock to exhibit stronger and stiffer mechanical response.

On the other hand, the long axis of a grain is more likely deposited in the direction parallel with laminae, resulting in more cross-sectional area for fluid flow and higher permeability along the direction. Kohata et al. [1997] tested several sands and gravels, and confirmed that the elastic deformation moduli of the granular materials became more anisotropic at higher anisotropic stress (i.e. higher ratio of vertical stress to horizontal stress). Meanwhile when

granular rock is more homogeneous, there is less modulus difference in vertical and horizontal directions, which could possibly be the evidence of long-axis influence. This shows the influence of rock fabric at microscopic scale on rock behavior.

Besides microscopic anisotropy discussed above, the anisotropy due to secondary rock characteristics such as degree of weathering and presence of joints or fractures also plays an important role in rock mechanical response upon loading. For example, rock mechanical and conductivity properties in carbonate formations may be more determined by number, distribution, and characteristics of fractures, rather than rock matrix itself. Reliable description of this type of anisotropy poses more significant challenge as the rock samples at laboratory may not represent *in situ* fracture conditions.

2.2.3.6 Humidity or Fluid Saturation

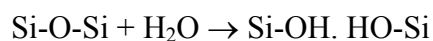
The deterioration of rock properties by adsorption (when liquid accumulates on the surface of a solid forming a thin film of molecules) or absorption (when a liquid diffuses into a solid to form a solution) is sometimes referred to as the Rehbinder effect, who in 1944 lead an extensive study into hardness reducing effects of surfactants (surface acting agents). Because most rocks are water-wet, i.e. water tends to attach to rock surface more easily than non-wetting fluids such as oil or gas, the effect of fluid saturation is also studied as that of water saturation, moisture content, humidity, etc. Many experiments have been carried out, and in summary, the results have indicated that:

- For all rock samples, strength is generally found to decrease with increased water saturation. This includes rock tensile strength, compressive strength, and UCS. The strength decrease has been reported to range from 8% [Hawkins and McConnell, 1992] to 98% [Priest and Selvakumar, 1982], depending on rock texture, mineralogy and fluid chemistry. Most of the strength decrease occurs after only a slight increase in water saturation or moisture content from the dry state [Mellor, 1971; West, 1994]. Further increases in moisture content have little effect on rock strength and elastic properties;
- The value of the friction coefficient appears to remain unaltered in many cases [Colback and Wiid, 1965];
- Young's modulus decreases with increased water saturation, sharing the same trend as rock strength [Burshtein, 1969; Gregory, 1976; Rao et al., 1987]; and,
- The behavior of Poisson's ratio is complicated; it may increase or decrease slightly before a general increase takes place at higher saturations [Hawkins and McConnell, 1992], or remain constant [Papamichos et al., 1997].

There are several possible reasons that may account for rock weakening due to fluid moisture or saturation changes [Han and Dusseault, 2002]. These include chemical reactions, capillary strength, shale swelling, etc.

Chemical reactions between water and rock solids

Water could react with various rock minerals. For example, quartz is the most common mineral in sand, and SiO₂ overgrowths are also common as cementation. Quartz hydrolysis is believed to reduce surface energy and cohesion [Swolfs, 1971]. The common mode of hydrolysis is:



The Si-O-Si bonds break up to two silanol groups: Si-OH and HO-Si. In such a hydrolyzed bridge, the hydrogen bonds are weaker by an order of magnitude than the silicon-oxygen bonds. Since all silicates have Si-O-Si or Si-O-M bridges (where M is a metal ion) that are susceptible to this type of hydrolysis, this water weakening may apply to silicates in general, e.g. feldspar, olivine, hypersthene, tourmaline and beryl [Griggs, 1967]. However, the hydrolysis occurrence highly depends on the temperature. The fact that quartz is strong below the critical temperature has motivated Griggs and Blacic [1965] to propose another model of hydrolysis, based on the assumption that "...the easy glide which occurs in the hydrolytic state can only occur when the hydrolyzed dislocation can move by exchanging hydrogen bonds with a neighboring silicon-oxygen bridge which has become hydrolyzed":

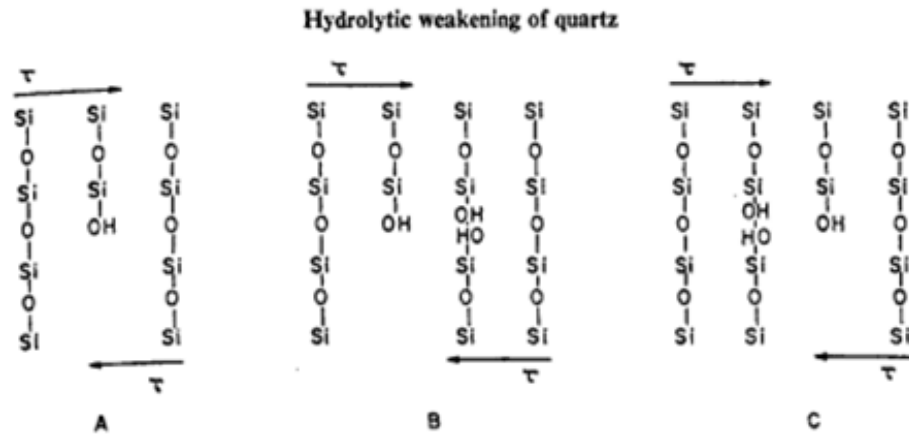
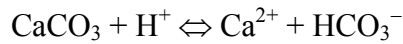
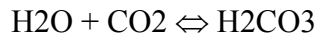


FIGURE 13: Frank-Griggs Model of Hydrolysis [Griggs and Blacic, 1965]

For calcareous cementitious rocks, the possible reactions with water are carbonate dissolution:



where H^+ may originate from:



In the normal pH range of formation water (e.g. pH=5-8), dissolved iron is present as Fe^{2+} while Fe^{3+} is insoluble. Therefore ferruginous cement will be most likely stable as formation water comes in, while for the formation water itself, since ferric irons commonly exist, the chemical reaction may occur as:



i.e, there may be some Fe^{3+} deposition in the rock pore system.

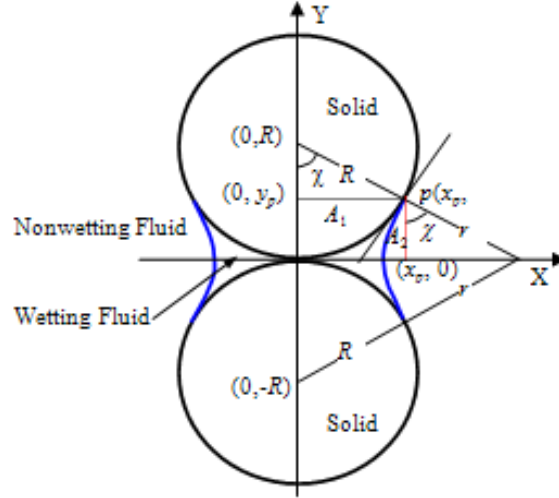


FIGURE 14: A microscopic model for capillary strength [Han et al., 2002]

Changes of Surface Tension and Capillary Force

Assuming rock particles have the same size and contact tangentially, with a zero contact angle between fluid and particles (**Figure 14**), Han et al. [2002] proposed a model to quantify rock strength changes with fluid saturation. Rock capillary tensile strength (σ_T) could be expressed as

$$\sigma_T = \lambda \frac{1-\phi}{\phi} \frac{F_c}{4R^2} \quad (2-39)$$

where R is the radius of the spherical rock particles, ϕ is porosity, and λ is a factor accounting for non-uniform particle size effects on total rock strength. A value of $\lambda = 6\sim 8$ is suggested for packs of particles with a narrow size range, and $\lambda = 1.9\sim 14.5$ for packs with wider particle size distributions [Schubert, 1984]. For UCS,

$$UCS = \lambda \frac{1-\phi}{\phi} \frac{\sin \phi}{1-\sin \phi} \frac{F_c}{2R^2} \quad (2-40)$$

which illustrates that, for loosely compacted rock, rock capillary strength is related to porosity, friction angle, capillary force, particle radius, and particle size distribution.

The Pressure Difference Method is applied to calculate the capillary cohesive force resulting from capillary pressure (P_c)

$$F_c = \pi x_p^2 P_c \quad (2-41)$$

, assuming that the shape of the liquid bridge between grains is a toroid characterized by radii r and x_p . Then, capillary pressure across the liquid bridge can be calculated by

$$P_c = \gamma \left(\frac{1}{x_p} - \frac{1}{r} \right) \quad (2-42)$$

Figure 15 plots various rock capillary strengths, such as UCS, tensile strength, and cohesive strength, and capillary force vs. fluid saturation. Compared to the rapid decrease of capillary pressure with water saturation, the decline rates of capillary force and strengths with saturation are much slower. When particle radius is 0.1 mm and fluid surface tension is 0.036 N/m, the maximum capillary strength can be as high as 20 kPa, whereas all capillary variables become zero around a saturation value of 0.34. However, there is a small section of the relationship at fluid saturation approaching zero where a short increase of strength is predicted, because some volume of water is needed to build a stable liquid bridge between particles.

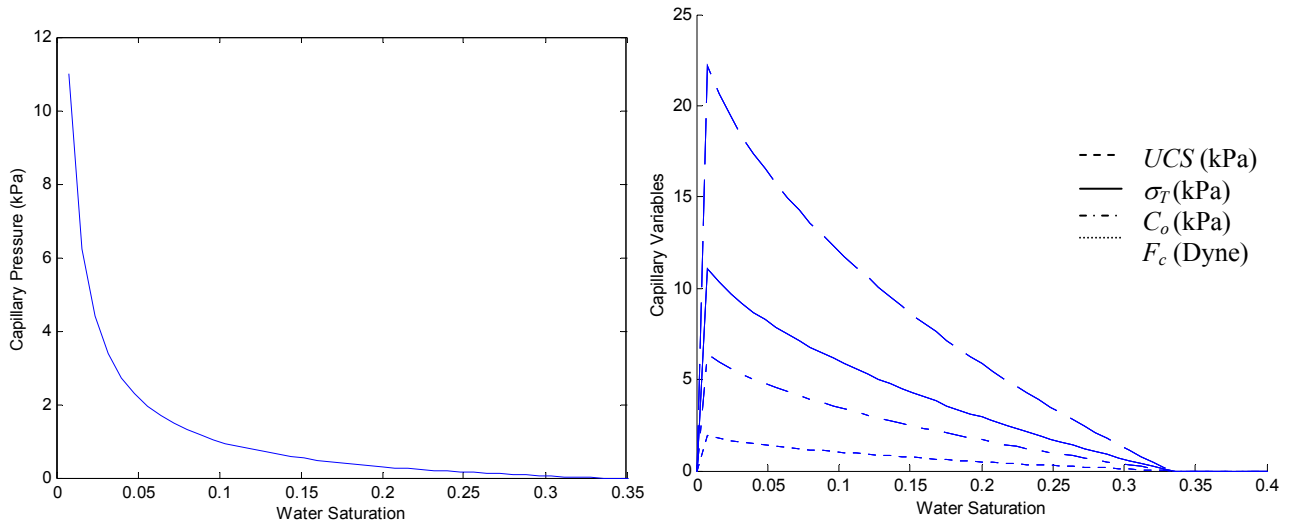


FIGURE 15: Variations of capillary pressure, force, and strengths with water saturation [Han and Dusseault, 2005]

Swelling and Disintegration of Shale

Clay behavior is very complicated and controversial. Generally, clay tends to precipitate authigenically in the voids among rock particles rather than at the contacts; therefore it carries little direct stress and does not directly contribute to the decrease of rock strength. However, when in contact with different water chemistry, the swelling behavior of smectitic clay (even in small fractions of the rock) may greatly affect rock stability. The swelling clay volume decreases the rock permeability, which increases the local pressure, which can cause increased fluid drag forces.

In many cases, several mechanisms may function simultaneously in a destabilizing direction. But is this effect important for extraterrestrial drilling? The short answer is yes. Imagine for example drilling deep holes on a planet or a moon with highly abundant water-ice formations (e.g. Mars or Jupiter's moon, Europa). It is highly probable, that heat generated by the drilling action could sufficiently warm up the water-ice bound formations to in fact melt the ice at the bottom of the borehole. Disregarding dangers of this situation (thawed water-ice could refreeze onto the drill and the surrounding borehole walls and trap the drill inside a hole forever) it is very likely that liquid water could in fact make the rock ahead of the drill bit weaker and in turn easier to drill. This effect may be present on extraterrestrial bodies that have no atmosphere (i.e. vacuum) as is the case on the Moon or have a very low atmosphere, with pressures below the triple point of water as is the case with the Martian South Polar Region. Having an atmospheric pressure below the triple point of water, at 6.1 mbar, ensures that no liquid water can be present

for an extended period of time. However, water-ice still may be present, but as soon as the ice temperature reaches zero, the ice will sublime directly to water vapor and will not go through the liquid state as is the case on Earth. But, in deep holes where drilled cuttings could accumulate around the drill, sealing the bottom of the hole from the outside atmosphere, a local atmospheric pressure in the lower part of the hole may in fact reach pressures above the triple point of water when enough ice sublimates to vapor (in this case, the partial pressure of sublimed water vapor will in fact be the same as the total atmospheric pressure).

2.2.3.7 Temperature

Another parameter that affects rock strength is temperature. On Earth, because of geothermal gradient, rocks lying deeper underground are hotter. Very high temperatures combined with high overburden pressure make rock more plastic and in turn more difficult to excavate. This was for example found by Soviet scientists and engineers working at the Kola Superdeep Borehole project. They found that at the depth of 12,262 meters the temperature was 180°C instead of expected 100 °C, and at these high temperatures drilling deeper was found to be unfeasible with then current state of drilling technology.

High temperature drilling will also have to be dealt with on two planets in our Solar System: Venus and Mercury. Venus surface temperature is in the range of 460°C, while that on Mercury in fact ranges from -180°C just before the sunrise to 427°C in the early afternoon [Watters, 1995]. This large thermal fluctuation is due to Mercury rotation and lack of atmosphere that has a tendency to trap the heat. High surface temperature on Venus, on the other hand, is due to its very dense carbon dioxide atmosphere that traps most of the heat. On both Mercury and Venus the temperature is so high that in fact zinc and tin would melt.

Unlike the challenges of high temperature (that make a rock more plastic) and very high overburden pressures (that make a rock stronger) that are pertinent to Earth, the challenges of drilling on most extraterrestrial bodies (except for Mercury and Venus) arrive from having to deal with rocks at extremely low temperatures. For example, the temperatures on Mars can be as low as -140 °C and on the lunar polar craters even as low as -230°C. The average temperature on the surface of a typical asteroid is approximately -70°C, while of the comet Tempel 1 the temperature varies from -113°C in shadow to -44°C at the point directly below the sun [Tempel 1 website, 2008].

Unlike high temperature that makes rocks more plastic, low temperature makes rock much harder and in turn much more difficult to drill. Much research has been conducted over the last century to determine the effect of low temperature and variable moisture content on the strength of different rocks. In particular, Mellor [1971] performed a very comprehensive study, during which he investigated the strength of sandstone (Berea Sandstone), limestone (Indiana limestone), and granite (Barre granite) from temperature ranging from +23°C to -195°C and at moisture contents ranging from zero (over dried rocks) to their full saturation.

The major effect of rock strengthening at low temperatures occurs when rocks have significant amount of water. It has been observed by Mellor [1971] that as the temperature of a rock is decreased, the rock strength gradually increases and it reaches the limit at around -120°C. At this temperature, the compressive and tensile strengths of Berea sandstone, Indiana limestone and Barre granite are higher than room temperature values by factors of around 5, 4 and 2, respectively (see **Figure 16**). However, Mellor also observed that with a further decrease in temperature to -196°C, the strength of the rocks in fact dropped.

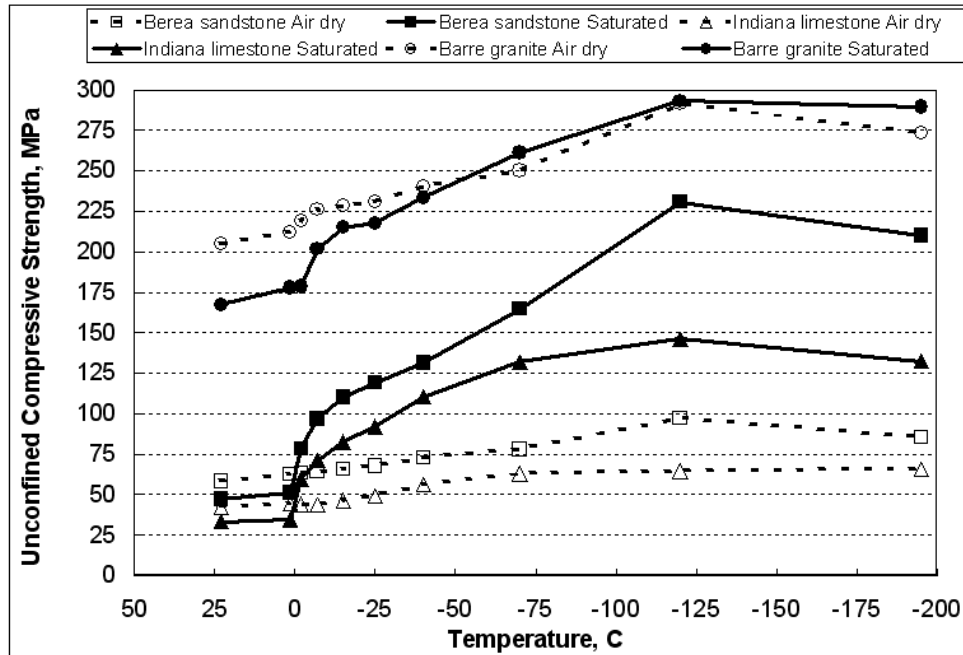


FIGURE 16: Effect of Temperature on Unconfined Compressive Strength for the “air-dry” and saturated sandstone, limestone and granite [after Mellor, 1971].

Mellor explained the rock strengthening effect as follow: as the temperature dropped, water begun to freeze in the largest pores, and progressively started to also freeze in smaller pores. This freezing effect of water in pore spaces had an effect of plugging cracks and pores in the rock and in turn increasing the rock strength, since now, much fewer cracks were present. However, as the temperature was reduced to below a certain value, the differential coefficient of thermal expansion caused the differential strain between the rock and the ice matrix, which resulted in weakening of the rock.

Heins and Friz [1967] also found that the strength of oven-dried basalt rock increased by 50% when cooled down to -196°C . This temperature dependency on the strength of basalt was confirmed by Zacny and Cooper [2007]. In particular, they found that the strength of basalt increased from 256 MPa at $+100^{\circ}\text{C}$ to 310 MPa at -100°C , or by 20%. The reason why the strength of basalt was not as pronounced as the strength of sandstone or limestone, was because basalt having much lower porosity and permeability, has intrinsically lower saturation levels.

2.3 Stresses and Energy in Drilling

2.3.1 Stress in Sedimentary Basins

2.3.1.1 Definitions, Total and Effective Stresses

Stress cannot be measured directly, only inferred from other measurements (pressure, displacements, tectonic data, geological history...). Stresses are carried by the solid material and the liquid; herein, “pressure” refers only to the compressive potential in a fluid.

Stress state in rock mechanics is defined in terms of principal compressive stresses and their orientations (**Figure 17**) acting at a single point:

- Three principal stress magnitudes acting normal to the principal planes, σ_1 , σ_2 and σ_3 indicate major, intermediate and minor principal compressive stresses (compression positive);
- Three mutually perpendicular principal stress orientations, each corresponding to a principal stress direction, usually stipulated by direction cosines in a Cartesian reference frame; and,
- A single value for the pore pressure - p_o .

The first six define a symmetric second-order tensor; the pore pressure is a scalar, independent of direction. With these seven independent values, stresses along and across any plane passing through the point can be computed. Further definitions and equations for stress transformations and calculations may be found in continuum mechanics texts [e.g. Beer et al., 2005].

Only exceptionally is it possible to fully define the stress state *in situ*; generally, assumptions must be made. In sedimentary basins, it is assumed that the vertical stress, σ_v , is a principal stress (either σ_1 , σ_2 or σ_3); so that the other two orthogonal principal stresses are parallel to the earth's surface. The two horizontal principal stresses are the maximum and minimum principal horizontal stresses, σ_{HMAX} and σ_{hmin} . In Petroleum Geomechanics, it is the convention to report principal stresses as total stresses, along with the pore pressure as an independent value.

In Cartesian coordinates, the Terzaghi principle of effective stress is defined as follows:

$$\begin{bmatrix} \sigma'_x & \tau_{xy} & \tau_{xz} \\ \tau_{yx} & \sigma'_y & \tau_{yz} \\ \tau_{zx} & \tau_{zy} & \sigma'_z \end{bmatrix} = \begin{bmatrix} \sigma_x & \tau_{xy} & \tau_{xz} \\ \tau_{yx} & \sigma_y & \tau_{yz} \\ \tau_{zx} & \tau_{zy} & \sigma_z \end{bmatrix} - \begin{bmatrix} p & 0 & 0 \\ 0 & p & 0 \\ 0 & 0 & p \end{bmatrix} \quad (2-43)$$

where σ is total normal stress, σ' is effective normal stresses, τ is shear stress, p is pore pressure, and x, y, z are the three coordinates. The above equation expresses the principle that effective stresses are the difference between total stresses in the rock skeleton and pore pressure in the interconnected voids. Principal effective and total stresses are always co-axial because p is a scalar. Further, because pore pressure always acts normal to the surface of rock particles as a hydrostatic force, it contributes nothing to the shear stress that acts parallel to a plane.

The concept of effective stress lays the foundation for rock stability investigation in fluid-saturated underground conditions because it is effective stresses that act on the rock particles to stabilize or mobilize them.

In Petroleum Geomechanics, a form of $\sigma' = \sigma - \alpha P$ has generally been used, where α is called Biot's poroelastic constant. Physically it means that the rock skeleton carries the part σ' of the total external stress σ , while the remaining part, αP , is carried by the fluid in the porous medium. Expressed as $\alpha = 1 - \frac{C_m}{C_b}$, (C_m and C_b are the compressibilities of rock matrix and rock

bulk, respectively), α is difficult to measure, given the inherently complex nature of a porous medium. However, α is restricted to the region $0 < \alpha \leq 1$, and for unconsolidated or weak rocks, α is close to 1 [Fjær et al., 1992].

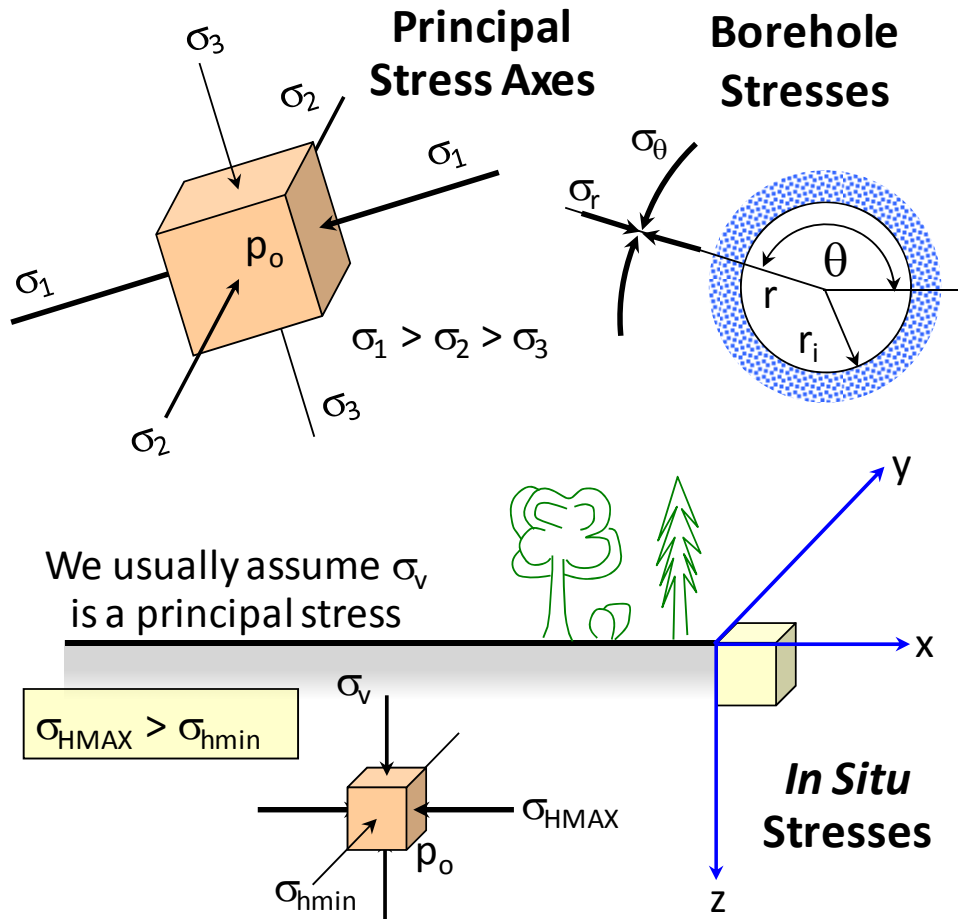


FIGURE 17: Some stress definitions commonly used in Petroleum Geomechanics

2.3.1.2 Stress Boundary Conditions

All geomechanics problems, including drilling analysis, take the *in situ* stress state as the point of departure; the same is true for drilling; the *in situ* (far-field) stresses and pore pressures constitute the boundary conditions for analysis. *In situ* stresses are predicated by tectonic, diagenetic and burial depth issues; these act at scales of 1-100 km. Stresses, $[\sigma]$, pressure and temperature, p_o and T_o , and even the pore water chemistry, $\{C_i\}$, are altered by the drilling process in a zone perhaps 5 to 10 times the borehole diameter (**Figure 18**). A drill bit is 100-500 mm diameter, so this zone is on the order of several meters; however, where the cutting tool tip acts on the rock, the relevant scale is perhaps 1-10 cm. Clearly, understanding stresses and stress changes at all scales is vital for drilling and borehole stability analyses.

In altered conditions, such as drilling through depleted reservoirs and zones where cold or hot fluids have been injected, or in side-tracking a new borehole from an existing cased hole, some form of mathematical modeling is needed to calculate the stresses in these changed conditions. Again, initial stress and pressure fields serve as the point of departure.

Effective stresses near the drill bit are changed by fluid pressure and stress relief. Drilling fluid density, borehole wall filter cake properties, and the transport characteristics of the rock

mass also affect stresses over time because of diffusion processes. In shales, pore fluid and mud filtrate chemistry, combined with Darcian and Fickian diffusion processes (Δp -flow, osmotic suction, concentration-gradient driven flux), can lead to volume changes (ΔV), which in turn alter the stresses (**Figure 19**) and perhaps affect the permeability. The drilling fluid is cooler than the rock at the bit (ΔT), leading to transient thermoelastic stress changes, as well as changing the rate of diffusion because fluid viscosities change with temperature and diffusion processes are kinetically activated. Finally, the bit and drill string apply a normal and shear load to the rock face through the tool contact. These processes affect physical parameters such as permeability; thus, rigorous analysis of rock stresses in drilling is a fully coupled thermal-hydraulic-mechanical-chemical problem. In the elastic behavior range, at least a Biot formulation is required [e.g. Wang and Dusseault, 2003], and generally effects of elastic non-linearity, plasticity and rupture will arise. Clearly, constitutive behavior is also a vital aspect of analysis in geomechanics.

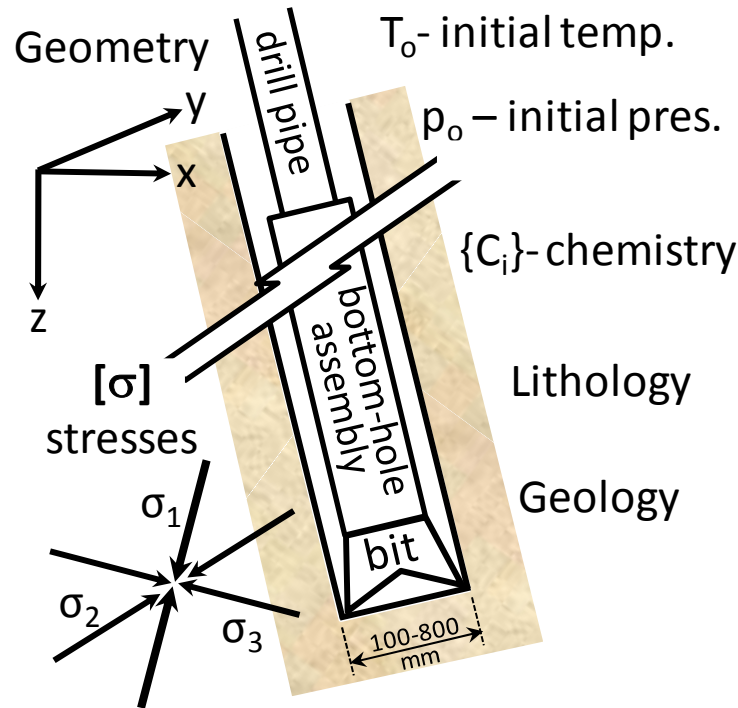


FIGURE 18: Initial conditions in drilling. All these factors change with depth, and many mechanical properties (strength, stiffness) are anisotropic. Furthermore, there are discontinuities such as joints, bedding planes, and faults.

In virgin conditions, far-field stresses apply, but in depleted reservoirs and ΔT processes, stresses have been altered, perhaps massively: the stress fields have changed, and principal stress directions have rotated. Altered stress conditions are case-specific, and must be measured or computed from initial conditions, constitutive laws, and boundary conditions. The subject of this section is the estimation of far-field stresses, which are the point of departure for drilling planning and analysis. Far-field stresses also impact issues such as hydraulic fracture behavior, casing shear, fractured carbonate production behavior, and so on.

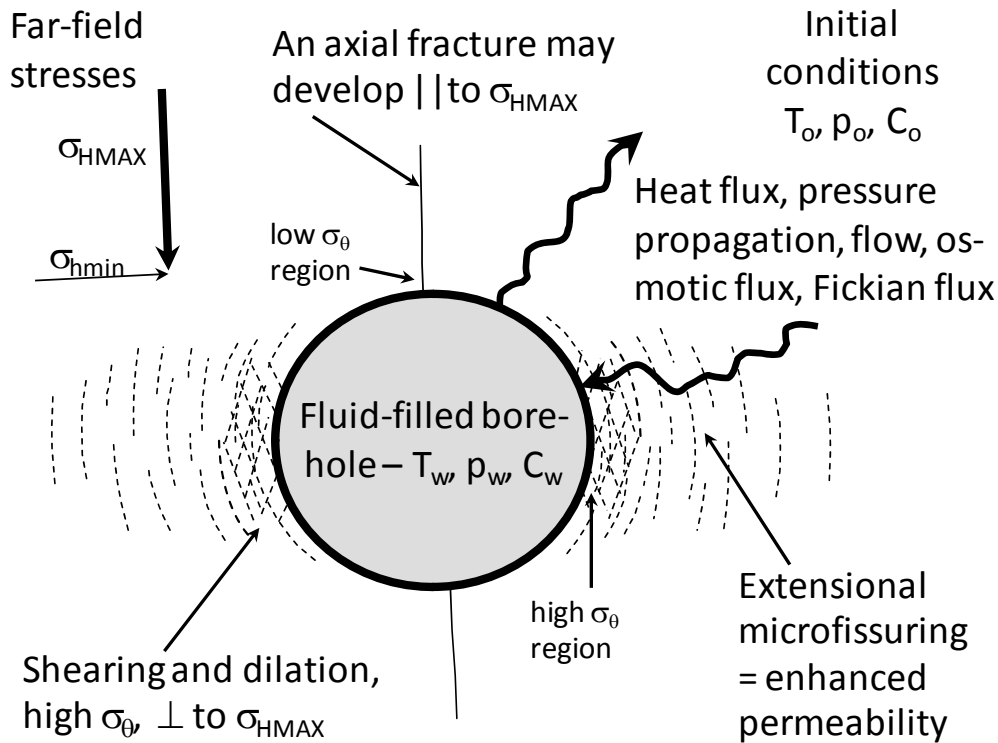


FIGURE 19: Diffusion processes near a borehole are coupled with the thermal effects, the chemical effects, and the mechanical effects.

2.3.1.3 Stress Orientations

The orientations of the two horizontal principal stresses may be determined by various means. Common methods are briefly introduced and discussed here.

Borehole breakouts are spalls which develop on opposing sides of the borehole during drilling. In near-vertical holes ($\pm 10^\circ$), breakouts are oriented perpendicular to σ_{HMAX} (**Figure 20**). Breakouts are analyzed with a set of quality control criteria; poor data are rejected and good data ranked according to quality [Zoback 2007]. Some of the factors to be considered are:

- Is the well within 10° of vertical? ($< 5^\circ$ is better)
- Is the breakout occurring over a long interval?
- Are there other consistent breakouts above and below?
- Is the breakout actually hole enlargement, a wash-out, a key-seat?
- Are strata anisotropic and inclined, leading to spurious orientations?
- Is the breakout in a lithologically consistent zone?
- Do the data make sense overall, regionally and with offset wells?

Boreholes commonly display extensional fractures in the wall, arising because of wellbore damage combined with pressures from the mud, particularly repeated surge pressures during trips and connections. If the well is near-vertical, these show up clearly on geophysical logs as fine vertical cracks, sometimes continuous over substantial lengths (**Figure 21**). They are easily differentiated from natural fractures that have sinusoidal wall traces, and from the dark black breakouts which are, as expected, at 90° to the extensional fractures. Because extensional

fractures will open normal to σ_{hmin} , they can be used, along with the log azimuth data, to give the direction of the two horizontal stresses. If the well is inclined somewhat, these extensional fractures will appear “en echelon” in the wall, but the direction may still be reasonably estimated. Care has to be taken that the inclined well has not caused a large rotation of the principal stresses in the well vicinity, giving spurious induced fracture orientations, so quality control criteria similar to those used in breakout analysis are used.

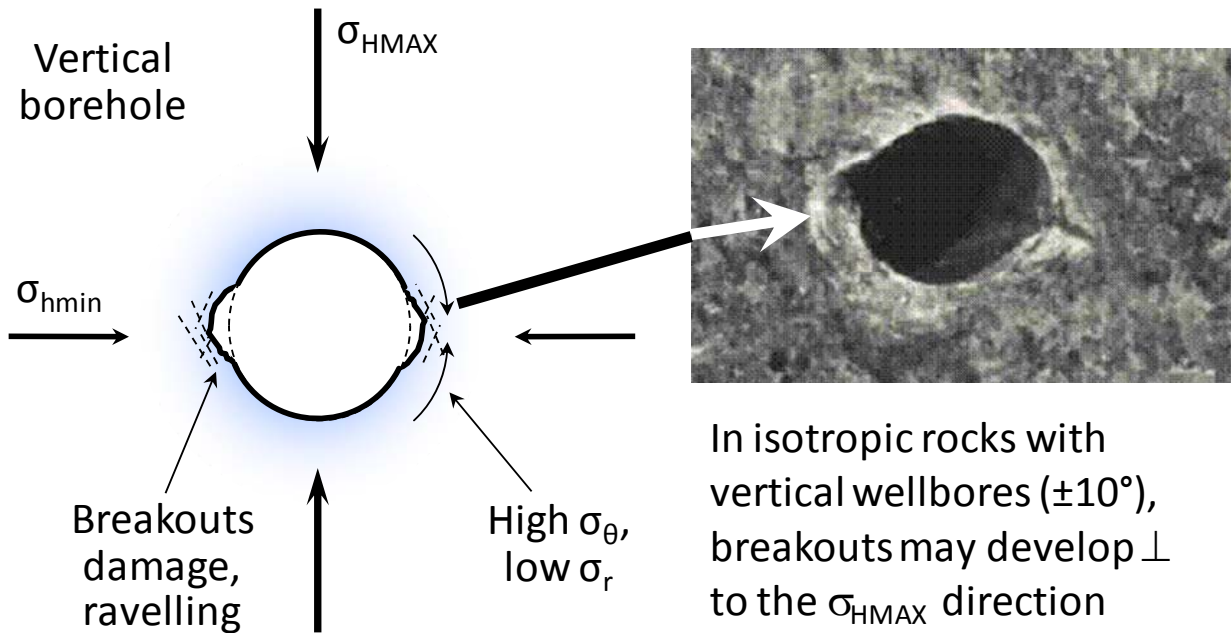


FIGURE 20: Borehole breakouts arise from yield of rock in the direction normal to σ_{HMAX} . Photo courtesy of Bezalel Haimson.

In an anisotropic stress field, the borehole will usually experience anisotropic wall damage, even if no breakouts or axial extension fractures are present. Microfissuring normal to σ_{HMAX} dominates, as with breakouts. It is likely that the filtrate has penetrated more deeply in the damaged region, giving an anisotropic resistivity response (**Figure 22**). This may be detectable on four-arm or multi-sensor resistivity meters, particularly for focused logs that measure resistivity at different wall depths, particularly in the range of 10-50% of the borehole radius. As always, quality control is necessary.

Core measurements have been widely used (and often abused) to assess stress orientations. All methods take advantage of anisotropic behavior of some kind, and several common approaches are discussed briefly here.

When a homogeneous rock is cored and brought to surface, it displays a small, slow expansion for some time (days). If a fresh piece of core is mounted in a precision measuring device, isolated from further temperature or moisture changes, and the time-dependent diameter changes measured in several directions; the maximum strain recovery can then be related to the direction of σ_{HMAX} . Assuming the orientation of the core is known, *in situ* stress directions may be inferred. This method is known as differential anelastic strain recovery [Ren and Roegiers 1983]. Rock anisotropy can confound this process, and it is best to test several specimens simultaneously to assure a consistent response.

Any piece of competent oriented core can be tested for radial variations in various properties. Core can be oriented by scribing during entry to the barrel, or by alignment with borehole wall log or image data. If the rock has a distinctly oriented microfissure fabric, it may reflect the stress field anisotropy, assuming that the anisotropy is directly related to the present stress field, not a paleo-stress field or inherent rock anisotropy. Among properties that may be used are differences in strain response, thermal expansion behavior, acoustic emissions, and so on [Villaescusa et al., 2002].

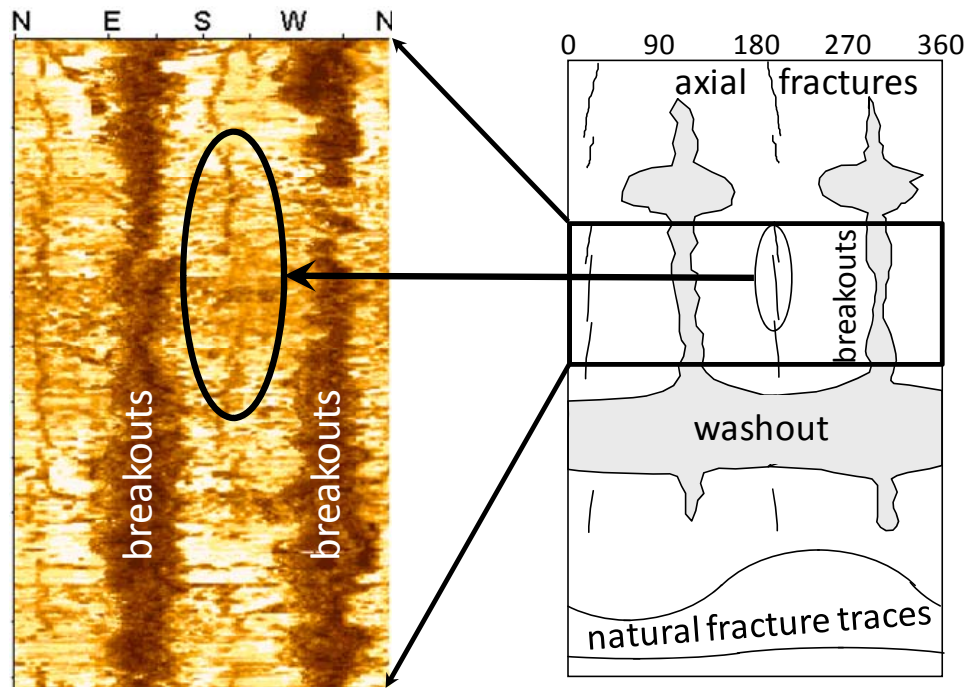


FIGURE 21: Use of borehole wall imaging methods to determine stress orientations. Here, a formation micro-resistivity imaging log is used to identify breakouts and fractures.

If old, unoriented core is all that is available, it is usually possible to obtain good core orientation ($\pm 5^\circ$ in azimuth) using paleomagnetic signatures, combined with the geological age of the specimen. Magnetic particles sedimented along with the rock matrix aligned themselves in the Earth's magnetic field at that time, and this "signature" is preserved permanently. Once the natural magnetization vector is quantified, it can be corrected for magnetic North Pole direction at the time the sediment was laid down. Polar orientations over geological time are widely known from continental drift studies of polar wandering. After the core is oriented, other properties may be used to infer stress orientations.

Geological inference is a powerful means of assessing stress directions [Pollard and Fletcher, 2005]. Generally, near faults, mountain chains, grabens (rifts), and so on, stresses reflect the geometry of the geological structures (**Figure 23**). For example, σ_3 ($= \sigma_{hmin}$) points in the direction of the strike of an active, planar, high-angle fault (a normal fault), but at 90° to the strike of a compressive thrust fault. In the latter case, it is also the vertical stress - σ_v . If the fault is a strike-slip fault, the direction of motion must be determined, and then σ_3 ($= \sigma_{hmin}$) directions can be estimated; usually, σ_{hmin} lies in an orientation about 60 - 70° from the strike of a fault. Care is necessary to assure that the features are related to the present-day stresses, and that there

hasn't been a stress field rotation since the time the fault was active. This method works well, in a regional sense, near active rifting (e.g.: East Africa rift belt) and active compressive mountain building (e.g.: Rocky Mountains and Andean forelands). Of course, local distortions can be superimposed on this stress field, particularly with greater distance from the active mountain front.

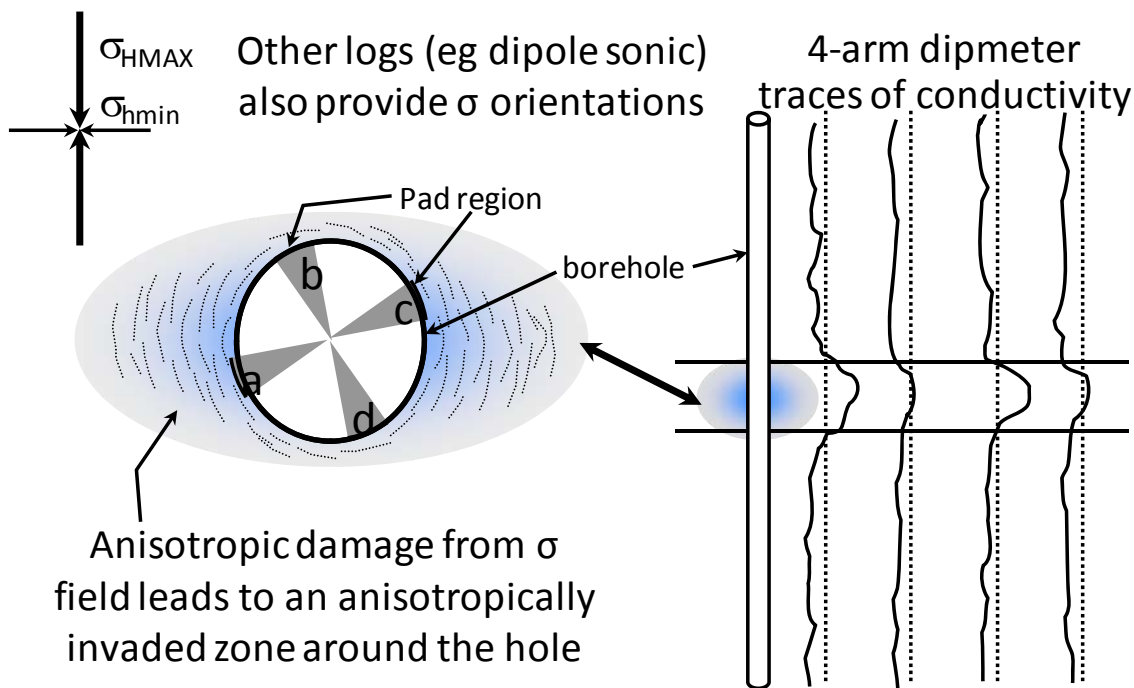


FIGURE 22: Here, induced resistivity anisotropy arising from anisotropic fluid invasion gives information about stress orientations.

In some basins, the large-scale geometry controls the stress distributions, particularly along continental margin basins (**Figure 24**). Along the Gulf Coast of the United States, σ_{hmin} is consistently aligned perpendicular to the continental shelf trace, with local variations superimposed from salt tectonics and local effects. Inland basins far from mountain-building or rift tectonics may also have a regional signature imposed by the geometry of the basin.

Other geological factors can affect the stress fields at scales of 1-30 km, including vulcanism, salt diapirism, regional arching or subsidence, or lithological differences. For example, in the salt-diapir related Chalk oil-fields in the North Sea, a radial distribution has been superimposed. In areas of intense gas migration and active pore pressure generation, effective stresses are severely affected. In strongly uplifted regions, on the other hand, pore pressures can be much lower than hydrostatic. In such cases, measurements combined with geological inference should be used.

The orientation of large hydraulically induced fractures will be at 90° to the orientation of σ_3 . Providing that $\sigma_{hmin} = \sigma_3$, the fracture will propagate vertically in the natural stress field. The fracture must be large enough to be beyond the effects of the borehole region, and much larger than any joint spacing in the rock (joints affect local but not large-scale propagation direction). Hydraulic fracture orientation can be determined in various ways, but perhaps the most reliable method for large vertical fractures at moderate depths (<3 km) is high-precision tiltmeters

arrayed on the surface [Wills et al., 1992]. Other methods use direct borehole measurements, interference tests among wells (one of which was fractured), microseismic mapping, and so on.

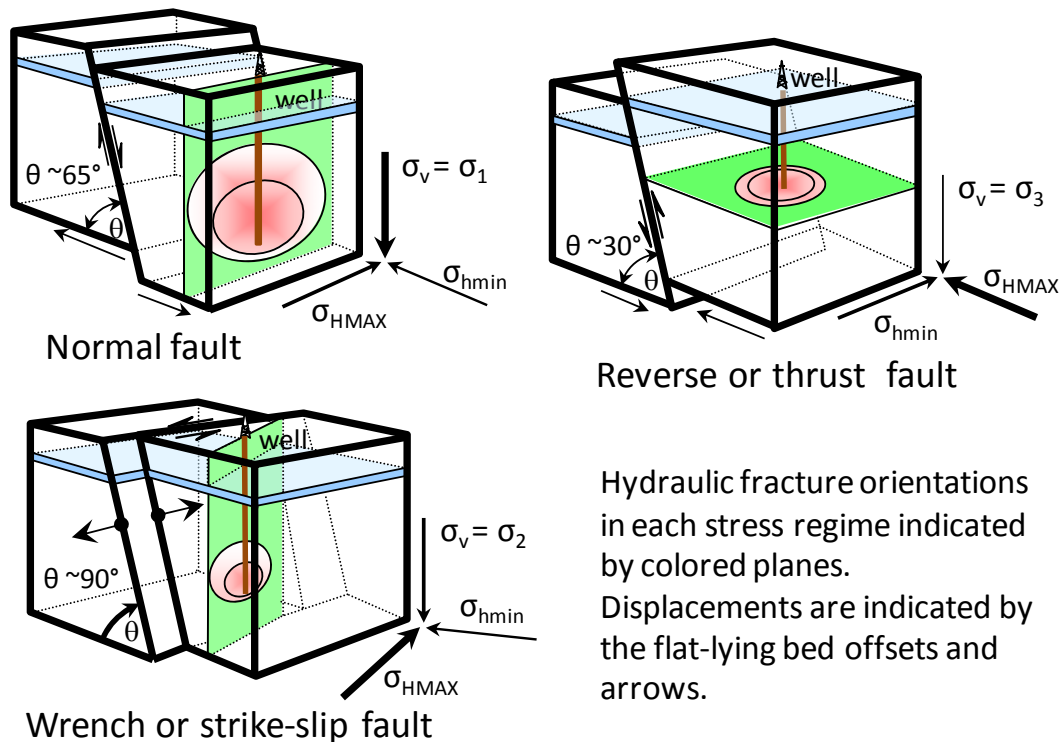


FIGURE 23: Stress regimes, characteristic fault orientations, typical hydraulic fracture orientations

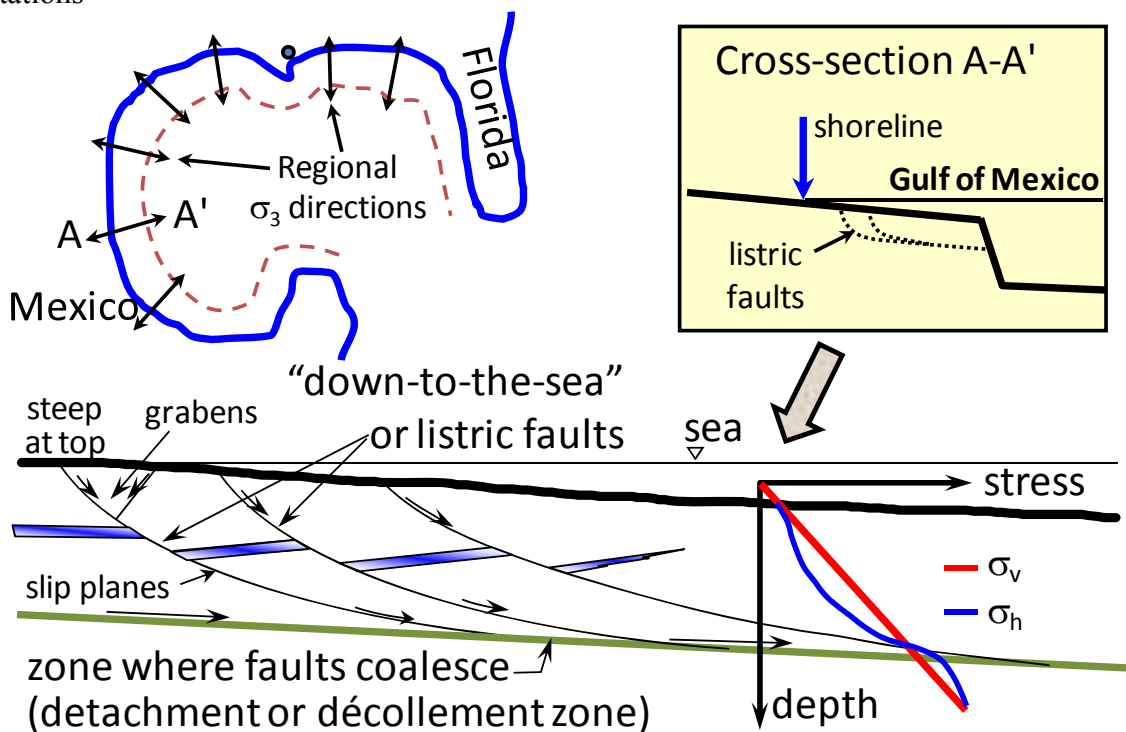


FIGURE 24: Gulf of Mexico or listric fault regime (also, “down-to-the-sea” or “growth” faults)

Finally, seismic shear wave velocity anisotropy can reflect stress anisotropy. However, wave transmission is highly sensitive to fabric, and if the rocks now have a different stress orientation than when the fabric developed through diagenesis and tectonics, seismic anisotropy may not reflect present-day stress orientations. Sonic dipole geophysical logs can determine seismic attributes anisotropy in the plane of the borehole, and these data may be used to estimate orientations and relative effective stress magnitudes. These data are then “calibrated” using leak-off tests (LOT, XLOT) or hydraulic fracture data (MiniFrac™ or similar tests), and the service company then provides a continuous estimate of the stresses with depth. Of course, as with all correlations, caution should be exercised in using the data.

2.3.1.4 Stress Magnitude Estimation

The vertical total stress, σ_v , is the weight of the overlying rocks (and water) acting on a unit area. This can be calculated using a density log assisted by precise core density measurements. It can usually be calculated to within ± 2 MPa at a depth of several kilometers, or within 2-3% with excellent reliability (95% probability).

The relative magnitude of the principal stresses can often be gauged by geological inference, using the tectonic history of the basin, appropriate faults, domal structures, etc. For example, mobilized salt at depth sometimes forms distinct elongated ridges (almost “waves”); these are at 90° to the direction of σ_{hmin} ($= \sigma_3$), and thus a relative magnitude is obtained, compared to the other two stresses. Other features (faults, folds, fracture patterns...) can be used to estimate relative stress magnitudes, but quantification of stress values requires further information.

In discussing stresses, K' , the ratio of the horizontal to vertical effective stresses is often used: $K' = \sigma'_{hmin}/\sigma'_v$. If $K' > 1.0$, lateral stresses are greater than σ_v and induced hydraulic fractures will be horizontal; these are thrust fault conditions (**Figure 23**), sometimes called compressional conditions. If $K' < 1.0$, normal or strike-slip fault conditions exist, called extensional and transpressional respectively, and hydraulically induced fractures will be vertical. Also, on an active fault plane with friction angle of ϕ' and no residual cohesion, the following effective stress ratio exists: $\sigma'_1/\sigma'_3 = (1 + \sin\phi')/(1 - \sin\phi')$. This relationship allows stress estimates to be made in some circumstances.

If a fault has been active in the recent geological past (tens of thousands of years), frictional behavior along the fault plane can be assumed; this gives some bounds to the horizontal stresses near the fault. Consider a 4 km deep active normal fault with $\sigma_v = 95$ MPa and $p_o = 50$ MPa. We can estimate the following:

$$\sigma_v = \sigma_1 \text{ and } \sigma'_v = \sigma_v - p_o = 45 \text{ MPa}$$

Assume a friction angle of $\phi' = 30^\circ$; then, $K' \approx 0.33$ if rock is in the critical slippage condition. $\sigma'_{hmin} = \sigma'_3 = K'\sigma'_v = 15$ MPa, and therefore $\sigma_{hmin} = \sigma'_{hmin} + p_o = 15 + 50 = 65$ MPa. This is considered to be a lower-bound estimate for σ_{hmin} ; the actual value of σ_{hmin} in the fault region is likely in the range 65-75 MPa. Since $\sigma_{HMAX} = \sigma_2$ and $\sigma_3 < \sigma_2 < \sigma_1$, $65 \text{ MPa} < \sigma_{HMAX} < 95 \text{ MPa}$. Often, we estimate $\sigma_2 = (\sigma_1 + \sigma_3)/2$ so that $\sigma_{HMAX} \approx 80$ MPa

It is instructive to repeat these calculations for a typical Gulf of Mexico listric fault at 5 km depth. The deep detachment plane is horizontal, in a zone of overpressure, and along a shale

band. Although σ_v may no longer be exactly a principal stress, we will assume it is: $\sigma_v = \sigma_3 = 105$ MPa, $p_o = 85$ MPa, and the shale friction angle $\phi' = 10^\circ$, so that $K' \approx 1.4$ at the condition of fault slip. Carrying out calculations gives $\sigma_{HMAX} = 113$ MPa and σ_{hmin} in the range of 105-113 MPa. One notable factor is that in an overpressured regime with slip along low-friction shale beds, all of the principal stresses are of similar value.

Leak-off tests (LOT), carried out when a casing shoe is drilled, are used to estimate σ_3 magnitude (usually $\sigma_3 = \sigma_{hmin}$ in these cases). During a LOT, if pumping is stopped after a slope change (**Figure 25**) and before a clear pressure drop takes place, a poor estimate of σ_{hmin} may be obtained. Best practice is to continue pumping until a after a pressure drop is observed and a stabilized injection pressure is being approached. This is referred to as an extended leak-off test (XLOT), and σ_3 estimates using XLOT are more reliable.

Hydraulic fracturing is used to estimate stress magnitudes (**Figure 26**). Note that XLOT are merely hydraulic fractures executed with the drilling fluid as the injectate, but there remain issues of possible pressure losses in the annulus, which can introduce errors. Fracturing stress measurements are offered commercially by several service companies (e.g. MiniFrac™); they use precision pumps, downhole gauges, and a refined methodology. Such data are highly reliable σ_3 estimates, considered to give information within a few percent of true values with 95% certainty. Much has been claimed about the possibility of using hydraulic fracture data to get information on the other horizontal stress (σ_{HMAX}), through use of the fracture breakdown pressure (peak pressure before the pressure drop). The most that can be said is that the value obtained is almost certainly a lower-bound estimate for several reasons (thermal effects, borehole wall damage, existence of natural fractures); actual σ_{HMAX} values are likely to be different than values based on hydraulic fracture data.

Lateral stresses do not necessarily increase monotonically with depth, as σ_v does. Strata of different stiffnesses will display deviations from a regular increase in lateral stress magnitude; the amount and nature of the difference depends on the lithology, the mechanical properties (stiffness, creep capacity), and the deformation and stress history. In general, because of slow shear stress relaxation, σ_h values in ductile shales are closer to σ_v than are the σ_h values in adjacent dolomites and sandstones. Salt is a material which creeps under differential stress, so one may assume that virgin salt has an isotropic stress state *in situ* ($\sigma_v = \sigma_h$).

Figure 27 shows a hypothetical stress distribution that might arise if a sequence of beds of different stiffness is subjected to a small lateral compression in a foreland basin adjacent to compressive tectonics (e.g. west side of the Appalachians in USA, east side of the Andes mountains). The stiffer beds have taken the greatest load, ductile shales less so, and the salt remains at an isotropic stress state. In an extensional stress regime or a depleted reservoir, one might expect the mirror image, with the stiffest beds having the lowest σ_h value, and so on. An understanding of the tectonic evolution of a sedimentary basin gives clear clues as to the distribution of stresses among various rock units.

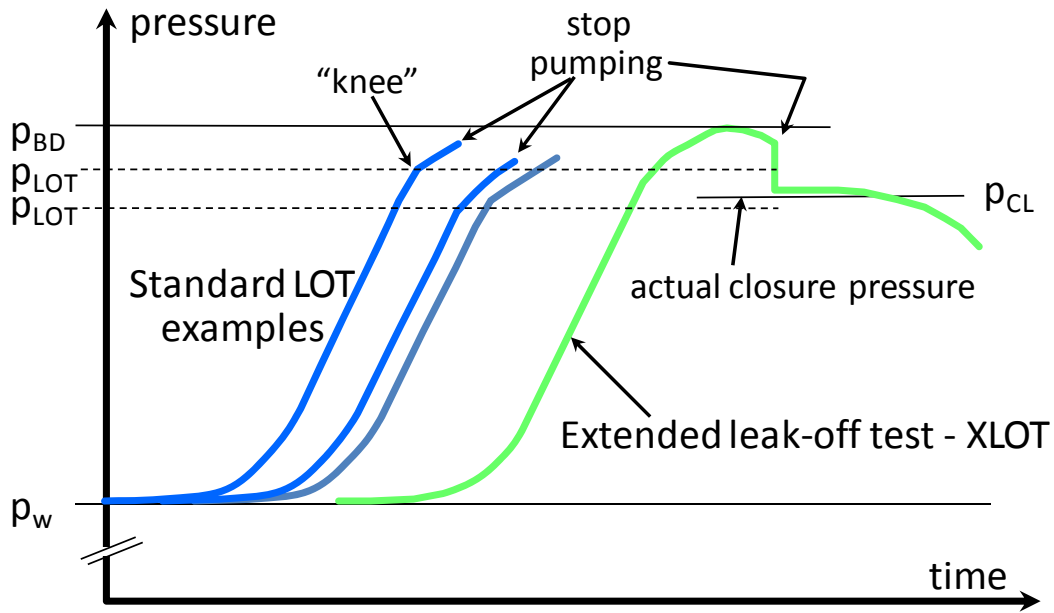


FIGURE 25: Leak-Off Tests (LOT) are best extended beyond the peak pressure – XLOT – for reliable σ_3 measurements. See **Figure 24** for definitions of some of the terms.

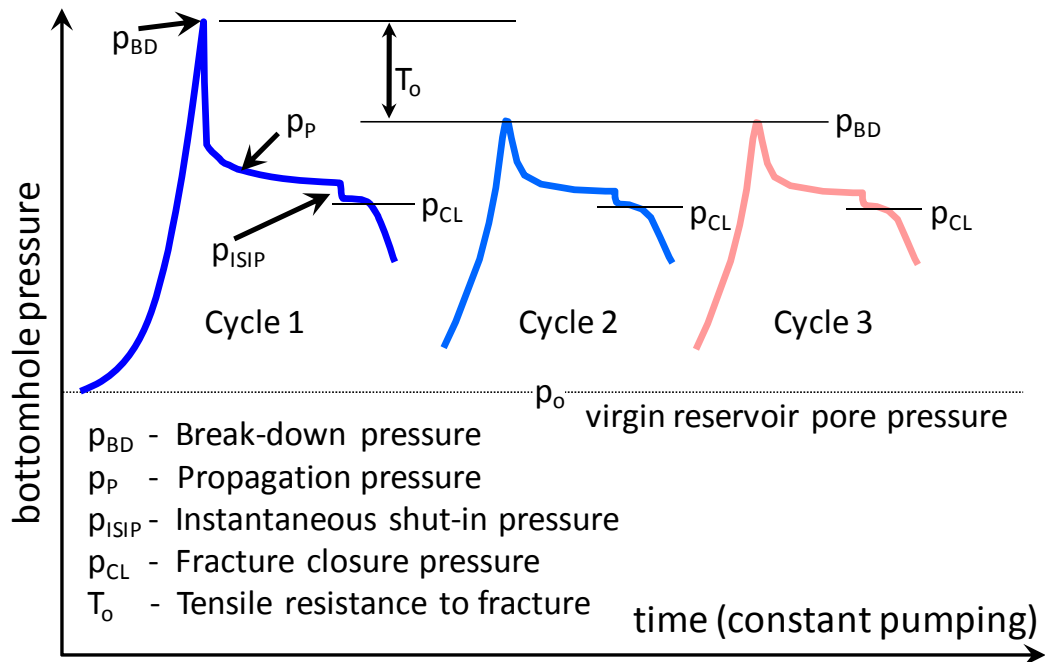


FIGURE 26: A detailed hydraulic fracture stress measurement procedure with multiple cycles

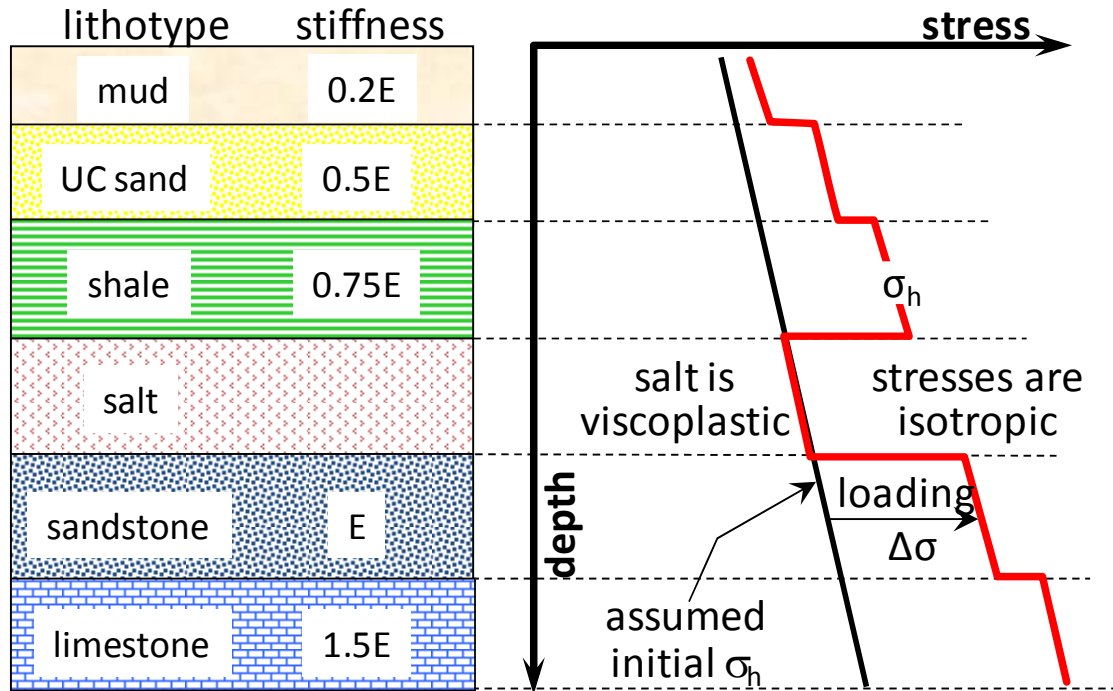


FIGURE 27: Relative stress values arising from compressional strain in a compressive foreland

2.3.1.5 Pore Pressures - $p_o(z)$

To complete the stress state, pore pressure values are required, and these data are also vital to design casing programs and manage blow-out risk in drilling. Robust $p_o(z)$ estimates based on geological inference, off-set well data, seismic interpretation, and regional trends, are usually available. Properly calibrated correlations to geophysical log data and seismic attributes exist for some regions, but for other regions the relationships are weak or insufficiently calibrated. Ultimately, true $p_o(z)$ values must be measured directly using formation testing methods or installed sensors. Fortunately, $p_o(z)$ data are vital to oil exploration and reservoir engineering, so there is an incentive to collect good data; nevertheless, p_o values in shallow strata, shales and other non-reservoir rocks are rare. During hydraulic fracturing for stress measurements, a good measurement of p_o is almost always collected to round out knowledge of the stress state.

In drilling activity, great attention is paid to influxes of hydrocarbons, water, or even the sudden onset of shale sloughing; all of these are indicators that the mud weight is less than p_o , and such data can be valuable estimates of pore pressures.

After application of various approaches, it is usually possible to have good data on orientations, and reasonable data on p_o , σ_v , and σ_{hmin} . Thus, the stress state can be reasonably estimated and used in geological, geomechanical, and reservoir management applications, as well as in drilling prognoses and analyses.

2.3.1.6 Typical Stress Distributions with Depth

Based on experience, combined with some measurements and geological inference, it is possible to make valuable generalizations about stress distributions with depth in a number of tectonic environments. These are first-order estimates based on simple models; exceptions will always be found, and site-specific data must be developed by more detailed study.

Non-Tectonic Classical Basin and Diagenetic Effects

In a monotonically sedimented basin without erosion or significant lateral strain events (compressional, extensional, transpressional), lateral stresses are less than vertical stresses. **Figure 28** shows a stress distribution that might be expected in such a basin. Some general comments can be made for such cases.

The minimum K' value to be expected is perhaps 0.4-0.5 in sands and carbonates, 0.6-0.7 in shales. For example, at $z = 3$ km with $\sigma_v = 70$ MPa, $p_o = 30$ MPa, in a sandstone bed we would expect $\sigma_{hmin} \approx \sigma_{HMAX} = 45$ -55 MPa, and in an adjacent shale, 55-60 MPa. Shale ductility and large strains during compaction mean that σ_{hmin} in shales is closer to σ_v than in sandstones. However, diagenesis has a large role, especially in soluble rocks. The effect of standard burial diagenesis (compaction, pressure solution, cementation) is complex and only a few examples are presented here.

Smectite-to-illite mineralogy changes take place in shales as burial depth and temperature increase. In the Gulf of Mexico, smectite is a dominant clay mineral in shales to $z \approx 3$ -4 km, but is totally absent by $z \approx 6$ -7 km. Consider the stress effect in a flat-lying bed of smectitic shale. A large volume change accompanies the smectite→illite transition, giving a shrinkage potential of at least several percent in most smectitic shales. In the vertical direction, shrinkage is merely compaction; in the horizontal direction, because no-lateral-strain conditions apply, it results in σ_h loss until $p_o > \sigma_h$. Furthermore, because the smectite→illite transition expels water, p_o may rise in restricted drainage conditions. Extensive fracturing takes place, and a naturally fractured quartz-illite shale is generated with a greatly reduced lateral stress. These materials are prone to lost circulation and massive sloughing.

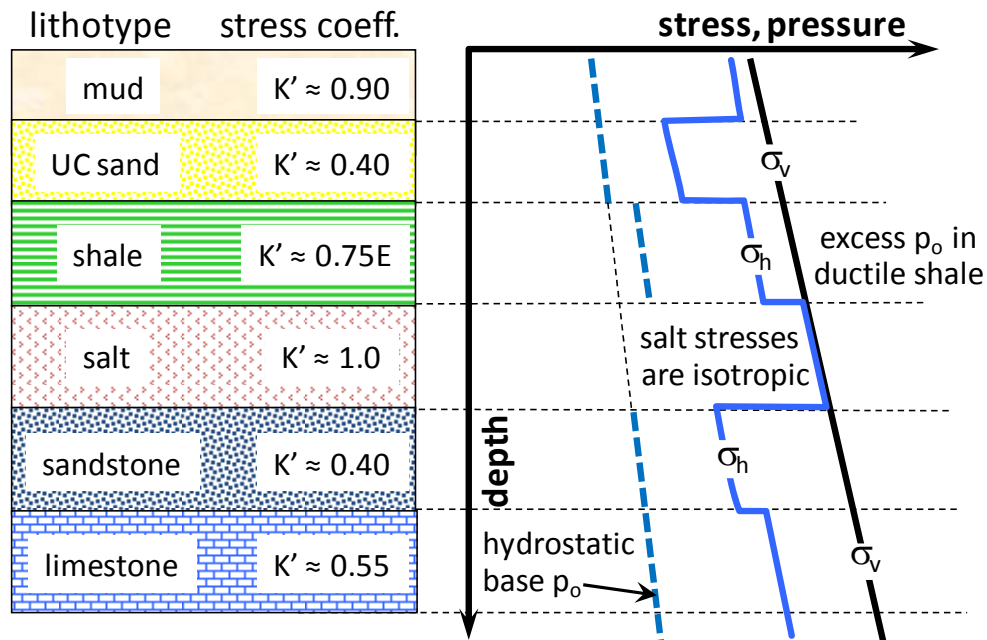


FIGURE 28: Stress coefficient values and stress distribution in a monotonically buried basin

Gypsum ($\text{CaSO}_4 \cdot 2\text{H}_2\text{O}$) changes to anhydrite (CaSO_4) with burial and temperature, but the high solubility of these minerals means that pressure-dissolution and recrystallization processes

continue slowly, reducing the difference between σ_v and σ_h , and also eliminating porosity in the process, generating a dense impermeable and non-fractured rock in which all stresses are close to the same value. Of course, salt creeps several orders of magnitude more rapidly than anhydrite, so in salt, all stresses are equal.

Dolomitization involves shrinkage, generating vertical fractures and reduced horizontal stress.

Pressure solution and recrystallization of SiO_2 in quartz sands leads to significant porosity loss. The process is sensitive to the stresses at the grain contacts: higher local stresses lead to higher dissolution rates, which in turn tend to give larger contact areas, lower local stresses, and attenuation of the process. The negative and positive feed-back processes involved in sandstone diagenesis are wonderful examples of the coupling of stresses, chemistry, fluid flux and temperature in the real world, altering stresses, permeability and rock fabric over time.

Eroded Basin

As rocks are buried, diagenesis makes them stronger and stiffer through compaction and porosity loss. Thus, in an erosive process, they are likely to respond elastically during unloading. Consider a flat-lying stratum subjected to general uniform unloading through erosion. $\Delta\sigma'_v$ leads to vertical elastic strain, ε_z , but the no-lateral-strain condition ($\varepsilon_x = \varepsilon_y = 0$) leads to the following relationship, often referred to as the “Poisson effect”:

$$\Delta\sigma'_h = \frac{\nu}{1-\nu} \cdot \Delta\sigma'_v$$

For sands, Poisson’s ratio is about 0.25, therefore $\Delta\sigma'_h \approx 0.33 \cdot \Delta\sigma'_v$. Consider a sandstone buried to 3 km depth ($\sigma_v = 70$ MPa, $\sigma_h = 55$ MPa, $p_o = 35$ MPa), and then erosion takes place until $z = 800$ m and $\sigma_v = 20$ MPa, $p_o = 8$ MPa. $\Delta\sigma'_v = -23$ MPa, thus $\Delta\sigma'_h \approx 0.33 \cdot \Delta\sigma'_v \approx -7.5$ MPa. Applying these changes to the initial conditions, $\sigma_v = 20$ MPa, $p = 8$ MPa, and $\sigma_h = 20.5$ MPa; the stress condition has changed from normal ($\sigma_v = \sigma_1$) to thrust ($\sigma_v = \sigma_3$). The stress path is sketched on **Figure 29**, as well as stress paths for two other values of Poisson’s ratio – 0.20 and 0.35 – the latter considered more appropriate for shales.

In all eroded non-tectonic basins, such as the Michigan and Williston Basins on the US-Canada border, a “skin” has formed where instead of $\sigma_v = \sigma_1$, the conditions $\sigma_v = \sigma_3$ now exists. Depending on the amount of erosion and the initial state before erosion this “skin” is perhaps several hundred m to 1-2 km thick. This is why hydraulic fractures in shallow (< 500 m) gas sands or oil sands in Alberta tend to be horizontal, but deeper fractures tend to be vertical. A typical stress distribution with depth is shown in **Figure 30**. High pore pressures are quite rare in eroded basins.

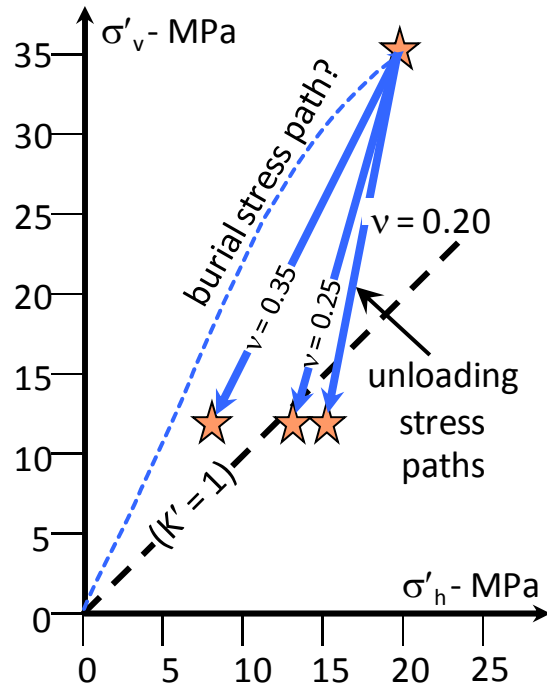


FIGURE 29: Stress path for elastic unloading arising because of erosion

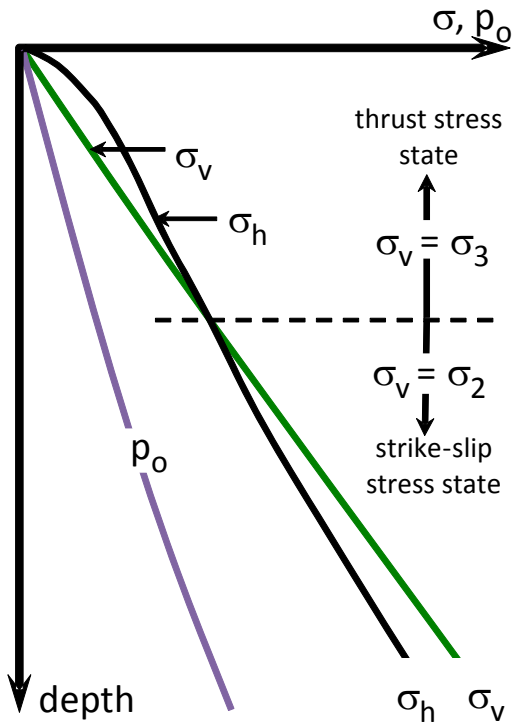


FIGURE 30: Stresses in an eroded basin

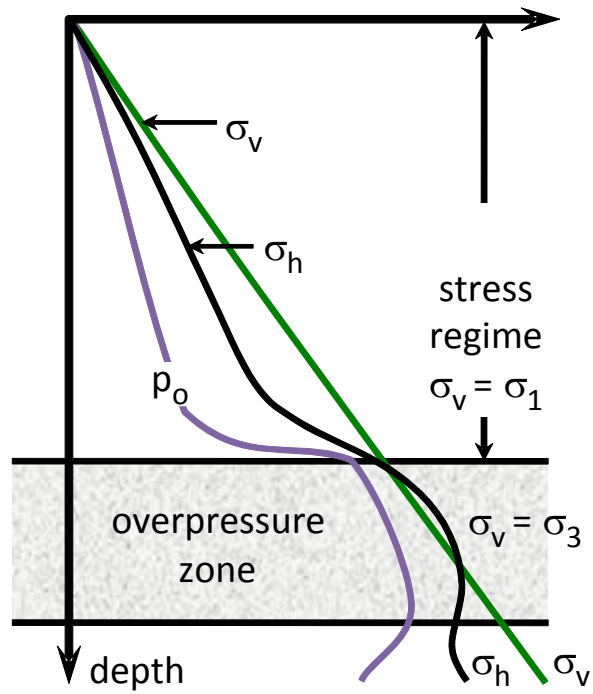


FIGURE 31: Stresses in a continental margin

Continental Margin Basin

Figure 31 shows the Gulf of Mexico model of stresses with depth in the listric faulting region. The major features are a normal fault regime near the surface changing to a thrust regime at depth, a highly overpressured zone in which the horizontal detachment fault is found (high p_o = low strength), and a stress “reversion” at depth related in part to lower pore pressures. In the overpressured regime the stresses are close to one another because of the elevated pore pressures and the ductility of the “under-compacted” sediments.

There are many other subtle features of the stress regimes of the GoM. Shallow gas sands only 300-1500 m below the sea floor are common, presenting great risks to drilling; these sands contain old catagenic gas (not shallow organic gas), indicating a deep pressure valving and hydraulic fracture process for emplacement. In the upper 4-5 km, above the overpressured interval, the pore pressures in shales are perhaps 10% higher than in the surrounding thick shales, so that if mud weight is kept just low enough to control sandstone pressures, shale sloughing acceleration is noted.

Salt diapirism can perturb the stress in a continental margin basin at a scale of perhaps 5-10 salt dome diameters around the dome (GoM, North Sea, off-shore Nova Scotia, etc.). **Figure 32** shows stresses near a salt dome, although highly complex salt structures also exist with components of faulting, horizontal salt emplacement, and so on. In this simple model, the large radial strain imposed on the rocks during domal emplacement means $\sigma_r = \sigma_1$ and $\sigma_\theta = \sigma_3$ near the dome stock (strike-slip). Above the dome, normal faulting is associated with extensional strain. During drilling near a salt dome, it is possible to pass from a normal fault regime through a thrust fault regime, and then into a strike-slip regime. For more complex, faulted cases also involving salt tectonics, the stress state with depth can be difficult to predict.

Compressional Tectonics Foreland Basin

Figure 33 shows a series of stress plots in a compressional foreland basin. Typical examples include Alberta and similar Rocky Mountain foreland regions, including the Andean foreland basins stretching from eastern Colombia to the southern tip of Argentina. Near the thrust faults, $\sigma_v = \sigma_3$ for considerable depths, eventually transitioning into a strike-slip regime at greater depth. Farther from the compressional front (100-200 km), the depth to the transition is shallower, and at great depth, it may be possible to encounter normal fault conditions. At great depth in the foreland syncline, pore pressures may be as high as $1.2-1.3 \times$ hydrostatic, but high overpressures are rare.

Transpressional Conditions

Two classic examples of strong transpressional conditions are the San Andreas fault system in southern California and the strike-slip faults of east-central Colombia (Cusiana Field) and western Venezuela (the Icotea fault passing through the middle of Lake Maracaibo). In these cases the strike-slip conditions appear to continue to great depth, and if the faulting is active and the rate of strain is large, the two horizontal stresses can approach values of $\sigma'_{HMAX}/\sigma'_{hmin} \approx 2.5-2.8$, essentially the condition of shear failure. In such tectonically active areas, massive shear failure and enlargement of boreholes during drilling is common, and the effects of depletion and injection can be startling, triggering small earthquakes or changes in fracture aperture because of shear distortion.

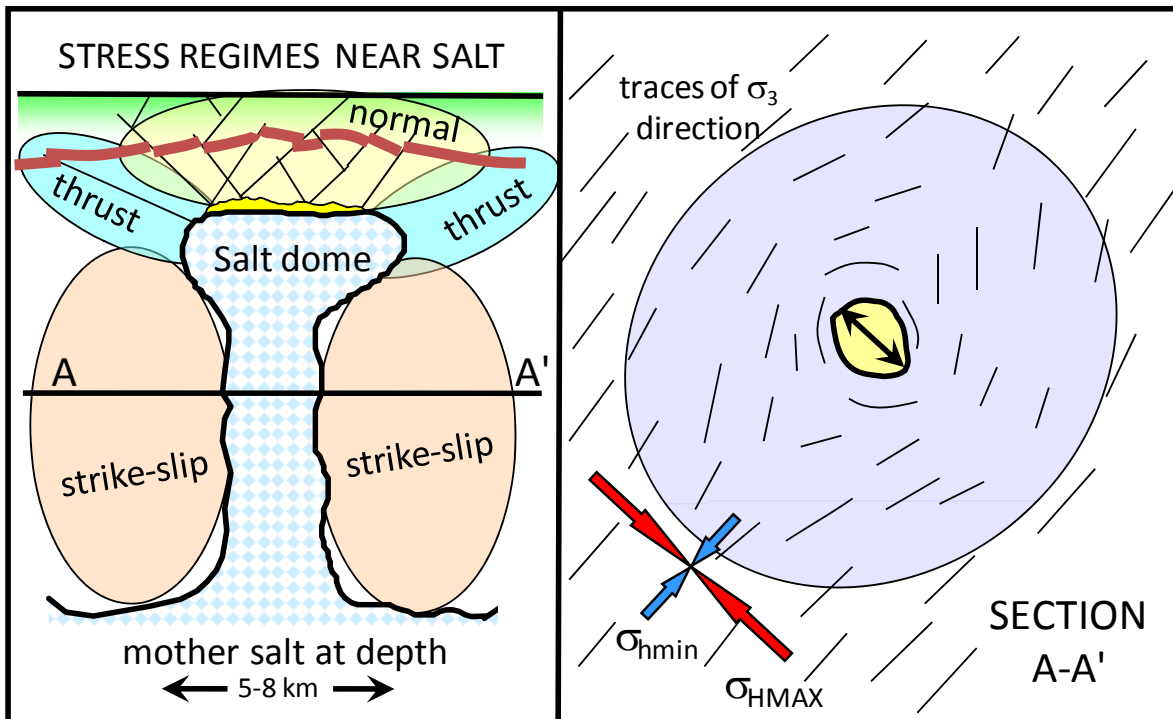


FIGURE 32: Because of the intrusion of the salt, compressive horizontal strains formed different stress regimes, depending on location. On a regional scale, the salt dome perturbs the stress regime for perhaps 4-6 dome diameters, depending on rock stiffness

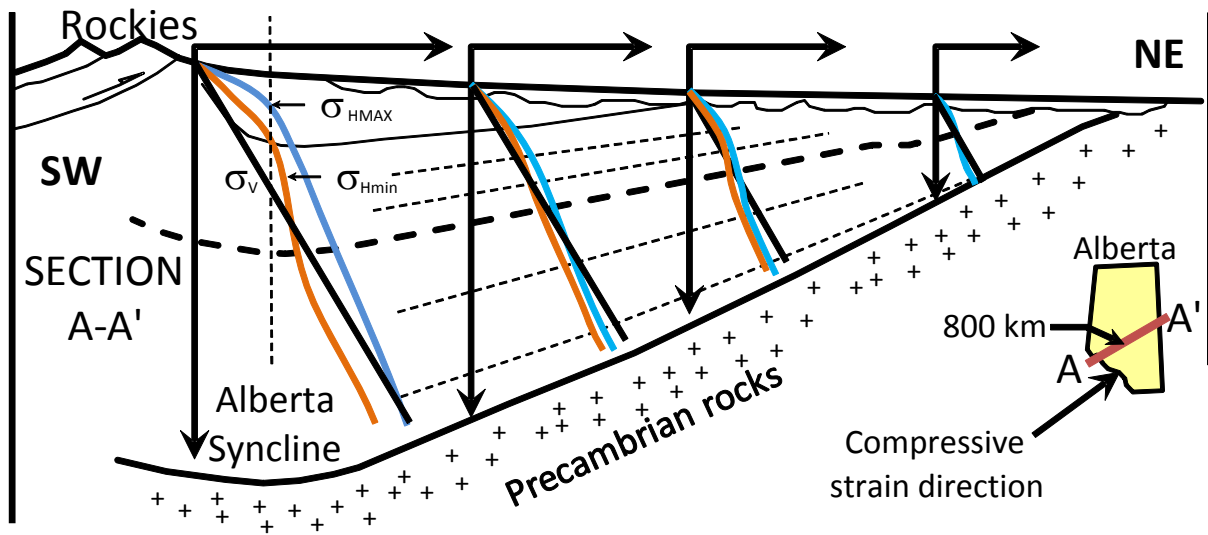


FIGURE 33: Stresses in a compressive foreland basin. Near the mountains, σ_1 is normal to the strikes of the thrust faults, and may be σ_{HMAX} for great depths. Away from the mountains, compressive strain effects persist, but less so than near the disturbed belt. (Blue line is σ_{HMAX} , red line is σ_{hmin})

2.3.1.7 Thermal and Pressure Effects on Reservoir Stresses

Drilling often has to take place through zones that are depleted or subjected to temperature changes. A brief discussion of some effects is given here.

Depletion of a flat-lying extensive reservoir involves conditions of no-lateral-strain, constant σ_v , and a pressure drop Δp . Applying these in a linear elastic model leads to prediction of a Poisson's ratio-controlled lateral total stress loss during depletion:

$$\Delta\sigma_h = \frac{1-2\nu}{1-\nu} \cdot \Delta p \text{ (as well as } \Delta\sigma'_v = \Delta p \text{ and } \Delta\sigma'_h = \frac{-\nu}{1-\nu} \cdot \Delta p) \quad (2-44)$$

This is known as the reservoir stress path, and the multiplier of Δp in the equation is known as the stress path coefficient, often taken as 0.67 (for $\nu = 0.25$). In practice, the stress path coefficient is known to vary substantially, from values as low as 0.45 to as high as 1.1 in cases where there is stress-triggered fabric breakdown. For intact sandstones, a stress path coefficient of 0.65-0.75 is recommended, and for intensely fractured reservoirs, 0.8-0.9 may be used for preliminary estimates. Using typical values for Δp shows that secondary drilling through the zone may result in lost circulation, particularly if it is necessary to maintain a high drilling fluid density because of thin high pressure gas zones above the reservoir (**Figure 34**). It is possible to “restress” a region around the borehole through controlled injection of solids such as lost-circulation material, cuttings, mud solids or CaCO_3 , until a stress cage develops around the hole, reducing the tendency for hydraulic fracture. This process may help avoid additional casing strings and reduce blowout risk, but it is a delicate procedure.

Depletion of very large volumes can lead to triggering of normal fault earthquakes, particularly if the reservoir was initially in a stress state close to yield. Of course, injection leads to similar changes but with different signs, until the condition of $p > \sigma_3$ is reached, at which point hydraulic fracture can be expected (shear yield can precede reaching the fracture condition in rocks of low cohesion). At high injection pressures, bedding plane slip (a form of thrust faulting) can be triggered, perhaps leading to casing shear.

Heating the reservoir through injection of hot fluids (ΔT as much as 250°C in the case of steam injection at $z = 500$ m) leads to huge increases in lateral stresses, and simple elastic calculations show that the shear strength limit is soon reached, such that σ_v becomes σ_3 and thrust fault slip conditions limit the stresses. Drilling into a hot reservoir not only carries risks associated with heat, but also borehole problems if the lateral stresses are at the yield point.

Cooling the reservoir is usually associated with water disposal, and ΔT of -30 - 50°C is feasible. Loss of lateral stress combined with the injection pressure means the condition $p > \sigma_3$ ($= \sigma_{hmin}$) can be easily reached, so that hydraulic fracturing takes place (more often, the opening of existing fractures). This invariably improves the performance of the injection well, but if a large cooled zone has to be drilled, lost circulation problems may be encountered.

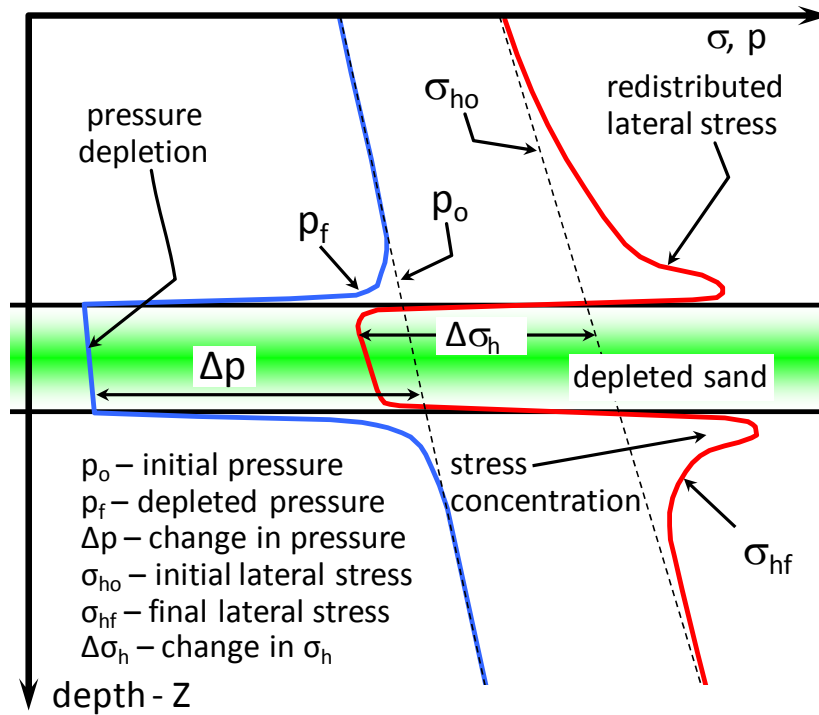


FIGURE 34: Reservoir depletion reduces the lateral stress. In this example, the lateral stress has been reduced below the pore pressure in surrounding strata, a difficult drilling condition.

2.3.2 Stresses around a Borehole

2.3.2.1 Elastic Stresses around a Borehole

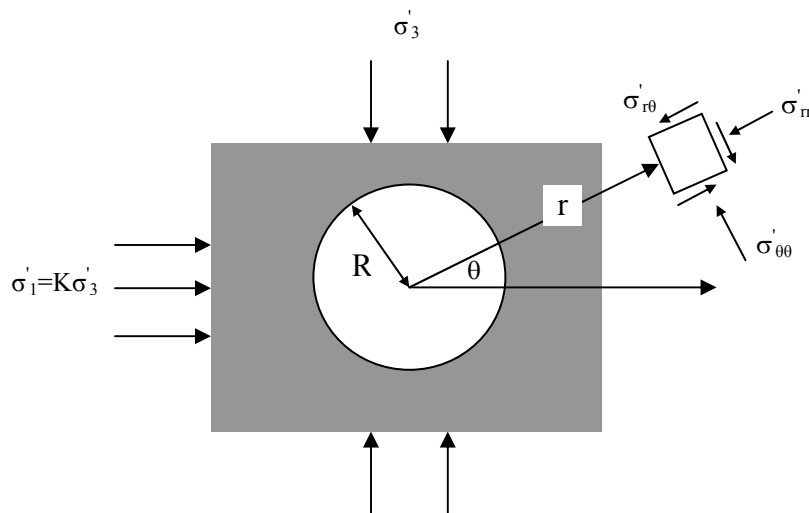


FIGURE 35: Initial Stress distributions around Wellbore [Brady and Brown, 1985]

According to Brady and Brown [1985], Kirsch originally derived the complete linear elastic solutions for the two-dimensional stress distribution and displacement field around a hole loaded by two principal stresses in the far field (**Figure 35**):

$$\sigma'_{rr} = \frac{\sigma'_3}{2} \left[(1+K) \left(1 - \frac{R^2}{r^2} \right) - (1-K) \left(1 - 4 \frac{R^2}{r^2} + \frac{3R^4}{r^4} \right) \cos 2\theta \right] \quad (2-45a)$$

$$\sigma'_{\theta\theta} = \frac{\sigma'_3}{2} \left[(1+K) \left(1 + \frac{R^2}{r^2} \right) + (1-K) \left(1 + \frac{3R^4}{r^4} \right) \cos 2\theta \right] \quad (2-45b)$$

$$\sigma'_{r\theta} = \frac{\sigma'_3}{2} \left[(1-K) \left(1 + \frac{2R^2}{r^2} - \frac{3R^4}{r^4} \right) \sin 2\theta \right] \quad (2-45c)$$

where σ'_{rr} , $\sigma'_{\theta\theta}$, $\sigma'_{r\theta}$ are the effective stresses around the hole, assuming pore pressure is constant. R is borehole radius; r , θ are cylindrical coordinates. σ'_1 is the maximum effective principal stress, while σ'_3 is the minimum effective stress. K is the ratio between them. For a vertical hole, σ'_1 and σ'_3 become maximum and minimum effective horizontal stresses (σ'_{Hmax} and σ'_{Hmin}).

When far field stresses are isotropic, i.e. $\sigma'_1 = \sigma'_2 = \sigma'_3$, the stresses near wellbore become

$$\sigma'_{rr} = \sigma'_3 \left(1 - \frac{R^2}{r^2} \right) \quad (2-46a)$$

$$\sigma'_{\theta\theta} = \sigma'_3 \left(1 + \frac{R^2}{r^2} \right) \quad (2-46b)$$

$$\sigma'_{r\theta} = 0 \quad (2-46c)$$

The difference between σ'_{rr} and $\sigma'_{\theta\theta}$ is: $\sigma'_{rr} - \sigma'_{\theta\theta} = -2\sigma'_3 \frac{R^2}{r^2} < 0$, which indicates σ'_{rr} is always less than $\sigma'_{\theta\theta}$. Further, the greatest stress difference occurs at the borehole radius $r = R$:

$$\sigma'_{\theta\theta} = \sigma'_3 [(1+K) + 2(1-K) \cos 2\theta] \quad (2-48a)$$

$$\sigma'_{rr} = 0 \quad (2-48b)$$

$$\sigma'_{r\theta} = 0 \quad (2-48c)$$

There is no effective radial stress at the borehole wall if it is a free boundary.

When far field stresses are isotropic, Eq. 2-48a becomes:

$$\sigma'_{\theta\theta} = (\sigma'_1 + \sigma'_3) + 2(\sigma'_1 - \sigma'_3) \cos 2\theta \quad (2-49)$$

If $\theta = 0$, $\sigma'_{\theta\theta} = 3\sigma'_1 - \sigma'_3$, while for $\theta = \frac{\pi}{2}$, $\sigma'_{\theta\theta} = 3\sigma'_3 - \sigma'_1$. These represent the greatest and the smallest values of the tangential stress at the borehole wall, and are used to estimate the initiation of a hydraulic fracture.

Bearing the above discussion in mind, the stress distributions around a wellbore in a plane are sketched in **Figure 36**. The dashed lines represent stress distributions that are perpendicular

to the direction of the minimum principal stress (σ'_3). The rock has been treated as an isotropic elastic material, temperature is constant, and the effect of fluid flow is neglected.

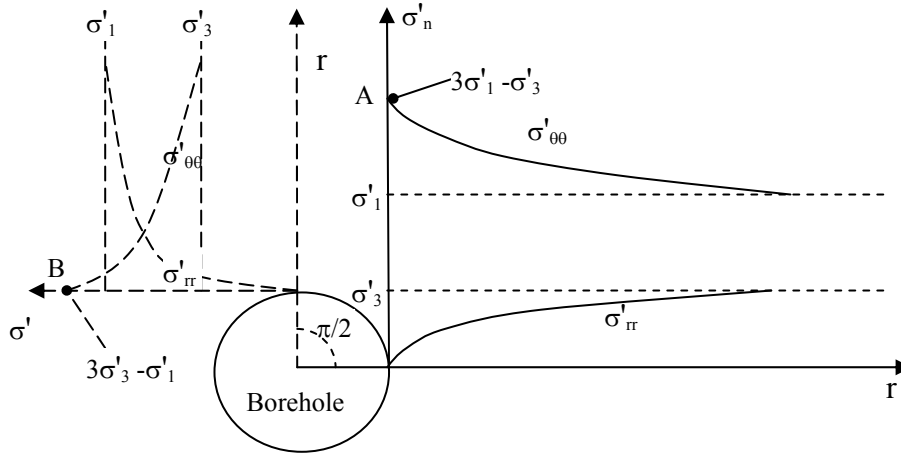


FIGURE 36: Stress distribution in the directions of $\theta=0$ and $\theta=\pi/2$ around a hole

2.3.2.2 Elastic Stresses around a Borehole with Fluid Flow

For an elastic isotropic formation, stress equilibrium around a borehole in cylindrical coordinates can be expressed as:

$$\frac{\partial \sigma'_r}{\partial r} + \frac{\sigma'_r - \sigma'_\theta}{r} = \alpha \frac{\partial P}{\partial r} \quad (2-50)$$

α is the Biot constant and fluid pressure P changes with location and time. The solutions for total stresses can be found as [Wang and Dusseault, 1991]:

$$\sigma'_r = \alpha P(r, t) + \frac{Ec_1(t)}{(1+\nu)(1-2\nu)} - \frac{Ec_2(t)}{(1+\nu)} \frac{1}{r^2} - \frac{1-2\nu}{1-\nu} \frac{\alpha}{r^2} \int^r r P(r, t) dr \quad (2-51a)$$

$$\sigma'_\theta = \alpha \frac{\nu}{1-\nu} P(r, t) + \frac{Ec_1(t)}{(1+\nu)(1-2\nu)} + \frac{Ec_2(t)}{(1+\nu)} \frac{1}{r^2} + \frac{1-2\nu}{1-\nu} \frac{\alpha}{r^2} \int^r r P dr \quad (2-51b)$$

Assuming steady fluid flow into the borehole, pore pressure varies only with radius and follows Darcy's rule:

$$P(r) = P_1 + \bar{K} \ln \left(\frac{r}{R_1} \right) \quad (2-52)$$

where $\bar{K} = \frac{Q\mu}{2\pi kh}$, R_1 is the wellbore radius, P_1 is the bottom flowing pressure. If flow rate Q is constant, effective stresses can be expressed as [Han and Dusseault, 2003]:

$$\sigma'_r = \frac{0.5\alpha}{1-\nu} P + \frac{Ec_1}{(1+\nu)(1-2\nu)} - \frac{Ec_2}{(1+\nu)} \frac{1}{r^2} + \alpha \frac{0.5-\nu}{1-\nu} \cdot \frac{\bar{K}}{2} \quad (2-53a)$$

$$\sigma'_\theta = \frac{0.5\alpha}{1-\nu} P + \frac{Ec_1}{(1+\nu)(1-2\nu)} + \frac{Ec_2}{(1+\nu)} \frac{1}{r^2} - \alpha \frac{0.5-\nu}{1-\nu} \cdot \frac{\bar{K}}{2} \quad (2-53b)$$

Coefficients c_1 and c_2 are variables only related to time and determined by boundary conditions. An appropriate condition is assuming the effective radial stress is zero at the borehole wall and equals the horizontal effective stress at far field (R_2):

$$r = R_1, \sigma'_r = 0; \text{ and } r = R_2, \sigma'_r = \sigma'_h \quad (2-54)$$

c_1, c_2 can be shown to be

$$c_1 = \frac{(1+\nu)(1-2\nu)}{E} \left[\frac{R_2^2}{R_2^2 - R_1^2} (\sigma_h + \alpha \frac{0.5-\nu}{1-\nu} P_2 + \frac{R_1^2}{R_2^2} \frac{0.5\alpha}{1-\nu} P_1) - \alpha \frac{0.5-\nu}{1-\nu} \cdot \frac{\bar{K}}{2} \right] \quad (2-55a)$$

$$c_2 = \frac{1+\nu}{E} \cdot \frac{R_2^2 R_1^2}{R_2^2 - R_1^2} \left(\sigma_h + \alpha \frac{(0.5-\nu)P_2 + 0.5P_1}{1-\nu} \right) \quad (2-55b)$$

One example of the elastic stress solutions is plotted as dotted lines in **Figure 37**.

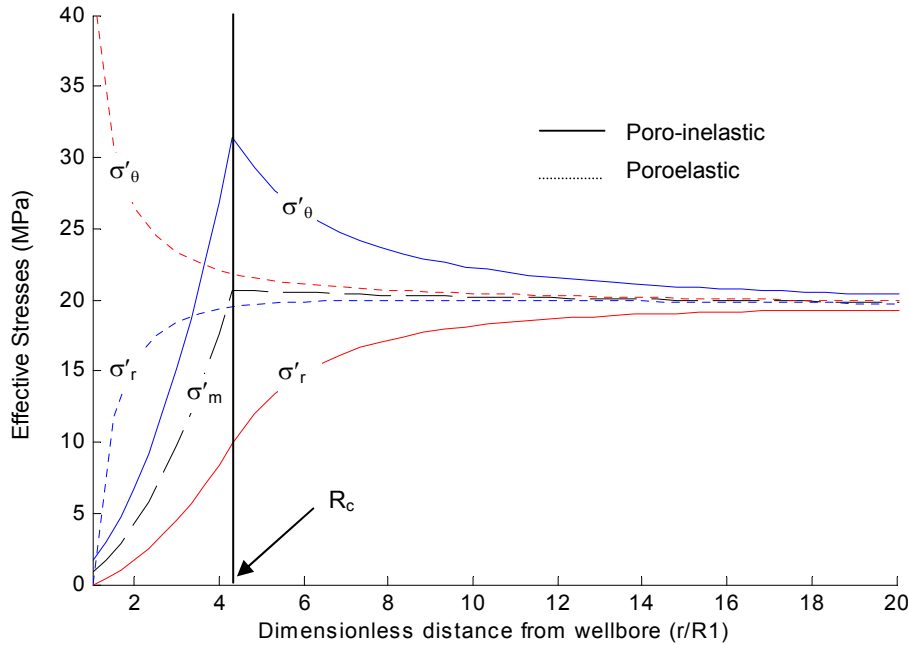


FIGURE 37: Effective stresses, σ'_r and σ'_θ , around a borehole: dotted lines are poro-elastic solutions, solid lines are poro-inelastic solutions. σ'_m is the average of the two stresses [Han and Dusseault, 2003]

2.3.2.3 Inelastic Stresses around a Borehole with Fluid Flow

The previous solutions are based on the assumption that the formation is elastic and that no failure occurs. However, weak or unconsolidated rocks are more likely to be yielded and mobilized by stresses and fluid flow, which may lead to borehole collapse for example.

Assuming the rock stresses around a borehole in a weak rock formation satisfy the Mohr-Coulomb failure criterion, the stress solutions have been found [Han and Dusseault, 2003]

$$\sigma'_r(r) = \frac{c_3}{\omega} r^{-\omega} + \frac{2C_o \tan \beta + \alpha \bar{K}}{\omega} \quad (2-56a)$$

$$\sigma'_\theta(r) = \frac{c_3(1-\omega)}{\omega} r^{-\omega} + \frac{2C_o \tan \beta + (1-\omega)\alpha \bar{K}}{\omega} \quad (2-56b)$$

where $\omega = 1 - \tan^2 \beta$. The constant c_3 could be given as:

$$c_3 = -(2C_o \tan \beta + \alpha \bar{K}) \cdot R_1^\omega \quad (2-57)$$

Plotting and comparing these to their poroelastic counterparts (**Figure 37**), the inelastic stresses shift the concentration of shear stress away from the wellbore. A Coulomb zone has been identified and defined through a critical radius R_c . In this zone, rock has yielded and been damaged to certain extent but has not completely lost its functionality and fallen into the borehole. For strong rock with low in-situ stress magnitude, the Coulomb zone may not exist.

The analytical solutions for the inelastic case have to assume isotropic far field stresses (i.e. $\sigma'_{Hmax} = \sigma'_{hmin}$) to avoid prohibitive mathematical challenge. For anisotropic far field stresses $\sigma'_{Hmax} > \sigma'_{hmin}$, numerical solutions of rock deformation around a pressurized vertical borehole is plotted in **Figure 38**. Instead of evenly distributing around the borehole in the isotropic case, rock deformation concentrates in the direction perpendicular to the maximum horizontal stress. These concentrated deformation zones near the wellbore have the highest risk of borehole collapse or instability, comparing to the rest formations around the hole.

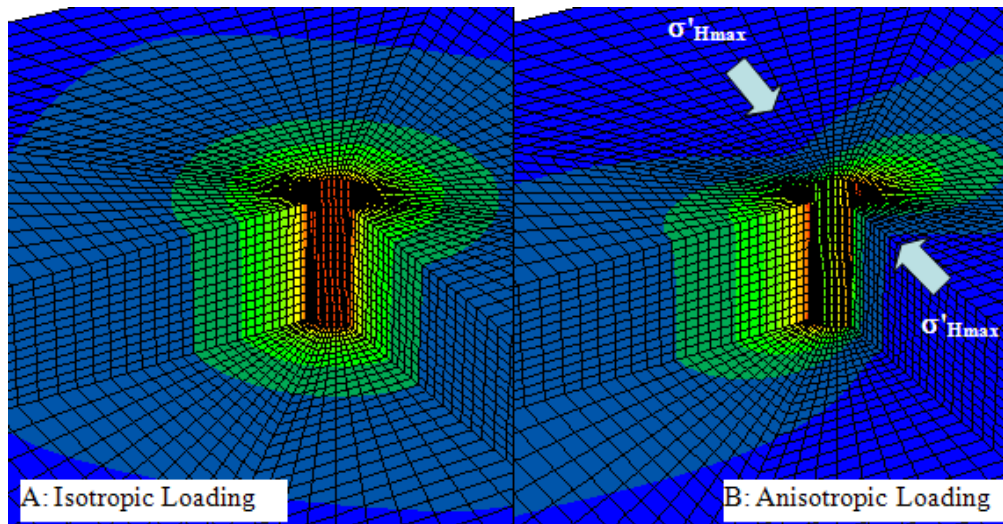


FIGURE 38: Rock deformation around a borehole when A: Isotropic loading ($\sigma'_{Hmax} = \sigma'_{hmin}$), B: Anisotropic loading ($\sigma'_{Hmax} > \sigma'_{hmin}$)

2.3.2.4 Heating and Cooling the Borehole

Thermal exchange between drilling fluid and rock occurs naturally. **Figure 39** is a simplified sketch of the drilling fluid and *in situ* rock temperatures that might be encountered during drilling on land. Offshore, the temperatures are greatly complicated by the cooling and heating that occur in the section of the riser that makes contact with sea water, which can be on the order of 1-4°C at the sea floor in deep offshore drilling.

Clearly, there can be a large difference between the mud temperature and the formation temperature. Below the cross-over point in **Figure 39**, the returning drilling fluid is cooler than the formation temperature. This has the following effects:

- Transient reduction of the temperature in the borehole wall rock
- Reduction in the rate of diffusion processes, such as:
 - Reduction of creep rates in salt
 - Increase in the viscosity of pore fluids
 - Reduction of shale reaction rates (e.g. adsorption-desorption reactions)
- Slight thermoelastic shrinkage of the rock, leading to a significant drop of the effective tangential stress σ'_θ in the near-borehole region

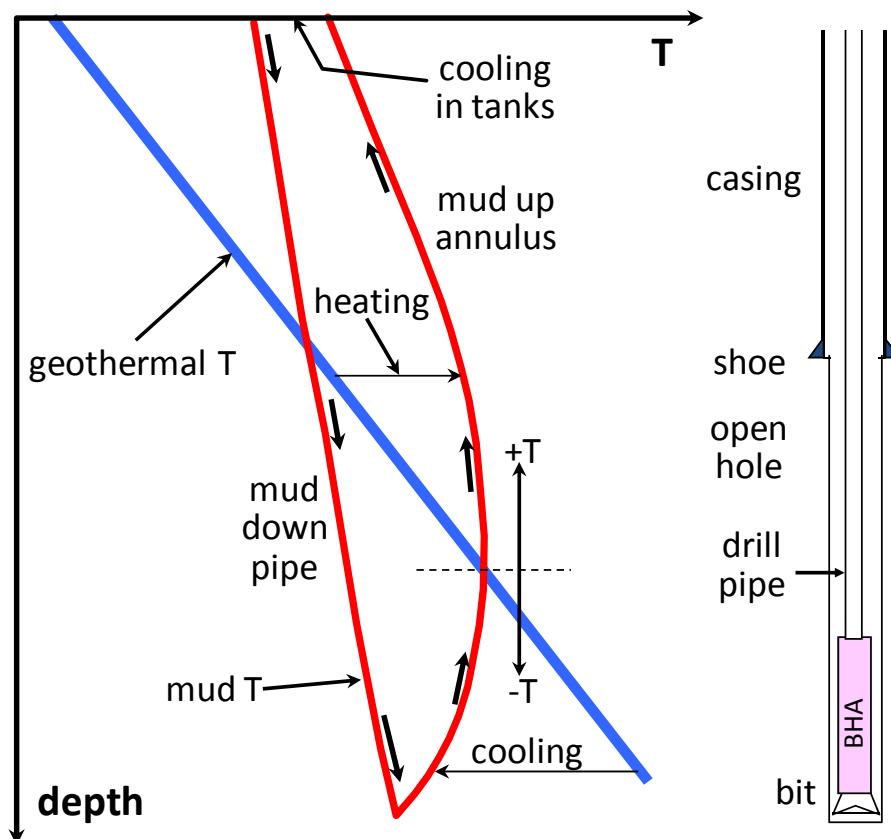


FIGURE 39: Drilling involves cooling the rock in the drill-bit region, helping stabilize the hole, while heating the rock higher in the borehole, potentially destabilizing the rock

This effect can be a major advantage for a drilling operation, reducing the rate of bottom-hole sloughing, mass transfer, and related problems. On the other hand, consider the drilling fluid temperature at the casing shoe in **Figure 39**; it is much higher than the formation temperature, and this causes effects opposite to those listed above, which in many cases are known to lead to accelerated sloughing and hole-cleaning problems [Wang and Dusseault 2003].

Figure 40 shows approximately the shape of the tangential stress distribution one might expect from heating or cooling the borehole wall. In the heating case, the heated zone expands, so the maximum compressive stresses are increased massively, and usually the shear stresses also increase. When a wellbore is subject to cooling, however, rock around the hole shrinks and therefore the tangential stress decreases. The specific shape depends on the magnitude of convective versus conductive heat flow, although it is reasonable to assume that in the case of boreholes, conductive heat flux dominates, whereas in cases of injection and production into permeable reservoirs, convective heat flux dominates.

For a quick approximation of how much the σ'_θ values in the wall can change, the following thermoelastic equation can be used, but only on the borehole wall.

$$\Delta\sigma'_\theta]_{r=R} = \frac{\Delta T \cdot E \cdot \beta_T}{1 - \nu} \quad (2-58)$$

Here, β_T is the linear coefficient of thermal expansion, usually about $10\text{-}15 \times 10^{-6} \text{ }^\circ\text{C}^{-1}$ for shale, E is Young's modulus, usually in the range of 5-100 GPa for most deeper sedimentary rocks (lower porosity \rightarrow higher stiffness), ΔT is the difference in temperature between the drilling fluid and the virgin rock temperature, and ν is Poisson's ratio. The change in tangential stress given by eq. (2-58) is only valid at the borehole wall; where it is usually supposed that conditions are the most critical.

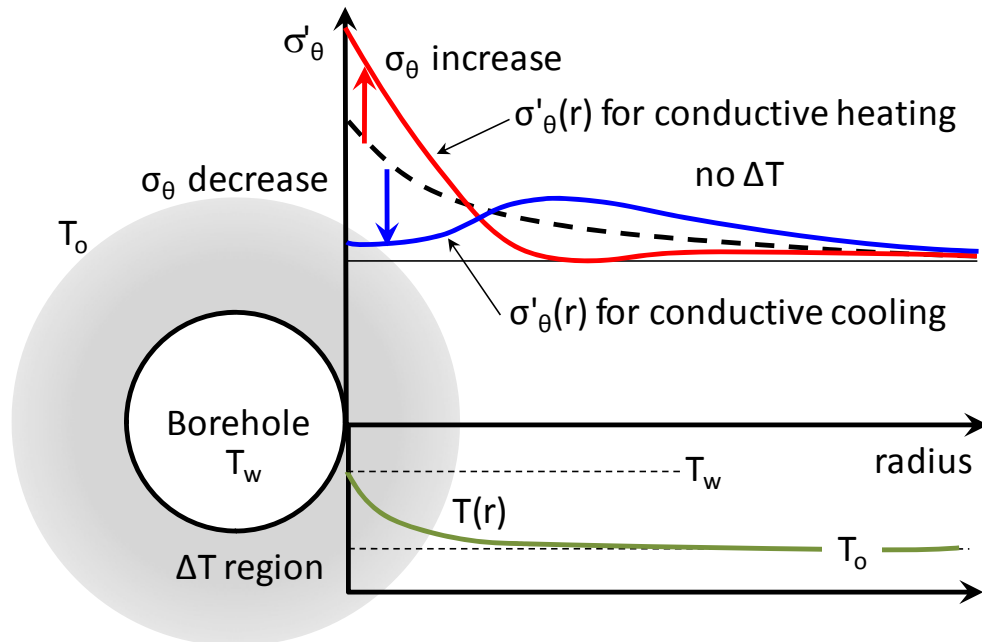


FIGURE 40: Tangential stresses near the borehole wall are dramatically altered if the drilling fluid temperature is changed. Heating leads to shear failure, cooling leads to stability.

2.4 Theories of rock breakage

The literature on rock drilling often includes such terms as “grinding”, “wearing”, “ripping”, “ploughing”, “cutting”, “breaking”, “shearing”, “scraping”, “fracturing”, and “chipping”. In this section, we will review various drilling methods with focuses on percussion drilling and rotary drilling.

2.4.1 Percussive

2.4.1.1 History

Developed by the Chinese more than 4000 years ago, percussion drilling is basically raising and dropping heavy piercing tools to penetrate rocks. The Chinese used a cutting head secured to bamboo rods to drill to depths of 915 m. The raising and dropping of the bamboo drill string allowed it to impact and fracture the less dense rock formations. It was reported to often take two to three generations of workers to complete large wells [Treadway, 1997].

In 1859 at Titusville, Pennsylvania, Colonel F. L. Drake completed the first oil well using a cable tool percussion-type machine. One of the earliest reports of percussion drilling technique occurred in 1949 [Harpst and Davis, 1949]. Since then different terms have been used, such as downhole hammer, percussion hammer, Down-The-Hole hammer, percussive drill, percussive-rotary drill, etc.

Major development and research have been reported between 1950s and 1960s [Wanamaker, 1951; Faihust and Lacabanne, 1956; Topanelian, 1957; Fish, 1961; Simon, 1964; Hartman, 1966; McGregor, 1967]. Understandings of the percussive mechanism have been significantly improved in lab. Some single-well applications have been reported in oilfield for the purpose of demonstrating the effectiveness of percussive drill [Smith and Kopczynski, 1961; Bates, 1964].

Mainly because of frequent mechanical failures, poor understanding and therefore control of drilling operations, and economical uncertainties, wide application of hammer drilling technology to oilfield was not reported until 1980s. In 1987, Pratt reported that air hammers were tested on 27 wells in Alberta and British Columbia. The average time to total depth for recent air/mud drilled wells at one location has been 80 days (best 66 days), compared to the record rotary drills which took 103 days. Whiteley and England [1986] also showed the field applications of air hammer in the Arkoma basin, which has significantly improved drilling operations including a large increase in ROP, a substantial reduction in cost per foot, improved hole geometry, and reduced drillstring stresses.

Since 1990s, wells have been drilled deeper and deeper to exploit hydrocarbon resources, and consequently drilled rocks become harder and harder. Hydraulic hammer or water hammer has been developed to accommodate these new challenges and efficient mechanical designs have been achieved [Kong et al., 1996; Giles et al., 2001; Tibbitts et al., 2002]. These designs, however, are still in pre-field stage.

Throughout its history, theoretical development of percussion drilling technology has been relatively lagged behind, comparing to its improvement in mechanical designs. This phenomenon is not uncommon in drilling industry as the integrated process of rock drilling involves so many disciplines and complicated physics that rigorously modeling it faces prohibitive theoretical challenges.

2.4.1.2 Pros and Cons

It has been widely recognized that percussion drilling (even without rotary) could result in a faster penetrating speed than conventional means such as rotary drill or diamond drill, especially in some hard formations such as siliceous granite, sandstone, limestone, dolomite, etc [Whiteley and England, 1986; Pratt, 1987]. With the same rotation and WOB the percussive-rotary method is 7.3 times faster than the conventional rotary method in a medium-hard granite, while at the best operational conditions for both methods, percussive-rotary has a 2.3 times advantage in ROP over the rotary [Melamed et al., 2000].

The facilitation is mainly due to the effects of frequent blows and high impact loads through bit teeth, and chipping of rock from a clean surface with the bit rotation. Other advantages of percussion drilling are

- Static and lower WOB. For example, ROP of 3.3m/h was achieved with the 8^{3/4} inch bit when WOB is 4.5 ton, while in rotary drilling mode 18.5 ton of WOB is needed to achieve the same ROP [Melamed et al., 2000].
- less contact time with rock, only 1 or 2 percent of total operational drilling time [Bates, 1964; Melamed et al., 2000], lead to a less abrasion of the bit therefore a longer bit life.
- less hole deviation and easier control of deviation problem for straight hole drilling.
- Larger cuttings may be generated, giving a better representation for geological study. Meanwhile large-sized chips may lead to hole cleaning problem in the fast drilled large holes [Pratt, 1987].
- Some potential applications of percussion drilling have been proposed. For example, the impact of the hammer may transmit mechanical impact waves to the rock through drill bit, generate hydraulic pressure fluctuations in borehole (**Figure 41**), and provide a steady seismic signal at the hole bottom. Vibrational energy can be seen in the 10-20 kHz range, which is used to estimate porosity, rock elastic moduli, and synthetic seismograms for comparison with surface seismic data. [Minear et al., 1996]. Hammer may be also used as a steerable drilling device that provides down-hole rotation [Bui et al., 1995], or be exploited for down-hole electricity generation, down-hole high-pressure jet intensification, etc.

Because of these attractions, it has been predicted that "...The combination of rotary and percussion-type drilling could make a frontal attack into the drilling technology and open a new era of drilling" [Samuel, 1996].

On the other hand, inclusive overall results, risks in operation (such as mechanical failure), and economical uncertainties greatly hinder the acceptance of percussion drilling technology, even it has been a focus in rock drilling for a long time. There are many unclear but critical issues yet to be solved, such as unreliable estimation of optimized values for hammer type, number of blows, energy per blow (which is directly related to length of the stroke, area of piston, supplied pressure), etc; wellbore stability issues associated with excessive hammer energy; poor performance in soft rocks; severe vibration to the drill string and the rig structure; less field evidence of reliable and continuous operations of percussion hammers, comparing to the rotary drilling.

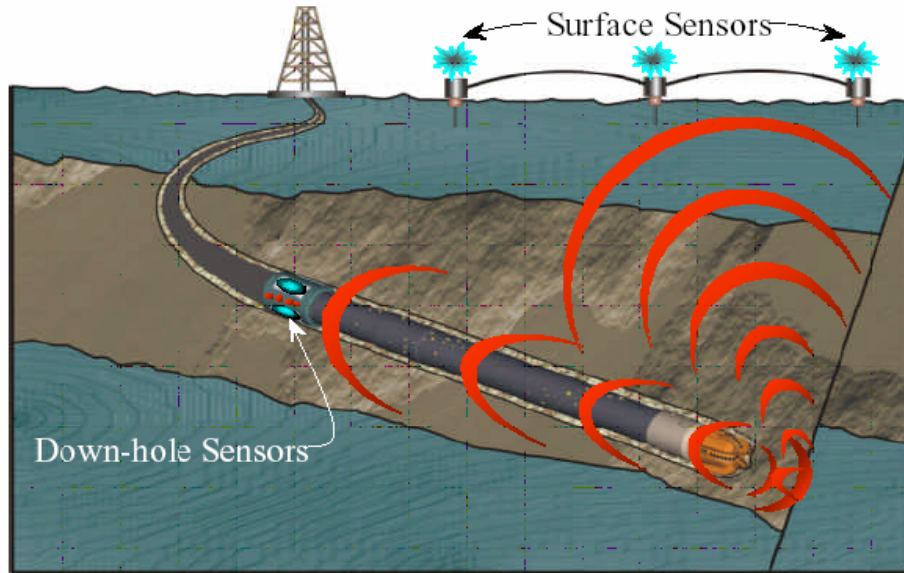


FIGURE 41: Percussion hammer seismic [after Pixton and Hall, 2002]

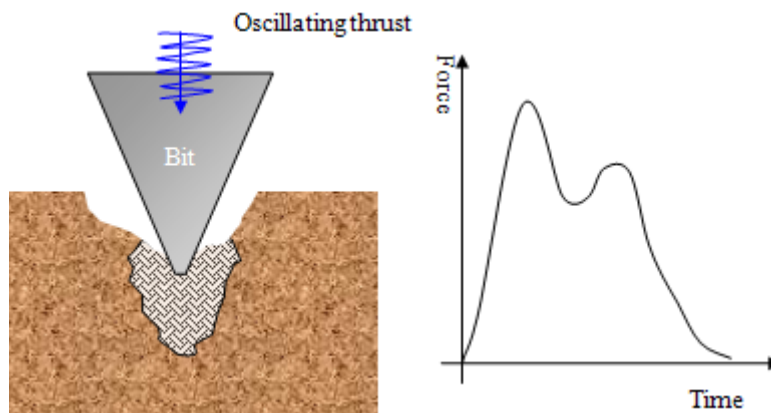


FIGURE 42: Illustration of a percussive drill (left) and a force response in bit.

2.4.1.3 Physics of Rock Breakage in Percussion Drilling

Percussion drilling involves four fundamental processes: 1) drillbit penetrates rock with compression and vibration; 2) rock receives impact, stress propagates, and damage accumulates; 3) rock fails and disaggregates; and 4) cuttings are transported away from the bit and up in the annulus. These are coupled physical processes, with different physics related to the tool and bit mechanics, rock mechanics, and cuttings transport mechanics.

Unlike conventional rotary drilling, where Weight On Bit (WOB) first forces the bit cutters to penetrate the rock in the direction normal to the bit movement, and then the cutters shear off a conchoidal chip of the penetrated rock as the bit rotates, the percussion bit can generate much higher impact force along the direction of bit movement (**Figure 42**). When the force exceeds rock strength, it crushes the rock below the bit and creates fractures forming a narrow wedge along the outer boundaries of the bit inserts. The cratered zone may extend to a depth several times greater than the actual depth of bit penetration.

Dynamic Stress Generation and Propagation

There is limited dynamics stress data during bit-rock impact, especially close to the impact location. The photoelastic method was first applied to analyze elastic stress behavior of rock under drilling loading conditions [Somerton et al., 1961; Reichmuth, 1963]. Oscilloscope traces were then used to record rock displacement in a few milliseconds during indentation test [Podio and Gray, 1965]. With improvement of instruments, high frequency data from an impact steel rod was recorded in a recent indentation test [Green et al., 2005]. Overcoming the difficulties to setup the measurement device, the high impact force, high frequency dynamic stress wave inside the rock has been first recorded recently during hammer impact [Han et al., 2006].

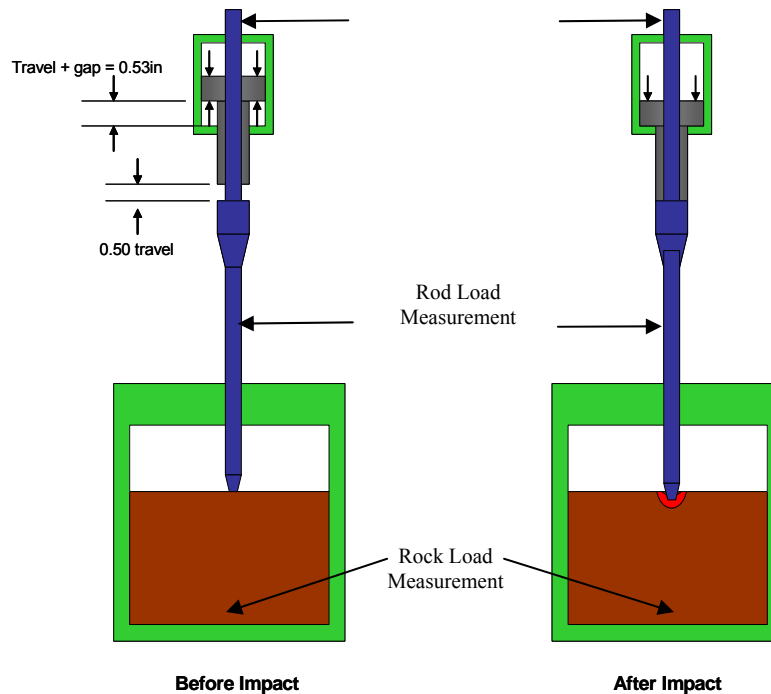


FIGURE 43: Schematic representation of test setup for single impact tests [Han, et al., 2006]

Figure 43 shows a schematic of single impact test performed on a Single Insert Impact Tester [Green et al., 2005]. Rock sample is loaded inside a pressure vessel, and exposed to drilling mud under various pressures. A conical single cutter is located tightly against rock at a given pre-load. A steel anvil with the single insert attached at the bottom extends out of the pressure vessel and upward through a hollow piston. A gas driven piston is used to strike a shoulder on the anvil. This impact sends a compressive stress wave down the anvil, through the insert, and into the rock. Three measurements can be taken simultaneously: load in the steel rod (ILoad) measured by a load cell located outside the pressure vessel, displacement of the rod (IDispl) by a high frequency-high resolution laser measuring device on the upper end of the anvil, and load at the rock bottom by a rock load cell (RLoad) pre-loaded against rock bottom directly in line with the insert impact. Data is recorded at a high frequency of 91 KHz.

In a test with Berea sandstone exposed to air, the impact stress in the steel rod (IStress), and the dynamic stress in the rock (RStress) are plotted in **Figure 44**. The magnitude of stress wave generated by the piston can reach as high as 120kpsi (827.4 MPa) in the steel rod, oscillating at

about 3 kHz frequency. After passing from the rod to the rock, the stress wave gradually loses its energy due to rock damping effect [Han et al., 2005b]. After approximately 0.12 milliseconds the wave reaches the rock bottom, and rock stress reduces to less than 1100 psi (7.6 MPa). Even though the loading stress in the rod diminishes after 0.01 sec, the rock stress oscillates around 700 psi (4.8 MPa) because of the remaining gas pressure in the vessel.

Figure 45 describes the first stress wave in the rod, as well as its displacement during the first cycle of the impact. Rod deformation increases first, levels off after the stress in the rod becomes tensional and keeps increasing when next cycle of compressive waves arrives.

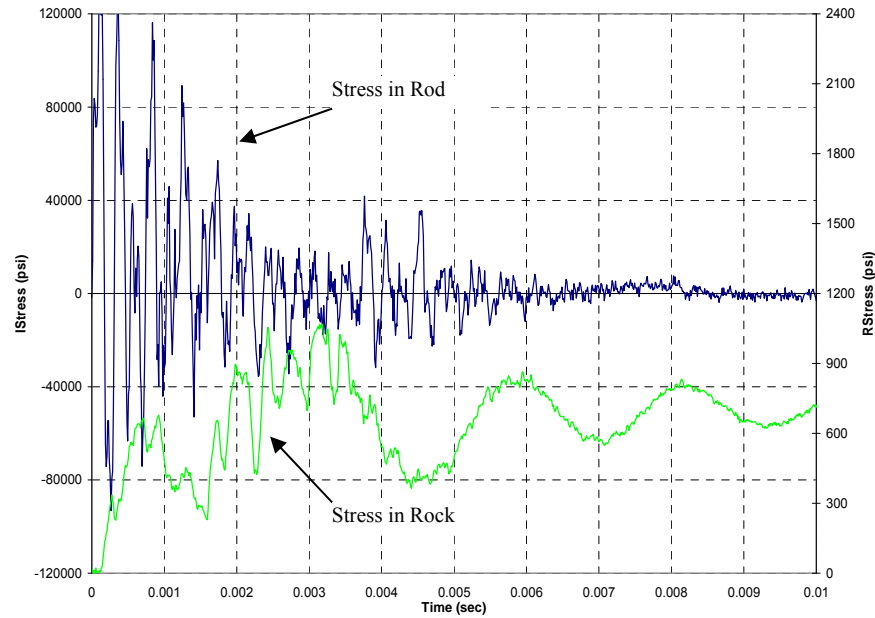


FIGURE 44: Compressive stresses recorded in the rod and the rock in a single impact test with 0 psi confining stress and 0psi pore pressure [Han et al., 2006]

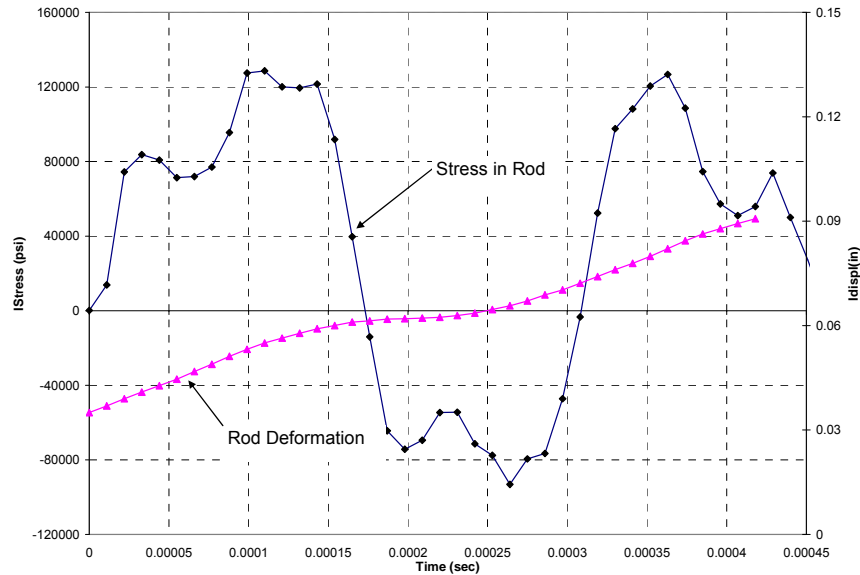


FIGURE 45: Compressive stress and displacement of the rod [Han et al., 2006]

Rock Damage and Defragmentation

When the insert impacts rock, some of stress waves are transferred from rod to rock while the other waves are reflected and dissipated mechanically and thermally. Upon receiving impact, rock deforms elastically when impact stress is less than rock strength. Once loading stress is high enough, however, rock starts to yield, fail, and disaggregate. Some examples of damaged rock from indentation tests with different lithologies are shown in **Figure 46**.

To investigate the effect of repetitive percussion on rock penetration, three impacts are loaded sequentially on the same location on the rock surface. After each impact, the depth and width of craters are measured, and debris is washed out so that a fresh rock surface can be exposed for the next impact. It is found that the repetitive percussion may affect rock penetration in different ways in different rocks. For Berea sandstone, the crater depth after each impact increases with the number of impacts, indicating that the rock becomes weaker due to cyclic loading [Han et al., 2005b]. For Mancos shale, however, the crater depth decreases with the number of impacts. Since the energy level of each impact is constant, this indicates the rock, instead of being weakened by repetitive loadings, is actually stronger than the original. The discrepancy may result from the difference of the rock structures. Berea sandstone is a porous (porosity is 20%) and medium strength rock (UCS is 6657 psi or 45.9 MPa). Sand particles can easily shift and rearrange themselves to accommodate impacting energy. Therefore micro-fissures are easily introduced during particles shift and the rock becomes damaged. On the other hand, Mancos shale is a more compact (porosity is only 7.9%) and highly layered rock with higher strength (UCS is 8079 psi or 55.7 MPa). When hammer impacts the shale, the shale particles are more restricted and likely crushed into smaller powders instead of moving to a porous space. Crushed particles, as a new material with smaller particle size, have more strength and higher density than the original rock, which explains why Mancos shale becomes stronger after each loading.

These findings are one example that demonstrates the complexity of percussion drilling. Hammer performance is not only related to cutter and bit design and the percussive energy level that a hammer can create, but also to rock mechanical properties, flow properties, and rock texture. Different rocks could have similar strength, but a hammer may perform quite differently due to the difference of rock textures.

Besides single indentation tests, drilling tests on similar scale to what is used in oil and gas fields are also conducted. The testing facility could provide field downhole conditions such as high confining stress and high fluid pressure [Green et al., 2005]. During test, as many as 16 drilling and fluid parameters can be recorded, such as penetration per revolution, torque, weight on bit, rotary speed, borehole pressure, flow rate, fluid temperature, overburden stress, confining pressure, etc. Data can be recorded at a frequency of 1 Hz, or at a high rate of 2,000 Hz for a short period. Both Berea sandstones and Mancos shales are tested. Each sample is 15 inches (39.4 cm) in diameter and 36 inches (91.4 cm) in length. An industry mud hammer bit is applied to drill each sample under various bottom hole pressures.

Figure 47 illustrates the hammer, a drilled rock sample, and collected cuttings. To compare, the cuttings collected from a roller-cone drilling, a hammer drilling, and a penny coin are laid side by side. Even though the size of the cutting from the hammer bit is smaller than that from the roller-cone bit, it is as thin as a penny coin while the cuttings from the roller-cone bit is a chunk. This may indicate different failure mechanisms involved in each drilling method, as discussed below.

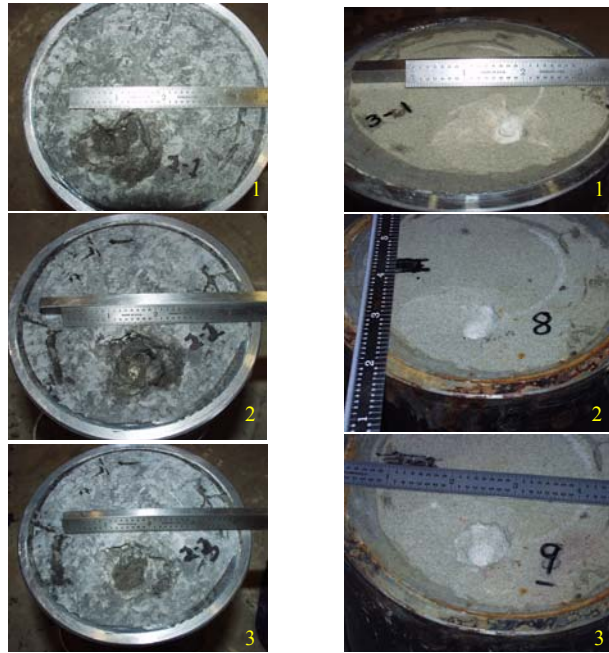


FIGURE 46: Indented rock samples after three impacts at the same location (left: Mancos shale; right: Berea sandstone) [Han et al., 2006]



FIGURE 47: Mud hammer bit (top left), drilled samples (top right), and cuttings collected (bottom left) in a full-scale hammer drilling test [Han et al., 2006]

2.4.1.4 Rock Failure Mechanisms during Percussion Drilling

Before further discussion of rock failure, it is necessary to clarify two terms that are often misused: rock yield and failure. Yield refers to a process of accumulation of shear bands or microfissures developed as rock starts to gradually lose its ability to support load, whereas failure means collapse and total loss of strength.

During percussion drilling, rock failure develops at and near the impact location. Unfortunately rock stress and deformation around the location is almost impossible to measure

without damaging device. Numerical simulations have been designed to help address rock defragmentation after receiving impacts [Han et al., 2005a; Han et al., 2005b; Han and Bruno, 2006]. Rock failure could occur due to 1) excessive compression and crushing; 2) excessive shear stress and particle movement; 3) excessive tension and fracturing; and, 4) cyclic loading and damage accumulation.

Compressive Failure

A critical compressive strain is proposed to describe when rock crushes due to excessive compressional strain in loading direction:

$$\varepsilon_{zz} > \bar{\varepsilon}_z \quad (2-59)$$

where ε_{zz} is calculated compressional strain in loading direction, and $\bar{\varepsilon}_z$ is the critical strain value determined from lab testing (e.g. $\bar{\varepsilon}_z = 0.006$ for a Berea sandstone).

High impact stress passes from indenter to rock in a compressive nature. **Figure 48** illustrates the distribution of compressive stress (in this case it is the vertical stress) in both the indenter and the rock adjacent to the impact point in a single indentation test. The diameter of the impacting cone is 0.25 inches (0.00635 m). The small indenter head, along with the rigid indenter-rock interface, greatly increases the impact stress from its original 20 kpsi (137.9 MPa) at the stroked anvil to as high as 212 kpsi (1461.5 MPa) at the indenter tip. The measured indentation depth is about 0.24 inches (0.0061 m), which is well covered by a conical shaped stress concentration zone (the blue and green elements in **Figure 48**)

Besides the vertical compressive stress, the vertical strain along the impact direction is also studied in **Figure 49**. Clearly a highly indented zone (colored in blue and dark green) is developed under the impact. This zone reaches well beyond the cutter penetration itself. It is the stress superposition under the cutter that help rock failure extends as deep as several cutter diameters in hammer drilling. More interestingly, there are some zones (colored in red) showing opposite deformation: moving against the direction of the impact force. These elements are outside the conical compressive strain zone and in tension state.

Tensile Failure

The fact that rock could fail in tension despite it has been compressively loaded in percussion drilling is not new [Fairhurst and Lacabanne, 1956; Reichmuth, 1963; Paul and Gangal, 1969]. It has been suggested that tensile fractures may be generated along the edges of the indenter [Fairhurst and Lacabanne, 1956]. We find that tensile zones are formed outside the edge of the compressive zone, tipped toward the surface. Fractures may develop along the dotted lines in **Figure 48** and the rock elements in tension could be removed.

Tensile failure is a more efficient rock failure mechanism because rock tensile strength is usually much less than rock compressive strength. Hole diameter measured in single indentation tests could be easily seven times larger than indentation depth. With rock surface exposing to atmosphere, the fractured rock debris is more easily to chip off. This becomes more evident in the full-scale hammer drilling tests. The ROP in underbalanced drilling conditions, where the Bottom Hole Pressure (BHP) resulted from the weight of the drilling mud is lower than rock pore pressure, was as high as 120 ft/hr while it was only about 10 ft/hr when the BHP was raised only 500 psi (3.45 MPa) over pore pressure (**Figure 52**). Furthermore, the cuttings collected after the

tests showed that flat disk-shaped cuttings were generated instead of chunk cuttings by a tricone drillbit (**Figure 47**).

Shear Failure

When rock is in shear, its peak strength can be defined by Mohr-Coulomb criteria [Jaeger and Cook, 2007]:

$$\sigma'_1 = \frac{1 + \sin(\varphi)}{1 - \sin(\varphi)} \sigma'_3 + \frac{2 \cos(\varphi)}{1 - \sin(\varphi)} c_o \quad (2-60)$$

where σ'_1 and σ'_3 are maximum and minimum effective principal stresses, c_o is cohesive strength, and φ is the friction angle.

High impact stress also induces the abrupt movement among rock particles. When the vertical loading stress exceeds the strength defined in eq. (2-59), rock will break in shear mode. The plot of plastic shear strain is shown in **Figure 50**. Compared to the compressive deformation in **Figure 49**, where the highest compressional strain occurs right below the cutter, most shear deformation appears along the edge of the cutter, with the maximum showing at the rock surface.

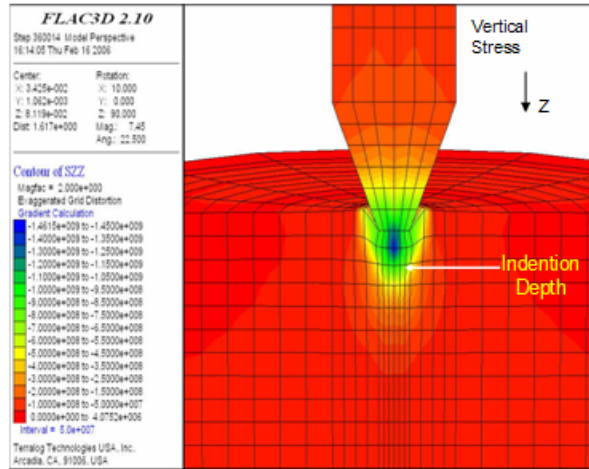


FIGURE 48: Vertical compressive stress during bit-rock impact (unit: Pa) [Han and Bruno, 2006]

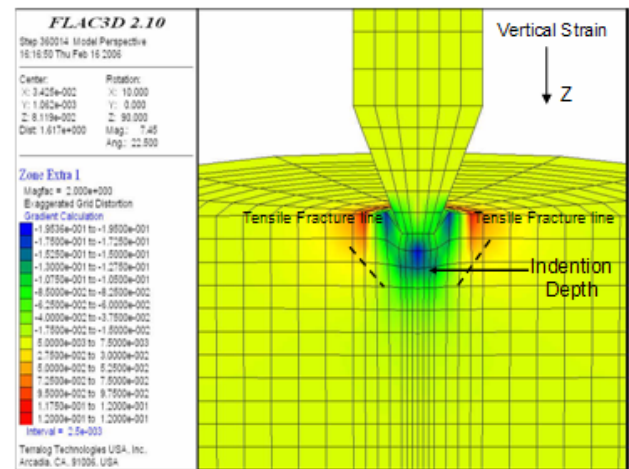


FIGURE 49: Vertical strain during bit-rock impact [Han and Bruno, 2006]

Rock Fatigue due to Repetitive Impacts

Because hammer blows can be delivered at a rate up to 1500-3000 per minutes while the longitudinal wave velocity in drill-steel is around 5200 m/s [Roberts, 1981], loading force on the rock oscillates dramatically, generated by the stress waves from both the initial blow and the reflected pulses along the drilling rod. Also stress wave could be reflected if rock is heterogeneous and there are preexisted layers and fractures. This leads to another possible important mechanism for rock failure during percussion drilling: rock fatigue due to cyclic loading.

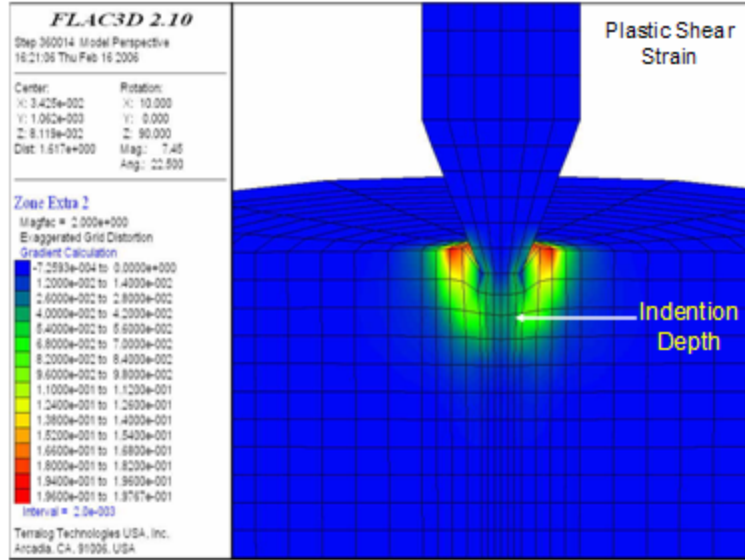


FIGURE 50: Plastic shear strain during bit-rock impact [Han and Bruno, 2006]

Haimson [1978] investigated the effects of cyclic loading on rock deformation and strength with experiments on four different hard rocks, including Tennessee marble, Indiana limestone, Berea sandstone, and Westerly granite. Four types of loadings were studied: uniaxial compression, uniaxial tension, triaxial compression, and uniaxial tension-compression. In general, it is clear that repetitive loading of any type can weaken rock strength and result in premature rock failure. For example,

- In uniaxial tension and in uniaxial compression, the strength left after 10^5 cycles cyclic loading is 60 to 80 percent of the respective Uniaxial Compressive Strength (UCS);
- Rock damage is the most severe in uniaxial tension-compression mode. The strength lost can be as high as 75% of UCS (**Figure 51**). After each cycle there is also a sharp drop in the elastic modulus as the load shifts from compression to tension.

Because the loading force in percussion drilling is essentially uniaxial compression that repetitively increases and decreases, the loaded rock is consistently, in turn, in a compression-tension state.

Acoustic emission and specimen photo-micrography suggest microfracturing as the principal mechanism of fatigue failure. If peak loading stress reaches 75% of rock maximum strength, decrease of rock strength with cycles of loading could be described as [Ewy et al., 2004]:

$$\frac{\sigma}{\sigma_i} = aN^b \quad (2-61)$$

where N is number of cycles, and σ/σ_i is the ratio of rock peak strength to initial strength. The two coefficients, a and b , are derived from lab tests. They vary with different types of rocks.

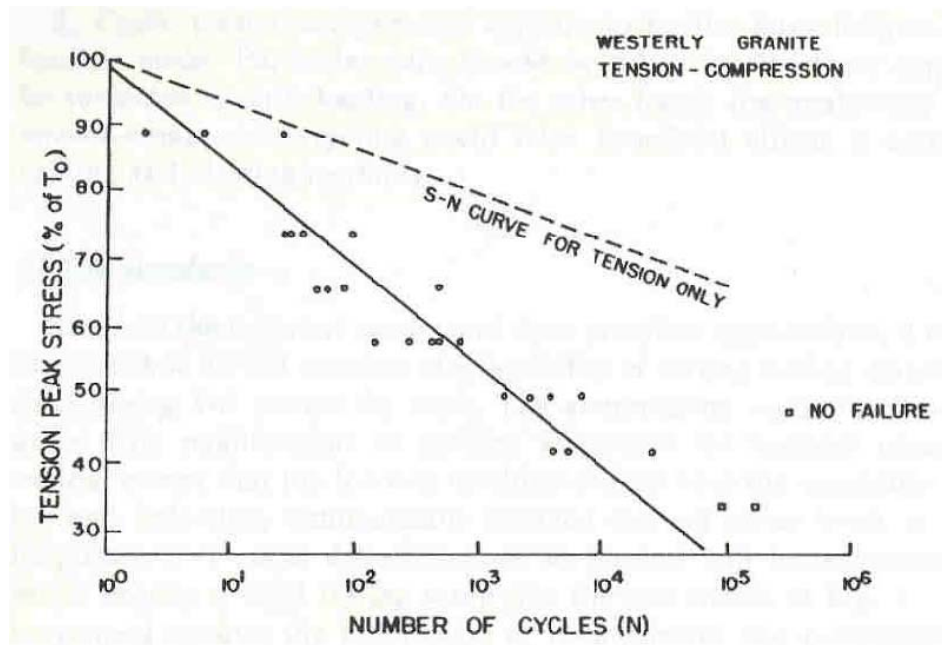


FIGURE 51: Cyclic fatigue of a granite in a uniaxial tension-compression test [after Haimson, 1978]

Effect of Pore Pressure and Bottom Hole Pressure

Due to the introduction of drilling fluids, Bottom Hole Pressure (BHP) may be different from formation fluid pressure, also known as pore pressure of rock. For a long time, lab tests and field applications have witnessed the effect of pressure difference across rock surface on drilling performance, esp. in rotary drilling [e.g. Deily and Durelli, 1958]. The pressure difference between BHP and pore pressure could be positive (over-balanced), or negative (under-balanced). Higher positive pressure difference usually leads to slower bit penetration. Some rotary drilling tests have shown ROP may decrease as much as 80% at high borehole pressures, compared with atmospheric drilling results [Cheatham, 1977]. Others have shown that increase of the absolute value of either BHP or pore pressure hardly changes bit penetration: it is the difference between BHP and pore pressure of the rock that affects bit penetration a great deal [Cunningham and Eenink, 1959; Warren and Smith, 1985]. Crater volume, however, remains constant [Maurer, 1965] or increases little [Yang and Gray, 1967] if only the horizontal stress parallel to the bottom surface is increased while the difference between BHP and pore pressure is held constant.

Similar effect has also been observed during single cutter impact test [Green et al., 2005] and hammer drilling shown in **Figure 52**.

There are several speculations on the mechanisms for ROP reduction with the pressure difference in rotary drilling, such as effective loading stress decreases as a result of increase of BHP, or higher confining stress around the rock results in higher rock compressive strength. The chip-shaped cuttings collected in full-scale hammer drilling (**Figure 53**) indicates the ROP variation is closely related to the tensile failure occurred during bit-rock impact and thereafter. Rock tensile strength is much less than its compressive strength, and therefore rock could fail more easily in tension than in compression. When there is little pressure difference between BHP and pore pressure compressing rock surface, the restraint of rock tensile failure is minimized. Rock could fail in tension not only during bit-rock impact but also when bit retreats and impact wave starts to reflect as it passes through heterogeneous rock. From this point of

view, certain type of percussion drilling is almost always better performed through encouraging rock tensile failure, such as air hammer (pressure difference is close to zero) or underbalanced drilling (pressure difference is negative).

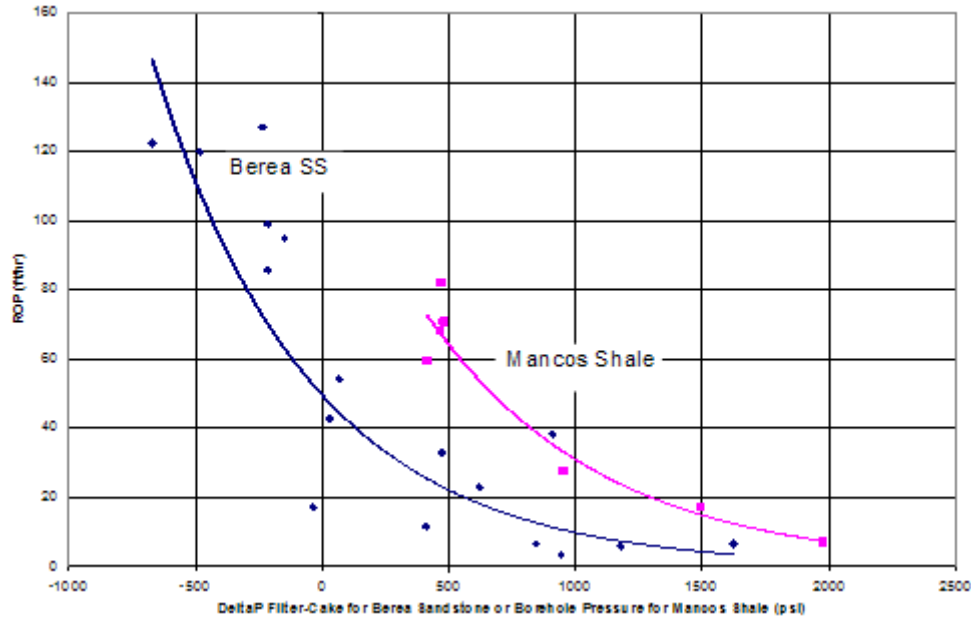


FIGURE 52: Recorded Rate of Penetration (ROP) reduction in full-scale hammer tests with various pressure difference across rock surfaces of a Berea sandstone and a Mancos shale [Han et al., 2006]

2.4.1.5 Effect of Cutter Shapes and Interactions

The effect of different cutter shapes on the penetration into brittle rock has been intensively studied. For example, Paul and Sikarskie [1965] developed a static-wedge penetration model, based on the Coulomb-Mohr failure theory. This model provides a macroscopic criterion for brittle failure when the rock is under a confined pressure below the brittle-to-ductile transition pressure. In percussive/vibratory drills, the teeth are located at the cutting edge and their characteristics and interactions are critical to the drilling rate.

To determine the effect of adjacent teeth and account for their interactions, Liu and his co-investigators [2007] developed an analytical model that extended the wedge penetration theory to express the overall specific energy as a function of the cutters spacing and teeth number. Both their theoretical models and lab tests indicate, for the coring bits with wedge-shape cutting teeth of vibratory drills, there exists an optimal spacing/depth ratio or an optimal teeth number that minimize coring bit specific energy and hence maximize its drilling rate.

2.4.2 Rotary drilling

In conventional rotary drilling, as shown in **Figure 53**, WOB first forces the drill bit cutters penetrate into the rock in the direction normal to the bit movement. Then, the cutters shear off a conchoidal chip of the penetrated rock as the bit rotates. There are two requirements for a rotary drill to advance through the rock: first WOB must be high enough to press the cutters into rock;

and second, the cutters must generate and localize enough shear stress through bit rotation to break the rock.

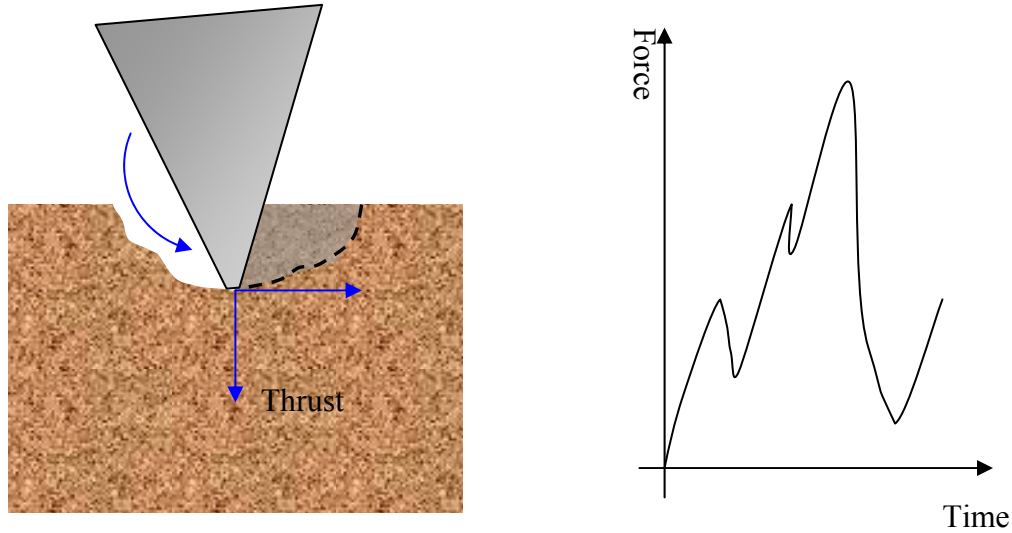


FIGURE 53: Illustration of a rotary drill (left) and a force response in bit.

2.4.2.1 Rotary Drilling with Drag Bits

This section summarizes a model of the drilling response for drag bits [Detournay and Defourny, 1992; Detournay et al., 2008], i.e., a set of relations between the weight-on-bit W , the torque-on-bit T , the rate of penetration V , and the angular velocity Ω that characterize the nature of the boundary conditions at the bit-rock interface, and some experimental validation of this model. Fixed-cutter bits or drag bits have been used in rotary drilling since about 1900 [Besson et al., 2000]. These bits initially consisted of steel blades and were reserved for the drilling of soft and shallow formations, because of their limited resistance to wear. However, the production of synthetic polycrystalline diamond compacts (PDC) as well as the development of a technology to bond the PDC to tungsten carbide in the early 1970's lead to the introduction of the modern fixed-cutters bits. The PDC bits, as they are often referred to, consist of individual PDC cutters that are mounted on a steel or tungsten carbide matrix body and are generally grouped into blades.

The PDC bit response model is restricted to the normal drilling mode, when the bit is drilling straight ahead with the bit velocity parallel to its axis of revolution and without any angular motion other than a rotation around its axis of symmetry. In contrast, bit penetration into rock for the most general mode of bit-rock interaction (relevant for directional drilling) is characterized also by a lateral and an angular component in addition to an axial component [Ho, 1987]. The model of bit-rock interaction summarized here distinguishes three successive regimes in the drilling response of PDC bits: (i) phase I, at low depth of cut per revolution, characterized by a dominance of the frictional contact process and by an increase of the contact forces with d , (ii) phase II, where the contact forces are fully mobilized, and (iii) phase III where the actual contact length increases beyond ℓ , due to poor cleaning. In contrast to models that rely on a precise description of the bit cutting structure layout [Warren and Armagost, 1988; Sinor and Warren, 1989], the effect of the bit detailed geometry is here lumped into a few parameters.

Rate Independent Interface Laws

The drilling response model for the normal mode consists of a set of relationships between W , T , V , and Ω . The kinematical variables V and Ω are conjugate to the dynamical variables W and T , respectively; i.e., P , the rate of energy dissipation at the bit-rock interface is given by

$$P = WV + T\Omega, \quad (2-62)$$

where W and T are taken positive when pointing in the same direction as V and Ω , respectively. Provided that the state variables are averaged over at least one revolution, the interface laws that relate the dynamic to the kinematical variables are generally of the form

$$W = W(V, \Omega), \quad T = T(V, \Omega), \quad (2-63)$$

meaning that the forces on the bit, W and T , depend only on the instantaneous (but suitably time-averaged) velocities, V and Ω .

While field and laboratory measurements exist [Black et al., 1986; Brett, 1992] that suggest an intrinsic dependence of the torque T on the angular velocity Ω , it has recently been argued that the observed rate dependence is in fact a consequence of the axial vibrations experienced by the drill bit during drilling, and that the apparent rate effects are actually function of the dynamical characteristics of the drilling system [Richard et al., 2007]. We will assume here that the interface laws are rate independent. The assumption is supported by experimental evidence obtained from single cutter and drilling tests conducted under kinematical control [Deliac, 1986; Richard et al., 2007; Dagrain et al., 2008]. Under the assumptions that the processes taking place at the interface between the bit and the rock are rate-independent, the drilling response can be described by relations involving only three quantities: W , T , and the ratio V/Ω , i.e.,

$$W = \tilde{W}(V/\Omega), \quad T = \tilde{T}(V/\Omega). \quad (2-64)$$

The rate-independent bit-rock interface laws will be expressed in terms of two dynamical quantities, a scaled weight w and torque t , and on the depth of cut per revolution d , which is proportional to the velocity ratio V/Ω . From now on we simply refer to weight-on-bit and torque-on-bit as weight and torque. These three basic state variables are defined as

$$w = \frac{W}{a}, \quad t = \frac{2T}{a^2}, \quad d = \frac{2\pi V}{\Omega}$$

where a is the bit radius. Scaling of the weight and torque removes the influence of the bit dimension from the interface laws. The scaled quantities w and t , which have dimensions Force/Length (a convenient unit is the N/mm), can conveniently be interpreted as the normal and shear force per unit length on a two-dimensional cutter removing material over a depth of cut d , see **Figure 54**.

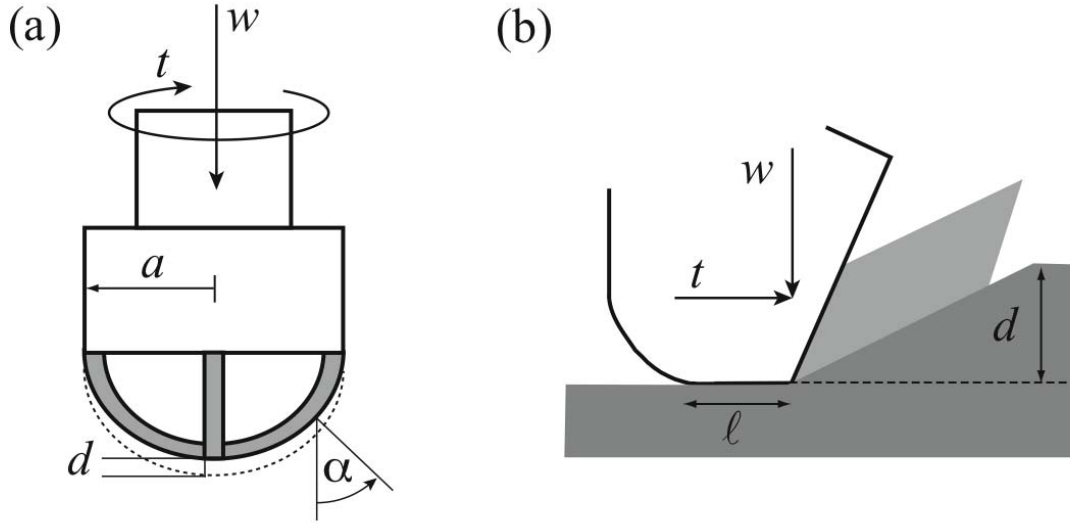


FIGURE 54: (a) Sketch of a drag bit showing the weight-on-bit w , torque-on-bit t , and depth of cut per revolution d ; (b) sketch of the equivalent two-dimensional cutter showing the tangential force t , the normal force w , and the depth of cut d [Detournay et al., 2008].

Cutting and Frictional Contact Processes

It is further postulated that two independent processes, cutting and frictional contact, characterize the bit-rock interaction. The torque t and weight w can thus be decomposed as

$$t = t_c + t_f, \quad w = w_c + w_f, \quad (2-65)$$

where the subscript “ c ” denotes the cutting components of w and t , and “ f ” the contact components. **Figure 55** illustrates the decomposition of the total forces (t , w) into forces transmitted by the cutting face (t_c , w_c) and by the wear flat (t_f , w_f), using the conceptual representation of an equivalent cutter.

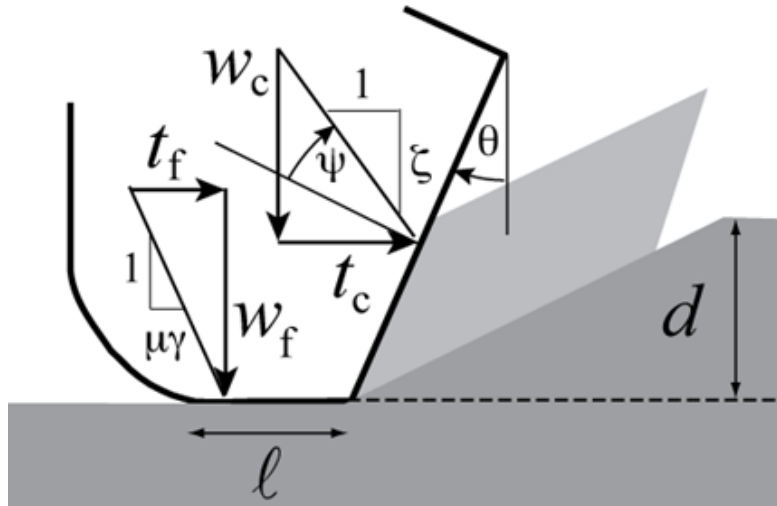


FIGURE 55: Decomposition of the total forces (t , w) into forces transmitted by the cutting face (t_c , w_c) and by the wear flat (t_f , w_f) [Detournay et al., 2008].

Cutting Process

The cutting components t_c and w_c are related to the depth of cut d according to (**Figure 56**)

$$t_c = \varepsilon d, \quad w_c = \zeta \varepsilon d. \quad (2-66)$$

where ε is the intrinsic specific energy, a quantity with dimension of stress and ζ is a number, which is typically in the range $[0.5 - 0.8]$. These two constants characterize the cutting process. The adjective “intrinsic” is introduced to differentiate ε from the specific energy E , defined below, which depends not only on the wear state of the bit, but also on the depth of cut. The intrinsic specific energy represents the energy required to remove a unit volume of rock by an ideally sharp bit under given field conditions [Detournay and Defourny, 1992]. In fact, ε depends not only on the rock strength [Dagrain et al., 2008] and on the bottom-hole pressure and local pore pressure [Detournay and Atkinson, 2000], but also on the back-rake angle θ of the cutters. However, single cutter experiments [Richard, 1999] indicate that the dependence of the intrinsic specific energy ε on θ is very weak over the range $[10^\circ - 20^\circ]$, which typifies the back-rake angle of most cutters mounted on drag bits. Hence for all practical purposes, ε depends only on the rock and on the pressure environment and not on the bit type and its wear state; this justifies the use of the term “intrinsic.” Although it is possible to write $\zeta = \tan(\theta + \psi)$, with ψ denoting the angle between the normal to the cutter face and the cutting force, it should be noted that ψ cannot be interpreted as a friction angle independent of θ . Indeed, single cutter experiments [Richard, 1999; Dagrain et al., 2008] and numerical simulations [Huang et al., 1999; Detournay and Dreshcher, 1992; Huang and Detournay, 2008] have indicated the existence of a complex flow process in front of the cutter, which is reflected by a dependence of the angle ψ on θ .

Frictional Contact Process

Our understanding of the frictional contact process is not complete at the time of this writing. However, it is possible to describe with reasonable confidence the dependence of both the contact components of the torque and weight on the depth of cut d . Three phases appear to exist with increasing d , corresponding respectively to an increase of the contact forces, a saturation, and finally another increase of the contact forces associated to poor cleaning (see **Figure 56**, which illustrates the assumed evolution of w_f with increasing depth of cut d).

First, we introduce the bit characteristic contact length ℓ which is defined as the ratio $\ell = A_f/a$, where A_f denotes the combined area of the projection of the cutter wear flat surfaces onto a plane orthogonal to the axis of revolution of the bit. This contact length ℓ is an objective measure of the bit bluntness. Experimental evidence suggests that new or sharp bits are typically characterized by a value of ℓ less than 1 mm. In blunt bits, ℓ can increase beyond 10 mm. There is also a limiting value to the normal stress that can be transmitted by the wear flat. This limiting value will be denoted as σ and will be referred to as the contact strength. The contact strength reflects the existence of a contained plastic flow process underneath the cutter wear flat, and thus will generally depend on the elastic modulus and strength parameters of the rock. Depending on rock and the pressure environment, σ can vary from a few MPa to several hundred MPa.

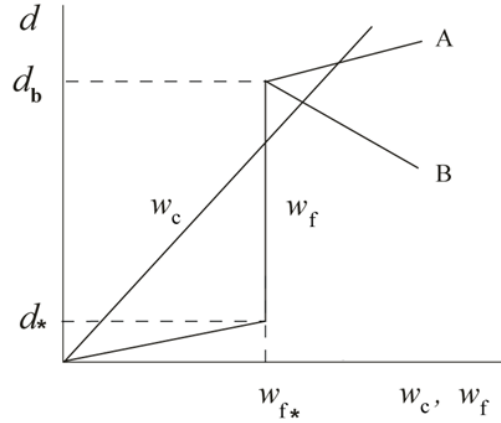


FIGURE 56: Conceptual response of the bit in the w_c - d and w_f - d spaces [Detournay et al., 2008]

In Phase I drilling regime ($w_f < w_{f*}$), the contact component of the weight, w_f , increases linearly with the depth of cut d

$$w_f = \sigma \kappa d. \quad (2-67)$$

It is conjectured that the increase of the contact force is predominantly due to a geometrical effect, as the two contacting surfaces are generally not conforming. Change in the depth of cut d indeed affects the angle between the two contacting surfaces thus causing a variation of the actual contact area (the inclination of the rock surface in the tangential direction is parallel to the cutter velocity whose vertical component is proportional to d). If the increase of w_f with d is entirely due to a geometrical effect, then κ represents the rate of change of the contact length with d . Single cutter experiments indicate that κ is a number typically in the range [1-10] [Detournay and Defourny, 1992; Nishimatsu, 1993; Detournay and Richard, 2008].

In Phase II ($w_f = w_{f*}$), the contact forces are fully mobilized. Beyond a critical value of the depth of cut per revolution d_* (function of the bit bluntness ℓ), the contact forces do not increase anymore because the normal contact stress has reached a maximum value σ , and the actual contact length has attained a limiting value that characterizes the bit bluntness. This drilling regime is thus defined by $w_f = w_{f*} = \ell \sigma$, with the consequence that any increase of the weight w must necessarily be translated as an increase of the cutting component w_c . In phase II, the bit behaves incrementally as a sharp bit.

Finally in Phase III, the contact surface increases, through pile-up of sheared rock material between the bit and the rock, caused by poor cleaning (the production of cutting exceeds what can be removed by the flow of mud). Because of this increase of the contact area, w_f becomes larger than w_{f*} . The threshold for phase III is here taken to correspond to a critical value of the depth of cut per revolution, d_b , which can however be a function of the bit geometry, mud flow rate, mud properties, and properties of the rock being drilled. Furthermore, the variation of w_f with d in Phase III depends on a variety of factors, which precludes the existence of a contact law in this phase.

The contact components of torque and weight are assumed to be always constrained by a frictional relation

$$t_f = \mu \gamma w_f, \quad (2-68)$$

where μ is the coefficient of friction at the wear flat/rock interface and γ a “bit constant,” which encapsulates the influence of the orientation and distribution of the contact forces acting on the bit. The coefficient of friction μ was conjectured earlier [Detournay and Defourny, 1992] to reflect the internal friction angle of the rock φ , i.e.

$$\mu = \tan \varphi. \quad (2-69)$$

Extensive single cutter experiments on different rocks [Almenara and Detournay, 1992; Lhomme, 1999; Dagrain, 2006] have indeed confirmed that the friction angle at the wear flat/rock interface, assessed from the slope of the friction line in the $E-S$ diagram (discussed below), is remarkably close to the internal friction angle, estimated from triaxial experiments at confining stress level comparable to the unconfined compressive strength. Similarity between these two friction angles is due to the existence of a boundary layer of failed rock below the cutter wear flat, where the shear flow takes place [Detournay and Defourny, 1992; Lhomme, 1999; Dagrain, 2006].

The bit constant γ depends on the orientation and distribution of the contact forces acting on the bit, both of which are strongly influenced by the bit design. A simple estimate of γ can be obtained for conditions that have been identified above as phase II drilling. This is indeed a situation where the contact length has reached its characteristic value ℓ and the normal contact stress has attained its limiting value σ , and thus $w_f = w_{f*} = \ell \sigma$.

The scaled torque transmitted through the contact surfaces, t_f , is sensitive to both the orientation of the contact surfaces, and to the manner in which the contact length ℓ is distributed radially across the bit (it is assumed that the stress vector transmitted at the rock/wear flat interface is contained in the plane defined by the normal to the contact and the cutter velocity vector). To calculate t_f , we introduce the radial contact length density λ , a function of the radial distance r from the bit axis. Hence, we can express $d\ell(r)$, the contact length associated with (parts of) the cutters inside the ring located between distance r and $r + dr$ from the bit axis, as $\lambda(r)dr$, and thus

$$\ell = \int_0^a \lambda(r)dr. \quad (2-70)$$

The contact component of the torque is then given by

$$t_f = 2\mu\sigma \int_0^a \frac{\lambda(r)rdr}{\cos \alpha(r)}, \quad (2-71)$$

where α is the angle between the normal to the contact surface and the bit axis. On the majority of bits, the cutting edge is curved, and thus α is a function of the distance between the cutter and the bit axis, see **Figure 53**. In view of (2-68) with $w_f = \ell \sigma$, and (2-71), the expression for the bit constant γ becomes

$$\gamma = \frac{2}{\ell} \int_0^1 \frac{\lambda(r)rdr}{\cos \alpha(r)}. \quad (2-72)$$

The above expression for γ has been confirmed experimentally with simple fishtail bits [Detournay et al., 2008].

2.4.2.2 Linear constraint on the drilling response

Relationship between Weight, Torque, and Depth of Cut

Combining (2-65), (2-66), (2-67) and (2-68) leads to a linear relation between w , t , and d

$$t = \mu\gamma w + E_o d, \quad (2-73)$$

where

$$E_o = (1 - \beta)\varepsilon, \quad \beta = \mu\gamma\zeta \quad (2-74)$$

Equation (2-73) represents a linear constraint on the response of PDC bits in terms of the three basic variables w , t , d ; it must be met irrespective of the state of wear of the bit and the magnitude of the contact forces. The geometric representation of (2-73) is the plane Π in the space (w, t, d) as shown in **Figure 57**, which further illustrates the response of a sharp and blunt bit. A geometrical interpretation of the parameters ε , E_o , ζ , and $\mu\gamma$ can also be found in **Figure 57**.

The parameter E_o takes a particular meaning when considering the response of a bit under constant weight. According to (2-73), such a response must lie on the line of slope E_o and ordinate intercept $\mu\gamma w$ in a plot of the scaled torque t versus the depth of cut d , see **Figure 61** for the case $\beta < 1$. Also represented in this Figure is the cutting line going through the origin and inclined on the d -axis with a slope ε ; the cutting line reflects the response of a perfectly sharp bit for which torque and depth of cut per revolution are both proportional to the weight-on-bit. Introduction of the cutting line enables the decomposition of the torque into a cutting and frictional component, and consequently a natural definition of the drilling efficiency η as

$$\eta = \frac{t_c}{t}$$

It is obvious that moving left to right on the constant weight-on-bit line is associated with an increasing efficiency: $\eta = 0$ on the torque axis where all the torque is dissipated in frictional processes and $\eta = 1$ on the cutting line (in this diagram, a constant efficiency is represented by a line through the origin). We finally remark that, under the constant weight-on-bit constraint, lower efficiency implies decrease of the torque if $\beta < 1$ and the opposite if $\beta > 1$.

E-S Diagram

The linear constraint (2-73) can equivalently be written as

$$E = E_o + \mu\gamma S, \quad E \geq \varepsilon \quad (2-75)$$

where E is the specific energy and S the drilling strength, respectively defined as

$$E = t/d, \quad S = w/d. \quad (2-76)$$

Both E and S have dimension of stress; a convenient unit is the MPa (numerically equivalent to J/cm^3).

Equation (2-75) is represented by the friction line of slope $\mu\gamma$ in the E - S diagram (see **Figure 58 and 59**). In this representation, E_o is simply the intercept of the friction line with the E -axis. The cutting point, characterized by $E = \varepsilon$ and $S = \zeta\varepsilon$, corresponds to an ideally

efficient drilling process, where all the energy provided to the bit is transferred into the cutting process. The cutting point is at the intersection of the friction line with the cutting locus, the line passing through the origin of the plane and inclined by ζ^{-1} to the S -axis. Admissible states of the drilling response of a PDC bit in the E - S diagram are represented by all the points on the friction line, which lies to the right of (and above) the cutting point.

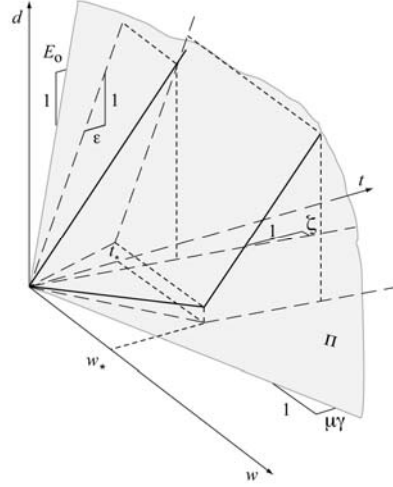


FIGURE 57: Three-dimensional representation of the PDC bit model in the $\{t, w, d\}$ space for a sharp and blunt bit (with phases I and II). The plane Π represents a constraint on the bit response [Detournay et al., 2008]

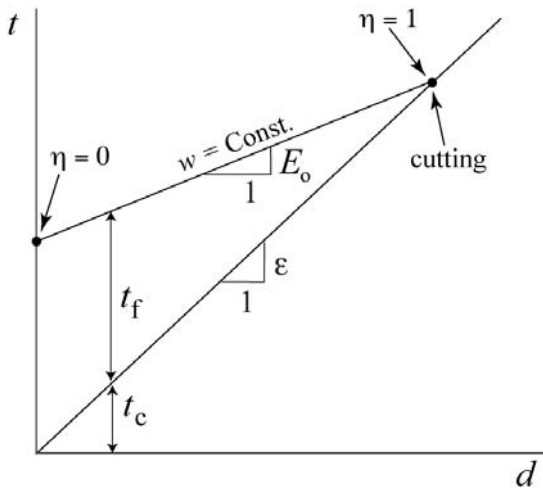


FIGURE 58: Constant weight w . Plot of torque t versus depth of cut per revolution d ($\beta < 1$) [Detournay and Defourny, 1992].

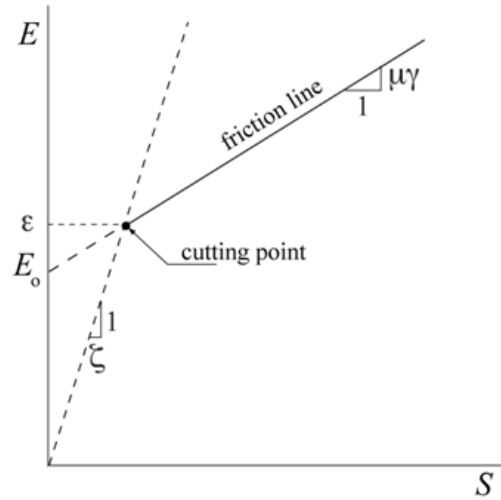


FIGURE 59: Schematic E - S diagram [Detournay and Defourny, 1992].

Consider a horizontal line going through the cutting point. The vertical distance between that line and a point on the friction line represents the component of the specific energy which is dissipated in frictional processes. The drilling efficiency η can thus alternatively be defined as

ε/E . It is also convenient to introduce the quantity χ , defined as the ratio of the specific energy to the drilling strength, i.e. $\chi = E/S$. A simple relation exists between χ and the efficiency η :

$$\eta = \frac{\chi - \mu\gamma}{(1 - \beta)\chi} \quad (2-77)$$

The parameter χ varies between ζ^{-1} and $\mu\gamma$ as the efficiency η decreases from 1 to 0.

Note finally that an increase of the mud pressure p_b (all other conditions remaining the same) will cause the cutting point to move up the cutting locus displacing with it the friction line, as the intrinsic specific energy ε is the only parameter that depends significantly on p_b .

Experimental Evidence of the Existence of a Linear Constraint

Published results of a series of full-scale laboratory drilling experiments, carried out in a Mancos shale with a step-type 8.5 inches diameter PDC bit for various combinations of imposed Ω and W ($W = 40, 80, 120$ kN and Ω varying between 50 and 900 RPM) [Black et al., 1986] can readily be analyzed within the above framework. (Results of tests performed at $W = 20$ kN are also reported in [Black et al., 1986], but are not included in this discussion for reasons discussed in [Detournay and Defourny, 1992].)

The overall response of the laboratory tests is summarized in the $E-S$ diagram shown in **Figure 60**. The points are coded in terms of the weight-on-bit W . A linear regression on the reduced data set gives the following estimates: $E_o = 150$ MPa and $\mu\gamma = 0.48$. Assuming that the bit constant $\gamma = 1$, the friction angle is approximately 26° (i.e. $\mu = \tan \varphi$). This value should be considered as an upper bound of the internal friction angle of the Mancos shale (published values of φ , deduced from conventional triaxial tests, are in the range $20^\circ - 22^\circ$). The intercept of the friction line with the E -axis, E_o , represents a lower bound of the intrinsic specific energy ε ; an upper bound of ε being given by the ordinate of the “lower-left” (LL) point of the data cluster. The LL point is here characterized by $E = 230$ MPa and $S = 160$ MPa, and thus by a ratio $\chi = 1.44$. This point is likely to be close to the optimal cutting point on the ground that (i) the bit is new, and (ii) the value of χ is quite high. Thus here the cutting parameters are estimated to be: $\varepsilon = 230$ MPa and $\zeta = 0.69$.

It can be observed from the coding of the points on the $E-S$ plot that the drilling efficiency increases with the weight-on-bit in these series of tests. The original data also indicates that the efficiency drops with increasing rotational speed of the bit. Clearly, all the experimental data lay along the same line regardless of the angular velocity. Therefore, neither the intrinsic specific energy ε nor the apparent friction coefficient $\mu\gamma$ between the bit and the rock varies with the angular velocity. However, the dispersion along the friction line is large; the points representative of the bit response move upwards along the friction line with increasing angular velocity, under constant weight-on-bit. Furthermore, as can be seen in **Figure 61**, the mean torque decreases with increasing Ω under constant W , consistent with a value of $\beta < 1$ ($\beta = 0.35$), but in apparent contradiction with the assumption of rate independence of the interface laws.

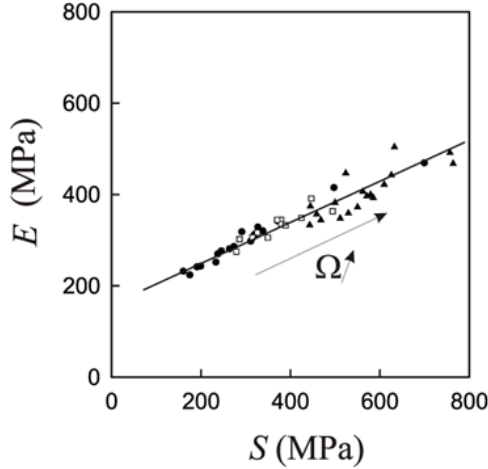


FIGURE 60: E - S diagram, according to published experimental data [Black et al., 1986] with \blacktriangle $W = 40$ kN, \square $W = 80$ kN, \bullet $W = 120$ kN [9]

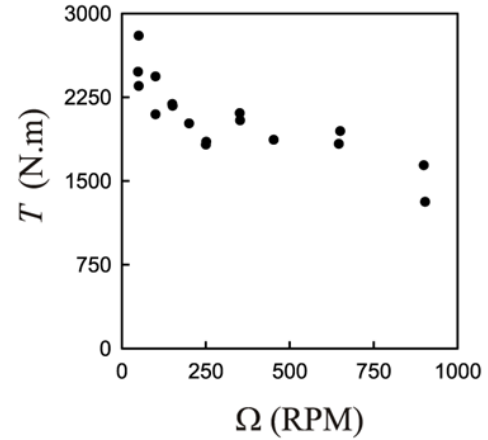


FIGURE 61: Evolution of the mean torque $\langle T \rangle$ with the angular velocity Ω_o under constant weight-on-bit ($W = 120$ kN), according to published experimental data [Black et al., 1986; Richard et al., 2007]

The diminishing efficiency η with larger Ω under constant W reflects an increase of the contact forces at the expense of the forces mobilized by the cutting process. Assuming permanent contact between the bit flat and the rock, σ would have to increase with the relative velocity between the wearflat and the rock. Although such a law cannot be ruled out *a priori*, no significant effect of the cutting velocity on the forces has been reported in the literature. However, the mean contact stress could increase with Ω if axial vibrations responsible for an intermittent loss of contact between the bit and the rock progressively decrease in intensity with Ω . Such a result is actually predicted by the model of drilling induced self-excitations proposed by [Richard et al., 2007]. These experimental results point therefore to the need of performing drilling experiments, aimed at characterizing the bit-rock interface laws, under kinematical control (i.e. both rate of turn and rate of penetration imposed) so as to prevent the development of self-excited vibrations.

2.4.2.3 Complete Drilling Response

Model

The response equations for drilling in Phase I and II are readily developed from the earlier expressions for the cutting and contact components of the torque and weight. They are interpreted geometrically in **Figures 62 to 65**, which show the response of the bit in the spaces d - w , d - t , and t - w .

For phase I drilling, we obtain after combining (2-65), (2-66), (2-67), and (2-68) the following expressions for w and t

$$w = S_* d, \quad t = \mu \gamma' w, \quad (2-78)$$

where

$$S_* = \zeta \varepsilon + \kappa \sigma, \quad E_* = \varepsilon + \mu \gamma \sigma \kappa, \quad \gamma' = \frac{\gamma}{1 - E_o/E_*} \quad (2-79)$$

If $|E_o/E_*| \ll 1$ as generally expected, we have that $\gamma' \sim \gamma$ and thus

$$t \sim \mu \gamma w. \quad (2-80)$$

The relationship between torque and weight on bit in phase I is therefore approximately the same as the constraint (2-68) between t_f and w_f . In other words, the response of the bit in phase I is dominated by the frictional contact process.

For phase II drilling, the incremental response of the bit is similar to the one of a sharp bit, i.e., any change of weight w and of torque t is assumed by the cutting component w_c and t_c , respectively. Hence, the response in phase II can be written as

$$t - t_* = \varepsilon(d - d_*), \quad w - w_* = \zeta \varepsilon(d - d_*) \quad (2-81)$$

where

$$d_* = \ell/\kappa, \quad \frac{w_*}{w_{f*}} = \frac{E_* - E_o}{E_* - \varepsilon}, \quad \frac{t_*}{t_{f*}} = \frac{E_*}{E_* - \varepsilon}.$$

Note finally that the cutting and contact components of the torque and the weight on bit can readily be calculated from w and t , if ζ and $\mu\gamma$ are known, according to (see **Figure 65**)

$$t_c = \frac{t - \mu \gamma w}{1 - \beta}, \quad w_c = \zeta t_c, \quad (2-82)$$

$$w_f = \frac{w - \zeta t}{1 - \beta}, \quad t_f = \mu \gamma w_f, \quad (2-83)$$

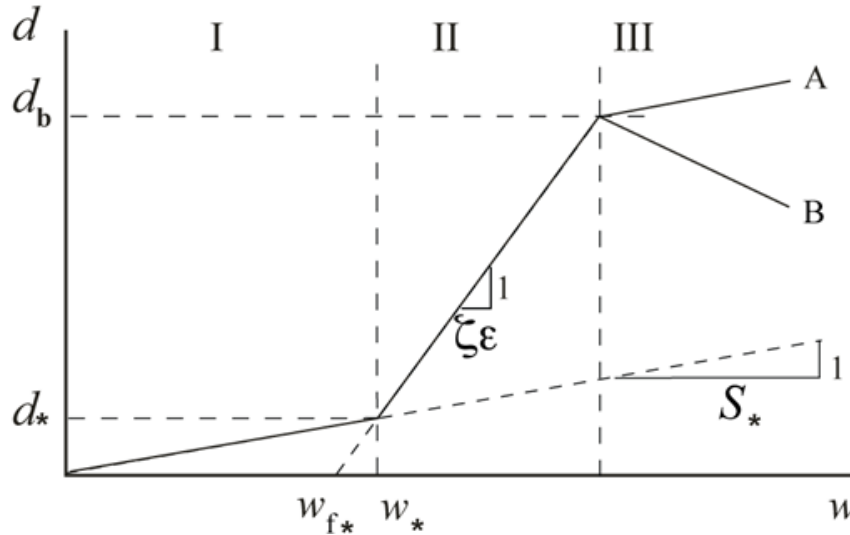


FIGURE 62: Conceptual response of the bit in the w - d space [Detournay et al., 2008].

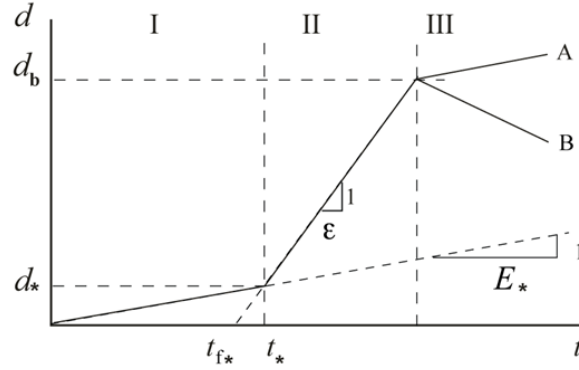


FIGURE 63: Conceptual response of the bit in the t - d space [Detournay et al., 2008]

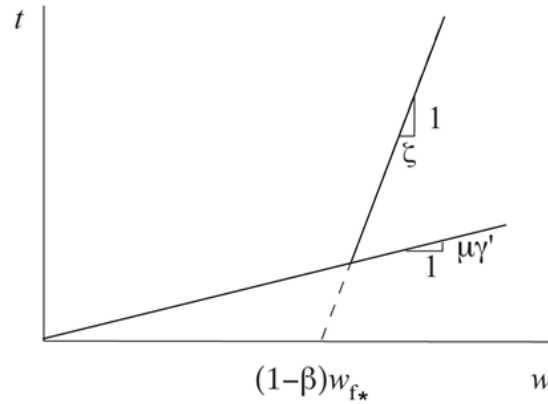


FIGURE 64: Conceptual response of the bit in the t - w space [Detournay et al., 2008]

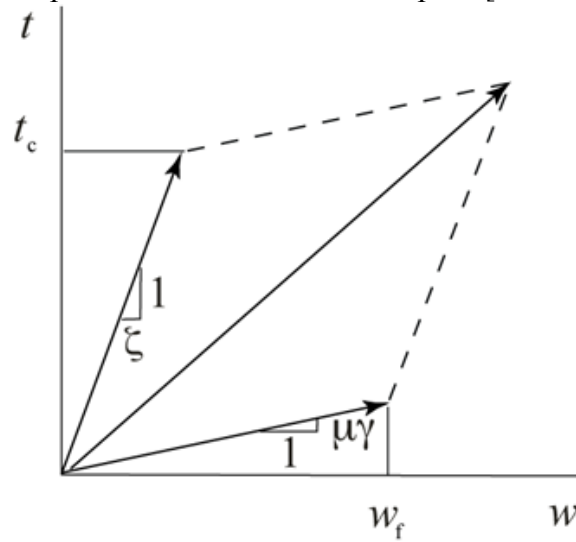


FIGURE 65: Decomposition of the bit response into cutting and contact components in the w - t diagram [Detournay et al., 2008]

Experimental Validation

A drilling experiment carried out at Schlumberger Cambridge Research with a small drilling rig (SDM) provides support to the drilling response model summarized above. Drilling tests in the SDM, which accommodates cylindrical rock samples that are about 200 mm in length and 150 mm in diameter and drill bits that have diameters up to 60mm, are performed under controlled

confining pressure, mud pressure, and pore pressure (prior to drilling), and under either imposed weight-on-bit or imposed rate of penetration (see Detournay et al., [2008]) for a presentation of drilling experiments performed under kinematical control).

The drilling experiment was conducted on a sample of Stancliffe sandstone under balanced condition using a core barrel. The Stancliffe sandstone is a fine-grained rock from the Carboniferous Namurian, with unconfined compressive strength $q = 85$ MPa, permeability $k = 2$ mD, and porosity $\phi = 13\%$. The core barrel has outer radius $a = 25.4$ mm and inner radius $b = 16.0$ mm; it is equipped with five rectangular PDC cutters with a backrake angle of 15° (angle taken positive for forward inclination of the cutting face). The nominal contact length ℓ is about 3 mm. The rock sample was saturated prior to drilling with the mud pressure and pore pressure maintained at approximately 3 MPa. The weight-on-bit was progressively manually increased until the apparition of phase 3 regime. The angular velocity Ω was set to $2\pi \text{ s}^{-1}$ (60 RPM).

The results are illustrated in the $d-w$, $d-t$, $t-w$, $E-S$ diagram shown in **Figure 66 and 67**. Grey filled points are used to distinguish a transition regime between phase I and II. Estimation of the model parameters for the “drill-on” experiment yields the following values: $\varepsilon = 77$ MPa, $\zeta = 0.64$, $\mu\gamma = 0.70$ (corresponding to a friction angle $\varphi = 35^\circ$ at the wearflat/rock interface, on account that $\gamma = 1$), $\sigma = 40$ MPa. The inferred value of intrinsic specific energy ($\varepsilon = 77$ MPa) is close to the measured unconfined compressive strength ($UCS = 85$ MPa) of the Stancliffe sandstone, thus confirming the correlation between ε and UCS obtained in scratch tests conducted at atmospheric pressure [Dagrain et al., 2008]. (Since the mud pressure and pore pressure are balanced, the forces on the bit are expected to be similar to those that would be observed in a similar drilling experiment at atmospheric pressure.)

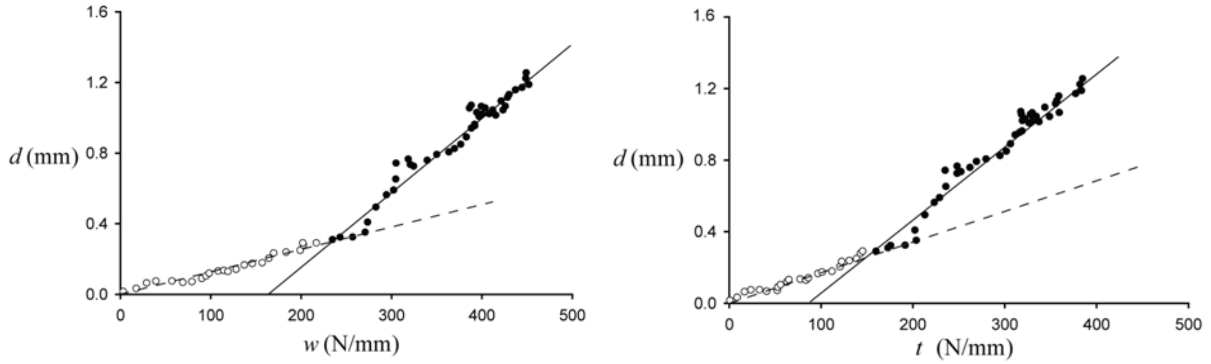


FIGURE 66: $w-d$ and $t-d$ diagrams for drill-on test conducted in Stancliffe Sandstone. White and black symbols identify phase I and phase II drilling regimes, respectively.

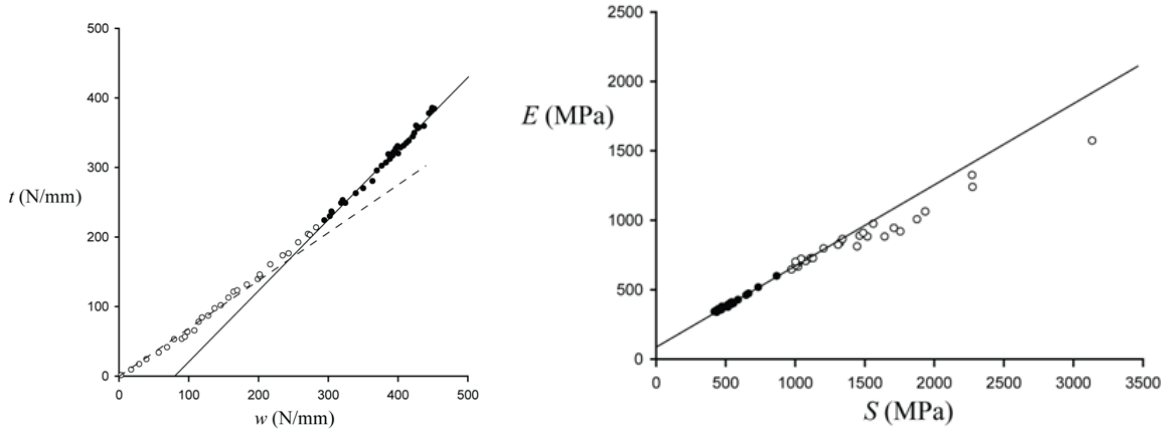


FIGURE 67: $t - w$ and $E - S$ diagrams for drill-on test conducted in Stancliffe Sandstone. White and black symbols identify phase I and phase II drilling regimes, respectively.

2.4.3 Percussive-Rotary

The major disadvantage of rotary drills is the occurrence of excessive bit wear at high rate of rotation, high values of thrust, and/or in hard rock; the major demerit of percussive drills is its relatively low penetration rate in soft rock, and discontinuities in the process of cutting (**Figure 68**). The combination of both drills (rotary-percussive drill) results in a fast ROP at a low level of thrust [Roberts, 1981].

Because rock is damaged by repetitive impacts, bit penetration and rotation become much easier than in solely percussive drilling. Therefore larger amount of chips may be sheared off the rock. On the other hand, debris removal becomes more efficient because of bit rotation, which results in a fresh rock surface consistently.

However, combination of percussive thrust and rotation involves so many complicated processes that few experiment has been done so far to investigate the physics.

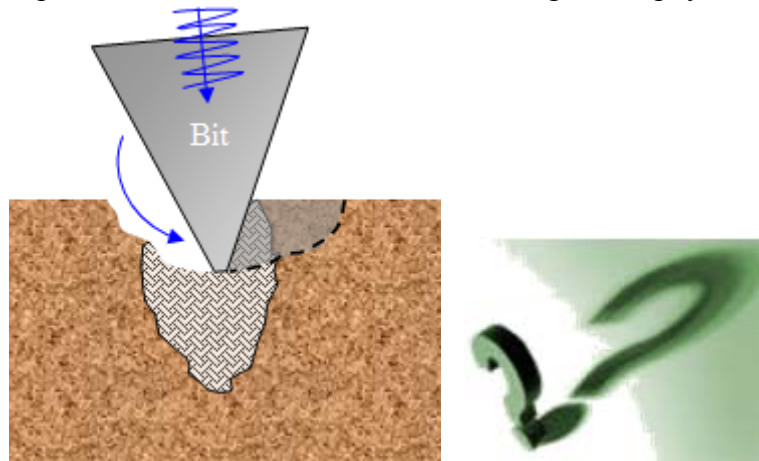


FIGURE 68: Illustration of a percussive-rotary drill

2.4.4 Other drilling methods

Besides mechanical drills such as rotary and percussive, there are other drilling methods. Based on energy type utilized in rock remove, some examples are as follows.

- Thermal drills such as laser drill, nuclear drill, electricity melting drill, microwave drill, magnetic drill, plasma drill, etc. Lab tests demonstrate that modern lasers have more than enough power to spall, melt and vaporize rock [Parker et al., 2003]. It also showed that the type of rock tested did not significantly change the amount of energy needed to cut or melt it.
- Nuclear reactors can produce temperature high enough to fuse and vaporize the rock. Adams [1965] patented a needle-shaped nuclear penetrator for drilling into the earth's crust. It melts the rock beneath it and will melt back to the surface after it reaches a predetermined depth. It has not been under development since 1960s, because of its size limitations on the reactors, high cost and safety problems.
- Using fluorine and other reactive chemicals, chemical drilling has been successfully tested to drill sandstone, limestone, and granite in the laboratory [McGhee, 1955]. However, it needs to deal with large volumes of highly reactive chemicals and damages environment to such extent that any logging or sampling process becomes meaningless.
- Explosive drills were used mainly in the Soviet Union [Ostrovskii, 1960]. With mixing two non-explosive liquids, a chemical is used to initiate the explosion, which demolishes rock.

While different drilling methods involve different rock breakage mechanisms, it should be fair to say there is still a long way to go before most of non-mechanical drills mentioned above can be applied in field.

2.4.5 Drilling Efficiency

2.4.5.1 Index for Drilling Efficiency

Different indexes have been developed in various drilling industries to evaluate the efficiency of drilling. Some examples are:

Specific energy is defined as the energy required to remove a unit volume or mass of rock. It is not only related to intrinsic properties of rock but also to bit type and design. Efficiency of fragmentation could be achieved through a combination of optimum bit inserts spacing and steady state cutting, which continuously removes layers cracks and weakens successive layers. [Demou et al., 1983]. For example, specific energy is found to decrease rapidly with increasing inserted depth at first, but then level off to a relatively constant value (**Figure 69**). An estimate obtained in oil shale is that specific energy for steady-state drag bit fragmentation is about 30% of that required for independent fragmentation [Larson and Olson, 1977].

Resistance is a function of the rock toughness and of the degree of thrust exerted. It can be seen that the amount of the transmitted energy depends on these factors rather than the available energy. In very soft or very tough rock, or if the drill is operated free or with insufficient thrust, residual energy will remain in the rod and drill to build up to potential failure levels. Only a proportion of the impact energy is available for rock breakage.

Rock drillability is used as a comprehensive index, often in mining and quarrying industries, that was initially based on the hardness and toughness of rocks, rock strength, later related to specific gravity, penetration rate, drill bit wear, properties of drill cuttings.

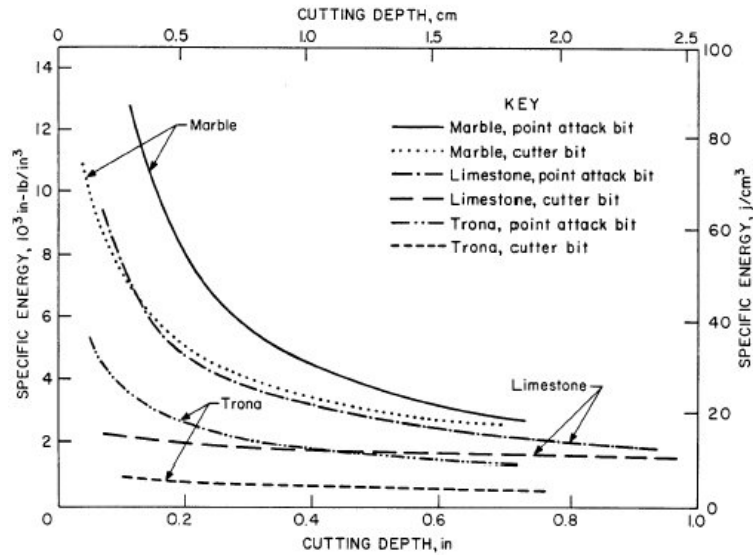


FIGURE 69: Specific energy vs. cutting depth [after Demou et al., 1983]

IF factor, which is the product of impact force (I) and the frequency of blows per minute (F), was used to evaluate the performance of the percussion drilling tool [Topanelian, 1957].

Rate of Penetration (ROP) are more often focused in oil industry as a faster ROP with acceptable economic cost usually means lower cost per foot and faster capital recovery. Reducing cost per foot generally requires achieving a higher average rate of penetration and/or increasing the useful drilling time between trips.

2.4.5.2 Static and Dynamic Variables to Improve Drilling Efficiency

All possibilities that may improve or withhold ROP may be classified into two categories: static and dynamic. The static group refers to the parameters that hardly change with time once equipment is installed in place, such as bit hardness and strength, rock strength, abrasiveness, and hardness etc. Dynamic parameters are manageable and may change with time of drilling such as hammer energy, bit abrasion, bottom hole pressure (BHP), thrust force, weight on bit (WOB), rotation speed (RPM), drilling fluid, etc.

Static Variables

Selection of bit materials is a very important issue. In soft sediments, drilling bits tipped with tungsten carbide can sometimes be used. In harder rocks, diamond bits are essential. Diamond or adamant is a crystalline, compact or drypto-crystalline form of pure carbon, and is the hardest substance known so far. It occurs as octahedral crystals with a perfect cleavage parallel to the faces of the octahedron. Alluvial diamonds may be rounded due to attrition, and the faces of diamond crystals are often curved. However, diamond is brittle; therefore very sharp edges wear away rapidly due to fracture and graphitisation caused by localized overheating [McGregor, 1967]. For this reason excessive thrust should not be used on a new diamond bit.

Carbide is the single greatest variable for downhole bits. The percentage of cobalt in the carbide grade is an important consideration: it is determined by fracture toughness and wear

resistance. Different shapes of carbides have been tried [Leonard, 2001]: spherical carbide, also known as hemispherical carbide, is best suited for hard to medium rock formations; parabolic, also referred to as semiballistic or ogive carbide, is used in medium formation; the ballistic carbide's curved bullet shape offers rapid cutting speed and is used mostly in softer formations. This type of carbide is prone to shear failure in harder formation.

Tests on different bit types, including point attack bits and cutter bits indicate that, comparing to point attack bits, cutter bits are more efficient in rock fragmentation, showing lower cutting and normal forces, and less bit deterioration [Demou et al., 1983]. Also it has been found that optimum cutters spacing of the drag bit is generally equal to or greater than the average crater width at a given depth. For example, for a cutting depth of 0.5 in, the crater width of 2.4 inch will be equal to or less than the optimum spacing.

Hardness is a measurement of the resistance of a mineral to scratching (not breakage). The wear between moving surfaces in frictional contact depends largely upon their hardness [Rabinowicz, 1965]: if one surface is significantly harder than the other, the hard surface should wear very little. Different terms have been used for quantifying hardness, such as

- Shore hardness or scleroscope hardness is measured in terms of the elasticity of the material. A diamond-tipped hammer in a graduated glass tube is allowed to fall from a known height on the specimen to be tested, and the hardness number depends on the height to which the hammer rebounds;
- Mohs' scale, used to assign values to the hardness of different minerals from 1, the softest, to 10, the hardest, is based on the scratch test and make sure of common minerals as standards. Mohs's scale, however, becomes so compressed that it does not provide adequate distinction between hard substances. Accordingly Ridgeway et al. [1933] extended the upper portion of the scale so that it ranges from 7 through 15.
- Hardness is often related to rock strength. That is to say, hard rock is usually strong. For three different tested materials in Demou's experiment [1983], including Indiana limestone, Tennessee marble, and Valders white rock, unconfined compressive strengths are 10,000, 16,800, and 29,600 psi respectively, and the Shore hardness is 32, 55, and 68 scleroscope units respectively. Compared to a baseline rock with 7,200psi UCS and 23 Shore hardness, a simple relation between rock unconfined compressive strength and Shore hardness has been noticed:

$$\frac{10,000}{7,200} \approx \frac{32}{23} ; \quad \frac{16,800}{7,200} \approx \frac{55}{23}$$

Dynamic Parameters

In percussion drilling, energy and frequency of hammer blows rely heavily on the pressure of the working fluid and the access of flow to the workings of the tool. Physical parameters, such as the geometry and mass of the hammer, the geometry, mass and stiffness of the drill bit used, and the stroke of the hammer may likewise be optimized, although not real-time while drilling. It has been found and can be demonstrated that most of the available energy contained in the piston during the power stroke is transferred to the rod [McGregor, 1967], provided that the rod is longer than half the impact wave length, and given that the resistance to the bit is sufficient to enable the rod shank to be impacted.

Bit abrasion, dullness, or wear may be affected by rock abrasiveness and the torque and thrust applied to the bit. Quartz, of course, is harder than most steels. Among different types of

drilling bit cutters, such as steel, Tungsten carbide, natural diamonds, Polycrystalline diamonds (PDC), wear is less rapid for Tungsten carbide because it is marginally harder than silica. Similarly diamonds rapidly lose their ability to cut if they are polished by the dust. Polishing effect may prove to be more deleterious to the bit than a scratch. With percussion drilling, the rocks that need to be considered as highly abrasive are those containing:

- a) Quartz, e.g. quartzite, sandstone, grit and acid-igneous rocks
- b) Other forms of silica, e.g. flint, chert, jasper, and wood-opal
- c) Olivine, e.g. dunite and some forms of basalt
- d) Garnet, e.g. garnetiferous gneiss
- e) Thrust is the force applied to hold a bit against rock so that it could penetrate and drill forward as rock debris is removed during drilling. It can be either dynamic or static: the latter derives from the weight of drilling string and the applied force resulted from a certain “feed mechanism”. In rotary drilling, penetration is proportional to thrust (**Figure 70**). In percussive drilling insufficient thrust produces several undesirable effects, including damage in drill caused by the piston striking the fronthed, heating up of drill rods and bits due to unabsorbed energy, increase of bit wear and rig vibration, which is described as bit “chattering” [Roberts, 1981]
- f) On the other hand, with increasing thrust, penetration increases progressively until an optimum level is reached (**Figure 71**). Further increase gives rise to reduced piston stroke length, bended rods, deviated hole, bit wear, and restricted or stalled bit rotation.

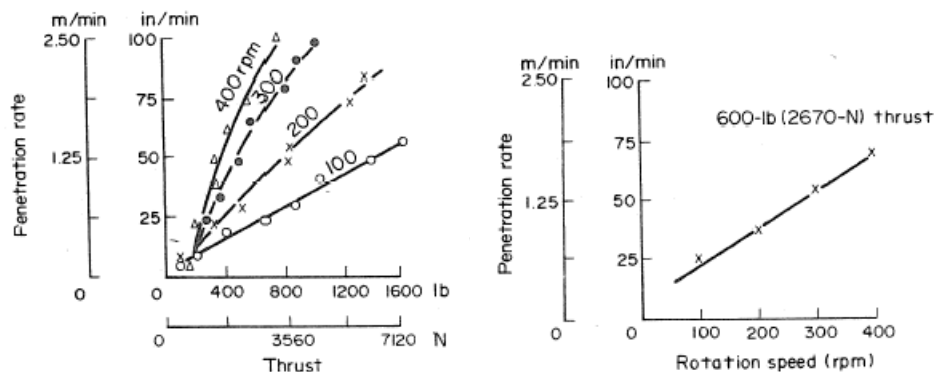


FIGURE 70: Characteristic curves for rotary drag-bit drilling [Fish and Barker, 1956]

Effect of bit rotation speed (RPM) on rock penetration is a double-side blade. Faster rotation results in higher input of cutting energy into the drilled rock due to higher shear stress at the contact of bit and rock and faster cutting speed (**Figure 72**); on the other hand, this requires more power on the ground to drive the rotation and leads to more bit abrasion that decreases penetration and increases drilling cost. Some experiment suggested that different cutting speeds between 10 and 70 in/sec did not produce any significant change in cutting efficiency [Demou et al., 1983]. In down-the-hole drilling, a rotation speed of about 40 RPM is commonly considered to be satisfactory; but in abrasive rock such as quartzite, 10 RPM is recommended. In non-abrasive rocks higher rotation speed can be selected, up to about 100 RPM [McGregor, 1967]. In oil and gas drilling, rotation speed is usually restricted to 30 to 100 RPM.

A side effect of low rotation speed is the vibration, which has been proven more detrimental to bit wear than rotation itself. Therefore diamond-set drill bits operate at fairly high rotational speeds. Higher rotation speed, however, is practical with turbine drills, as these give less

vibration. In certain underground mining operations, particularly in Canada, rotational speeds as high as 3,000 to 4,000 RPM are used with a gain in footage/wear ratio.

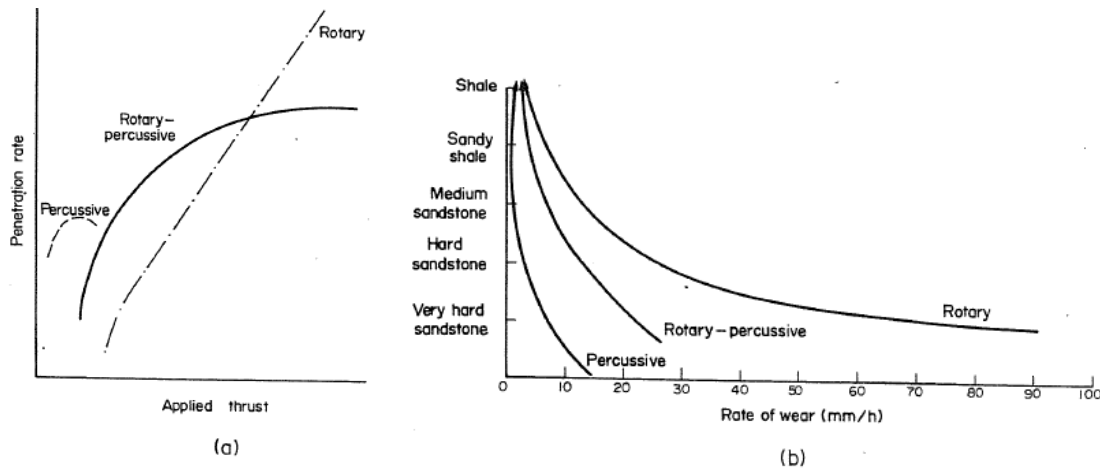


FIGURE 71: a) Typical thrust vs. penetration rate curves; b) Comparative wear rates [Fish, 1961]

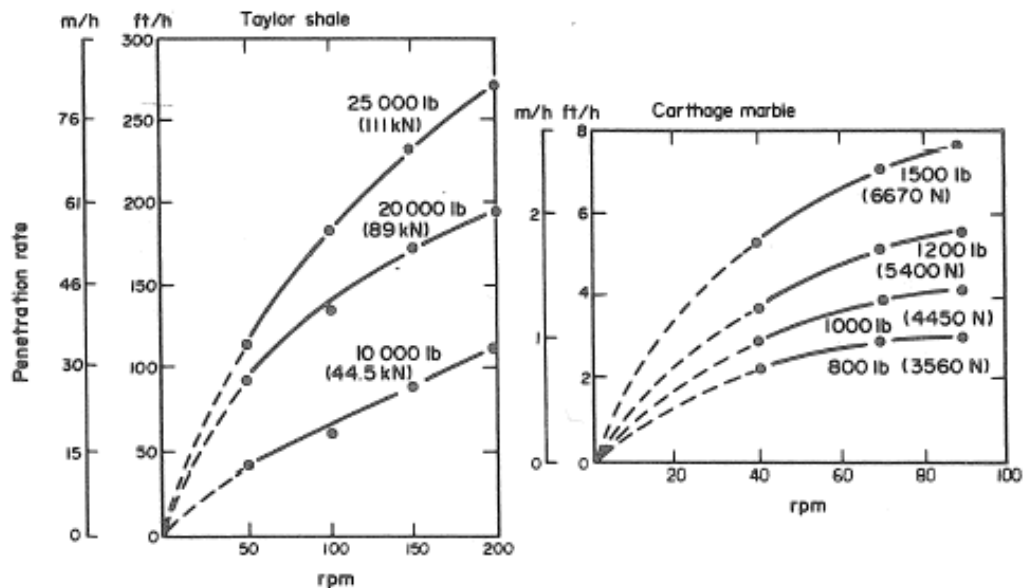


FIGURE 72: ROP vs. RPM at various thrusts on a roller bit [Gatlin, 1960]

Drilling Fluid

Often referred to as “mud” in the oil and gas industries, drilling fluid is critical to underground drilling. With appropriate rheology and circulation, drilling fluid could remove rock debris generated during hole introduction and leave a fresh rock surface for bit to attack. Meanwhile it cools down drill bit, provides pressure support to avoid hole collapse, and serves an effective means to maintain well control.

There are different drilling fluids such as oil-based liquid, water-based liquid, gas or air. Many drilling fluids are a plastic fluid that is complex and non-Newtonian in which the shear

stress is not proportional to the shear rate. A definite pressure (yield point) is required to initiate and maintain movement of the fluid.

A particle suspended in a fluid is subjected to a number of hydrodynamic forces (**Figure 73**). The momentum of a solid particle moving with a fluid can be described as [Bruno et al., 2004]

$$\rho_p V_p \frac{d\vec{v}_p}{dt} = -\rho_f V_p \vec{g} + \int_S \vec{T} \cdot \vec{n} dS \quad (2-86)$$

where V_p is particle volume, ρ_p is its density, \vec{v}_p is the particle velocity vector, S is the particle surface, \vec{n} is a unit vector, and \vec{T} , the instantaneous stress tensor that must satisfy the Navier-Stokes equations, represents all forces between fluid and particle. This include forces from fluid-particle interactions in either laminar or turbulent flow, such as drag force due to fluid viscosity and pressure drop across rock particles, buoyancy force due to density difference of fluid and particles, Basset force due to fluid velocity difference from particles, Magnus force due to particle rotation, inert force due to particle acceleration or deceleration, etc. Effect of pipe rotation on fluid transportation can be estimated with a solution of the circumferential velocity from the Taylor-Couette experiment [Taylor, 1923].

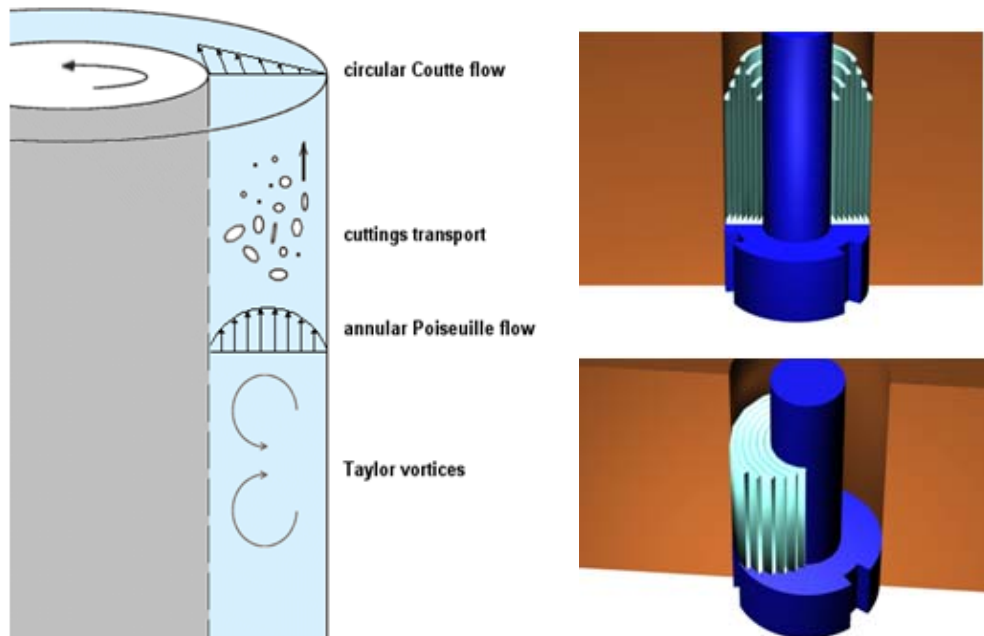


FIGURE 73: Circulation of drilling fluids in well annulus (left) and its radial (top right) and axial (bottom right) flow patterns [Bruno et al., 2004]

2.5 Summary/Conclusions

This chapter is intended to cover the fundamentals of rock and its breakage. We first evaluate drilling-related properties from both terrestrial and extraterrestrial rocks, their determinations, and influence factors. Then stresses are described in sedimentary basin and around borehole.

With understandings of rock properties and stresses, various drilling methods, especially percussive and rotary, are investigated.

2.5.1 Underground Rocks and Stresses

Rocks involved in drilling could be classified into three groups: igneous, sedimentary, and metamorphic. Rock response to drilling activities relies not only on the level of applied loads, but also on rock characteristics, including elastic, strength, and transport properties. Various moduli such as Young's modulus, bulk modulus, shear modulus, and the modulus of toughness, along with Poisson's ratio and bulk compressibility, describes rock elastic deformation. Rock strengths such as shear strength, uniaxial compressive strength (UCS), residual strength, etc. define the loading capacity of rock. If rock is saturated with fluid, porosity and permeability are used to quantify its transport properties.

Rock properties are often related to each other. For example, various correlations have been developed between rock strength and porosity, or among rock strength and moduli variables themselves. Rock mechanical properties are affected by many internal and external conditions. Factors include grain size, cement type, contact pattern, in-situ stress level, temperature, cracks and fissures, rock heterogeneity, etc. Laboratory testing conditions such as loading rate, coring method, specimen geometry, and so on, could further complicate the estimation of the properties.

They could be determined either through static laboratory tests or dynamic logging method.

- In the laboratory, rock cores must be carefully preserved and tested under high-quality conditions to determine mechanical, transport and chemical rock properties for design and analysis. Triaxial tests are the standard method of obtaining information on deformation and strength behavior for stability analysis in drilling. Drill chips and poorer quality core can still be of value, as these materials can be assessed using rapid index tests to use as correlates to mechanical and transport properties.
- In field, elastic constants are dynamically estimated from sonic wave velocities, bulk density, and shale content. Sonic waves are also sensitive to the presence of fluids and the level of in-situ stresses. Furthermore, the ratio of compressional and shear wave velocities is an indicator of formation consolidation. Even though rock strength cannot be measured directly from logs, consistent efforts have been made to develop empirical correlations between rock strength and other measurements. Due to the empirical nature of these correlations, calibrations should be made before applying to a field.

Subsurface drilling will likely play a large role in future exploration as planetary missions increase in scope and complexity. Knowledge of the physical and mechanical properties of planetary materials are derived from a number of sources, including meteorites, in situ measurements from landed spacecraft, and inferences from remote measurements. The only extraterrestrial drill cores returned to Earth are the lunar drill cores obtained by the Apollo and Luna missions. These samples and the experience gained through their extraction provide invaluable guides for future drilling into planetary regolith environments, especially on atmosphereless bodies such as asteroids or the planet Mercury. A second source of physical properties data that may help guide future exploration efforts are data from penetrometers, which have been successfully flown on landed missions to the Moon, Mars, Venus, and Titan.

In situ stresses and pressures are vital data required for analysis as these values, combined with material properties and geometrical disposition, define the initial conditions for all analyses including flow response, fracturing behavior, mechanical stability, drillability, and so on.

Stress magnitudes and orientations can be estimated using large-scale tectonic fabric, geological history, depth and lithostratigraphic disposition. This provides valuable general data that can be used to design drilling programs and even to make preliminary assessments of casing points. However, for risk management, it is necessary to obtain more precise estimates of stresses and pressure. Direct measurements of in situ stresses are mainly based on variations of hydraulic fracturing methods, which also include leak-off tests, extended leak-off tests, and formation integrity tests. Borehole seismic and regional seismic methods can help give some indication in certain conditions using calibrations and correlations as well as factor such as shear wave anisotropy, which is likely related to stress directions. Pore pressures are usually measured directly with borehole methods, although new seismic methods combined with knowledge of the geological and tectonic history can help in pressure estimates.

Indirect measures of stress magnitudes and orientation can be provided by geophysical log data (anisotropic response, breakouts, axial fractures), or else cores can be tested in certain ways to allow estimates to be made. For example, careful ultrasonic velocity measurements on oriented core shows anisotropy that may be related to the stress orientations in situ.

Stresses and pressures dictate where casing points will be placed. The limiting factors are borehole instability or blowout conditions at the bit, as well as the hydraulic fracturing pressure at the shoe. As one drills deeper below an existing casing shoe, these values generally become nearer to one another until they are virtually the same, dictating need for a new casing string.

Stresses can be altered through drilling itself (creating an opening), by changes in pressure, through temperature changes, and by chemical effects such as salt dissolution or exposure of shale to drilling fluids of different chemistry. These factors of course can be controlled to increase borehole stability in various stress regimes.

The solutions of elastic and inelastic stresses around a vertical hole with or without fluid flow are given in this chapter. For a weak formation, a Coulomb zone near the wellbore has been identified. In this zone, rock has yielded and been damaged to a certain extent but has not completely lost its functionality and collapsed into the borehole. For a strong rock with low in-situ stresses, such zone may not exist. When far field stresses are anisotropic horizontally, rock deformation concentrates in the direction of minimum horizontal stress, and represents the highest risk of borehole instability or collapse.

2.5.2 Drilling Theories

Among various rock removal techniques, percussive and rotary drills are probably the two most widely used.

With long history, percussion drilling has been recognized as a fast rock penetration method, even faster than rotary drill or diamond drill in some hard formations. Merits such as low requirement of Weight-on-Bit, less bit-rock contact time, longer bit life, less hole deviation, larger cuttings, etc. have encouraged people to apply percussion drilling to both terrestrial and extraterrestrial rocks. Meanwhile, inclusive overall results, risks in operations, and economical uncertainties greatly limit the wider acceptance of this technology.

Percussion drilling involves four fundamental processes: 1) drillbit penetrates rock with compression and vibration; 2) rock receives impact, stress propagates, and damage accumulates; 3) rock fails and disaggregates; and 4) cuttings are transported away from the bit and up in the annulus. These are coupled physical processes, with different physics related to the tool and bit mechanics, rock mechanics, and cuttings transport mechanics.

To improve the understandings of rock physics in percussion drilling two groups of lab tests are summarized in the chapter: single impact tests and full-scale hammer tests. In single impact tests, both the stress inside the rock samples and the stress of the steel rod were recorded at a frequency as high as 91 kHz, along with the displacement of the rod. For each rock sample, three impacts were sequentially loaded at the same rock location to investigate the effect of cyclic loading on rock damage. Meanwhile full-scale drilling tests were carried out with an industry mud hammer and in-situ high stress conditions. Both underbalanced and overbalanced conditions were investigated.

The studies have shown when a hammer impacts rock, some stress waves are transferred from the hammer to rock while the other waves are reflected and dissipated mechanically and thermally. Different failure mechanisms have been involved at different stage of hammer-rock impact: compressive failure occurs in a stress concentration zone with high compressive and can extend several diameters deeper than the penetration depth of the cutter; tensile fractures are critical for efficient rock breakage in percussion drilling and generally formed outside the edge of the compressive zone, tipped toward the surface. When there is little bottomhole pressure (BHP) compressing rock surface, rock may more easily break in tension, not only when the bit impacts but when the bit retreats. The indentation data from single impact tests, the hammer performance from full-scale drilling tests, as well as the cuttings collected, all indicate the existence and the importance of tensile failure in breaking rock in percussion drilling.

An analytical model for describing the interaction between adjacent cutters in a coring bit is derived for the coring bits with wedge-shape cutting teeth of vibratory drills that percussively penetrate into brittle material. The overall coring bit specific energy is derived as a function of the cutters spacing and teeth number. There exists an optimal spacing/depth ratio or an optimal teeth number that minimize coring bit specific energy and hence maximize its drilling rate. Experimental drilling tests have been performed and confirmed the theoretical development.

Different indexes have been used in different industries to evaluate drilling efficiency, such as specific energy, rock drillability, and rate of penetration. Possibilities that may improve or withhold drilling efficiency may belong to either static or dynamic groups. Static variables refers to the parameters that hardly change with time once equipment is installed in place, such as bit hardness and strength, rock strength, abrasiveness, hardness, etc. Dynamic parameters are manageable and may change with time of drilling such as hammer energy, bit abrasion, bottom hole pressure, thrust force, weight on bit, rotation speed, drilling fluid, etc. To improve drilling efficiency, we should marry the designs of bit and drilling system with the understandings of rock properties and behaviors.

2.5.3 *Effect of environment on the drilling*

The effect of temperature on the strength of rock was found by many researchers to be quite significant [Heins and Friz 1967; Mellor 1971; Zacny and Cooper 2007]. Since the drillability of rocks and required Weigh-on-Bit to achieve penetration are inversely proportional to rock strength (i.e. with higher rock strength it is more difficult to drill a rock), it is expected that the low temperature may in turn affect the efficiency of the rock breaking process. Heins and Friz [1967] found that the strength of an oven-dried basalt rock increases by 50% when cooled down to -80°C, which means, that in theory the required Weight-on-Bit to allow the cutter to penetrate the rock would be 50% higher and also, the power required to drill will also be 50% higher. In practice, however, the rock in the immediate vicinity of a drill bit will heat up, and as a result the effect of the low temperature will somewhat be diminished.

2.6 Acknowledgement

The authors deeply appreciate the generous and professional efforts from the three technical reviewers: Earling Fjaer, Chief Scientist at SINTEF in Trondheim, Norway; Robert W. Zimmerman; Head of the Division of Engineering Geology and Geophysics at the Royal Institute of Technology in Stockholm, Sweden; Constantinos Mavroidis, Director of the Biomedical Mechatronics Laboratory, Department of Mechanical and Industrial Engineering at Northeastern University in Boston, Massachusetts, USA. The authors would like to acknowledge Yoseph Bar Cohen of Jet Propulsion Lab/Caltech/NASA for helping in completing the chapter, and for his countless suggestions that helped to make the chapter a stimulating read. Our gratefulness is also extended to Patrick Fink, Honeybee Robotics, for his help with this Chapter references.

The percussion drilling research was originated and sponsored by the National Energy Technology Laboratory at Department of Energy; some other studies in this chapter were conducted at the Jet Propulsion Laboratory (JPL), California Institute of Technology, and Honeybee Robotics Spacecraft Mechanisms Corporation under a contract with the National Aeronautics and Space Administration (NASA).

2.7 Nomenclature

C : rock compressibility;
 C_b : bulk compressibility;
 C_f : compressibility of pore fluid;
 C_m : rock matrix compressibility;
 C_s : compressibility of the reservoir solid material;
 c_o : rock cohesive strength;
 d : diameter of grain (grain size), depth of cut;
 E : Young's modulus, specific energy;
 E_s, E_d : Static and dynamic Young's modulus;
 F_c : capillary force;
 G : shear modulus, modulus of rigidity;
 h : formation thickness;
 K : bulk modulus;
 K' : ratio of the horizontal to vertical effective stresses;
 k : permeability;
 M_t : modulus of toughness;
 P : fluid pressure, rate of energy dissipation at the bit-rock interface;
 P_c : capillary pressure;
 Q : volume flow rate per unit time;
 R : particle radius, borehole radius;
 S : specific surface area, drilling strength;
 T : temperature, torque on bit;
 V : volume, rate of penetration;
 V_{sh} : volume of shale;
 v_p, v_s : velocities of compressional wave and shear wave;

W : weight on bit;
 α : Boit's poroelastic constant;
 β : rock failure angle;
 β_T : linear coefficient of thermal expansion;
 λ : Lamé elastic constant, factor accounting for non-uniform particle size effect on rock strength;
 η : drilling efficiency
 ϕ : rock porosity;
 φ : internal friction angle;
 ρ : rock density;
 ρ_b : rock bulk density;
 ρ_s : solid grain density;
 ρ_f : pore fluid density;
 Ω : angular velocity;
 γ : surface tension;
 μ : coefficient of friction, fluid viscosity;
 ν : Poisson's ratio;
 σ : total stress;
 $\sigma_x, \sigma_y, \sigma_z$: stresses in the direction of x, y, z at Cartesian coordinate;
 σ_r, σ_θ : radial and tangential stresses at cylindrical coordinate;
 $\sigma_v, \sigma_{HMAX}, \sigma_{Hmin}$: vertical, maximum, and minimum horizontal principal stresses;
 $\sigma_1, \sigma_2, \sigma_3$: maximum, medium, and minimum principal normal stresses;
 $\sigma'_1, \sigma'_2, \sigma'_3$: maximum, medium, and minimum effective principal stresses;
 σ_c : rock compressive strength;
 σ_T : tensile strength;
 τ : shear stress;
 ε : strain, intrinsic specific energy;
 $\varepsilon_x, \varepsilon_y, \varepsilon_z$: rock strain in the direction of x, y, z at Cartesian coordinate;
 $\varepsilon_r, \varepsilon_a$: radial and axial strain;
 $\bar{\varepsilon}_z$: critical strain for rock failure in compression;
BHP: Bottom Hole Pressure;
PDC: Polycrystalline Diamond Compacts;
ROP: Rate of Penetration;
RPM: Rotation per Minute;
UCS: Uniaxial Compressive Strength;
WOB: Weight on Bit;

2.8 References

- Adams, W. M., "Nuclear Reactor Apparatus for Earth Penetration," US Patent No. 3155194, (1965).
Almenara, R. and E. Detournay, "Cutting Experiments in Sandstones with Blunt {PDC} Cutters," *Proc. EuRock '92*, Thomas Telford, London, (1992), pp. 215-220.

- ASTM, "Standard Test Methods for Maximum Index Density and Unit Weight of Soils Using a Vibratory Table," ASTM International, Publication No. D 4253, (2000).
- Basilevsky, A. T., R. O. Kuzmin, O. V. Nikolaeva, A. A. Pronin, L. B. Ronca, V. S. Avduevsky, G. R. Uspensky, Z. P. Cheremukhina, V. V. Semenchenko, and V. M. Ladygin, "The Surface of Venus as Revealed by the Venera Landings: Part II," Geological Society of America Bulletin, Vol. 96, (1985), pp.137-144.
- Bates, R. E., "Field Results of Percussion Air Drilling," The 39th SPE Annual Fall Meeting, Houston, TX, USA, SPE 886, (October 11-14, 1964).
- Beer, F. P., Johnston, E. R. and J. T. deWolf, *Mechanics of Materials* McGraw-Hill, New York, 4th Edition, (2005), p. 800.
- Bell, F. G., "The Physical and Mechanical Properties of the Fell Sandstones," Engineering Geology, Northumberland, England, Vol. 12, (1978), pp. 1-29.
- Besson, A., B. Burr, S. Dillard, E. Drake, B. Ivie, C. Ivie, R. Smith, and G. Watson, "On the Cutting Edge," Oilfield Review, (2000). Black, A. D., B. H. Walker, G. A. Tibbitts, and J. L. Sandstrom, "PDC Bit Performance for Rotary, Mud Motor, and Turbine Drilling Applications," SPE Drilling Engineering, (1986), pp. 409-416.
- Brady, B. H. G. and E. T. Brown, *Rock Mechanics for Underground Mining*, George Allen & Unwin Ltd, London, UK, 1985.
- Brett, J. F., "The Genesis of Torsional Drillstring Vibrations," SPE Drilling Engineering, (September 1992), pp. 168-174.
- Bruce, S., "A Mechanical Stability Log," The 1990 IADC/SPE Drilling Conference, Houston, Texas, SPE/IADC 19942, (February 27 - March 2, 1990).
- Bruno, M., G. Han, and C. Honeger, "Advanced Simulation Technology for Combined Percussion and Rotary Drilling and Cuttings Transport," GasTips, Vol. 11, No. 9, (Winter, 2004), pp. 5-8.
- Bui, H., J. Meyers, and S. Swadi, "Steerable Percussion Air Drilling System," DOE Contractor Review Meeting, Baton Rouge, USA, (April, 1995).
- Burshtein, L. S., "Effect of Moisture on the Strength and Deformability of Sandstone," Soviet Mining Science, Vol. N4, (1969), pp. 573-576.
- Byrne, P. M., H. Cheung, and L. Yan, "Soil Parameters for Deformation Analysis of Sand Masses," Canadian Geotechnical Journal, Vol. 24, (1987), pp.366-376.
- Carmichael, R. S., "Handbook of Physical Properties of Rocks," ISBN-13: 9780849302282, CRC Press, Vol. 2, USA, (1982).
- Carrier, W. D. III, "Apollo Drill Core Depth Relationships," Moon. 10, (1974), pp. 183-194.
- Carrier, W. D. III, J. K. Mitchell, and A. Mahmood, "The Relative Density of Lunar Soil," Proceedings of the 4th Lunar and Planetary Science Conference, (1973), pp. 2403-2411.
- Carrier, W. D. III, G. R. Olhoeft, and W. Mendell, *Physical Properties of the Lunar Surface, in The Lunar Sourcebook*, G. H. Heiken et al. (Ed.), Cambridge UP, New York, (1991), pp. 475-594.
- Cheatham, J.B. Jr., "The State of Knowledge of Rock/Bit Tooth Interactions under Simulated Deep Drilling Conditions," TerraTek Report, (1977).
- Cherkasov, I. I., A. L. Kemurdzhian, L. N. Mikhailov, V. V. Mikheev, A. A. Morozov, A. A. Musatov, I. A. Savenko, M. I. Smorodinov and V. V. Shvarev, "Determination of the Density and Mechanical Strength of the Surface Layer of Lunar Soil at the Landing Site of the Luna 13 Probe," Kosmicheskie Issledovaniya, 5(5), (1967), pp. 746-757, in Russian.

- Choate, R., S. A. Batterson, E. M. Christensen, R. E. Hutton, L. D. Jaife, R. H. Jones, H. Y. Ko, R. F. Scott, R. L. Spencer, F. B. Sperling and G. H. Sutton, "Lunar Surface Mechanical Properties," *Surveyor Project Final Report, Part 2*, NASA Technical Report 32-1265, Jet Propulsion Laboratory, (1968), pp. 137-194.
- Coates, G. R., R. P. Schluzer, and W. H. Throop, "VOLAN - an Advanced Computational log Analysis," Proceedings of the SPWLA 23rd Annual Logging Symposium, Corpus Christi, Texas, Paper A., (July 6-9, 1982).
- Coats, G. R. and S. A. Denoo, "Mechanical Properties Program Using Borehole Analysis and Mohr's Circle," Proceedings of the SPWLA 22nd Annual Logging Symposium, Houston, Texas, USA, (June 23-26, 1981).
- Colback, P. S. B. and B. L. Wiid, "The Influence of Moisture Content on the Compressive Strength of Rock," Proceedings of the 3rd Canadian Symposium of Rock Mechanics, Toronto, (1965), pp.65-83.
- Collins, P. M., "Geomechanical Effects on the SAGD Process," SPE Reservoir Evaluation & Engineering, Vol. 10, No. 4, SPE 97905-PA, (August, 2007).
- Cunningham, R. A. and J. G. Eenink, "Laboratory Study of Effect of Overburden, Formation, and Mud Column Pressure on Drilling Rate of Permeable Formations," Journal of Petroleum Technology, Transaction of AIME, 204, (January, 1959), pp. 9-15.
- Dagrain, F., *Etude des Mécanismes de Coupe de Roches avec Couteaux Usés. Approche des Mécanismes de Frottement sous les Couteaux par le Concept du Troisième Corps*, PhD thesis, Université Polytechnique de Mons., (2006).
- Dagrain, F., T. Richard, and E. Detournay, "Determination of Rock Strength Properties from Scratching Tests," International Journal of Rock Mechanics and Mining Sciences, (2008), to be submitted.
- Davies, J. P., and D. K. Davies, "Stress-Dependent Permeability: Characterization and Modeling," SPE Journal, SPE 71750, (June, 2001), pp. 224-235.
- Deily, F. H. and A. J. Durelli, "Bottom Hole Stress in A Well Bore," The SPE Annual Meeting, Houston, SPE 1095, Texas, USA, (October 5-8, 1958).
- Deliac, E. P., *Optimization des Machines d'Abattages à Pics*, PhD thesis, Université Pierre et Marie Curie, Paris, (1986).
- Demou, S. G., R. C. Olson, and C. F. Wingquist, "Determination of Bit Forces Encountered in Hard Rock Cutting for Application to Continuous Miner Design," *Report of Investigations 8748*, United States Department of the Interior and Bureau of Mines, (1983).
- Detournay, E. and P. Defourny, "A Phenomenological Model of the Drilling Action of Drag Bits," International Journal of Rock Mechanics and Mining Sciences, Vol. 29, No. 1), (1992), pp. 13-23.
- Detournay, E. and A. Drescher, "Plastic Flow Regimes for a Tool Cutting a Cohesive-Frictional Material," Proceedings of the 4th International Symposium on Numerical Methods in Geomechanics (NUMOG IV), Rotterdam, Balkema (1992).
- Detournay, E. and C. Atkinson, "Influence of Pore Pressure on the Drilling Response in Low-Permeability Shear-Dilatant Rocks," International Journal of Rock Mechanics and Mining Sciences, Vol. 37, No. 7), (2000), pp. 1091-1101.
- Detournay, E., and T. Richard, "Mechanics of Rock Cutting," International Journal of Rock Mechanics and Mining Sciences, (2008), in preparation.

- Detournay, E., T. Richard, and M. Shepherd, "Drilling Response of Drag Bits: Theory and Experiment," *International Journal of Rock Mechanics and Mining Sciences*, (2008), in press.
- Donaghe, R. T., R. C. Chaney, and M. L. Silver, (Editors), "Advanced Triaxial Testing of Soil and Rocks," *Proceedings of the 1986 ASTM Symposium*, Louisville Kentucky, ASTM Committee D-18, (1988), p. 896
- Duke, M. B. and J. S. Nagle, "Lunar Core Catalog," NASA Johnson Space Center, JSC09252, (1974), p. 242.
- Dullien, F. A. L., *Porous Media: Fluid Transport and Pore Structure*, Academic Press, New York, USA, (1979).
- Duncan, J. M. and C. Y. Chang, "Nonlinear Analysis of Stress and Strain in Soils," *Journal of the Soil Mechanics and Foundations Division*, *Proceedings of the ASCE*, SM5, (September 1970), pp.1629-1652.
- Dusseault, M. B. and Fordham, C. J., "Time Dependent Behaviour of Rocks," *Comprehensive Rock Engineering*, Vol. 3, Hudson, J. A. (Ed.), Pergamon Press, (1994), 119-149.
- Dusseault, M. B., P. Cimolini, H. Soderberg, and D. W. Scafe, "Rapid Index Tests for Transitional Material," *ASTM Geotechnical Testing Journal*, Vol. 6, No. 2, (1983), pp. 64-72.
- Ewy, R. T., C. A. Bovberg, G. Chen, R. Jansson, and G. Pepin, "Fatigue Testing of Hollow Cylinders and Application to Injection Well Cycling," *The 6th North America Rock Mechanics Symposium*, Houston, TX, USA, ARMA/NARMS 04-464, (June 5-9, 2004).
- Fairhurst, C., and W. D. Lacabanne, "Some Principles and Developments in Hard Rock Drilling Techniques," *Proceedings of the 6th Annual Drilling and Blasting Symposium*, Minnesota University, (1956), pp. 15-25.
- Fish, B. G., "Research in Rock Drilling and Tunneling," *Min. Elect. Mech. Engr.*, (February 1961), pp. 1-13.
- Fish, B. G. and J. S. Barker, "Studies in Rotary Drilling," *National Coal Board*, MRE Rep. No. 209, (1956).
- Fjær, E., R. M. Holt, P. Horsrud, A. M. Raaen, and R. Risnes, *Petroleum Related Rock Mechanics*, Elsevier Science Publishers B.V., The Netherlands, (1992).
- Gardner, G. H. F. and M. H. Harris, "Velocity and Attenuation of Elastic Waves in Sands," *9th Annual Logging Symposium*, (1968), pp. M1-M19.
- Gatlin, C., *Petroleum Engineering*, Prentice-Hall, London, UK, (1960).
- Ghalambor, A., A. Hayatdavoudi, and R. J. Koliba, "A Study of Sensitivity of Relevant Parameters to Predict Sand Production," *The 3rd Latin American/Caribbean Petroleum Engineering Conference*, Buenos Aires, Argentina, SPE 27011, (April 27-29, 1994).
- Giles, C. A., T. Seesahai, J. W. Brooks, and W. Johnatty, "Drilling Efficiencies Provided by Hydraulic Thrusting Devices," *the AADE 2001 National Drilling Conference*, Houston, Texas, USA, (March 27-29, 2001).
- Green, S., A. Judzis, D. Curry, A. Black, U. Prasad, and J. Rogers, "Single Cutter Impact Tests Investigate Deep-Well Hammer-Drilling Performance," *The SPE Annual Technical Conference and Exhibition*, Dallas, Texas, USA, SPE 97173, (October 9-12, 2005).
- Gregory, A. R., "Fluid Saturation Effects on Dynamic Elastic Properties of Sedimentary Rocks," *Geophysics*, Vol. 41, No. 5, (October, 1976), pp. 895-921.
- Griggs, D. T. and J. D. Blacic, "Quartz: Anomalous Weakness of Synthetic Crystals", *Science*, Vol. 147, (1965), pp.292-295.

- Griggs, D. T., "Hydrolytic Weakening of Quartz and Other Silicates," *Geophys. J. R. Astr. Soc.*, Vol. 14, (1967), pp. 19-31.
- Haimson, B. C., "Effect of Cyclic Loading on Rock, Dynamic Geotechnical Testing," American Society for Testing and Materials, ASTM STP 654, (1978), pp. 228-245.
- Han, G. and M. Bruno, "Percussion Drilling: from Lab Tests to Dynamic Modeling," SPE International Oil & Gas Conference and Exhibition in China, Beijing, P. R. China, SPE 104178, (December 5-7, 2006).
- Han, G. and M. B. Dusseault, "Quantitative Analysis of Mechanisms for Water-related Sand Production," Proceedings of the SPE International Symposium and Exhibition on Formation Damage Control, Lafayette, Louisiana, USA, SPE73737, (Feb 20-21, 2002).
- Han, G. and M. B. Dusseault, "Description of Fluid Flow around a Wellbore with Stress-Dependent Porosity and Permeability," *Journal of Petroleum Science and Engineering*, Vol. 40, No. 1/2, (2003), pp. 1-16.
- Han, G. and M. B. Dusseault, "Sand Stress Analysis around a Producing Wellbore with a Simplified Capillarity Model," *International Journal of Rock Mechanics and Mining Science*, Vol. 42, No. 7-8, (2005), pp. 1015-1027.
- Han, G., M. Bruno, M. B. Dusseault, and B. Xu, "Rock Nonlinearities in the Oil-Water Environment around a Wellbore," Proceedings of 3rd ARMS (Asian Rock Mechanics Symposium), Kyoto, Japan, (November 30 - December 2, 2004), pp. 335-340.
- Han, G., M. B. Dusseault, and J. Cook, "Quantifying Rock Capillary Strength Behavior in Unconsolidated Sand," Proceedings of the SPE/ISRM Rock Mechanics Conference, Irving, Texas, USA, SPE 78170, (October 20-23, 2002).
- Han, G., M. Bruno, and K. Lao, "Percussion Drilling in Oil Industry: Review and Rock Failure Modelling," The AADE National Technical Conference & Exhibition, Houston, Texas, USA, AADE-05-NTCE-59, (April 5-7, 2005, a).
- Han, G., M. Bruno, and M. B. Dusseault, "Dynamically Modelling Rock Failure in Percussion Drilling," The 40th US Rock Mechanics Symposium, Anchorage, Alaska, USA, ARMA/USRMS 05-819, (June 25-29, 2005, b).
- Han, G., M. Bruno, and T. Grant, "Lab Investigations of Percussion Drilling: from Single Impact to Full Scale Fluid Hammer," The 41st US Rock Mechanics Symposium, Colorado School of Mines, Golden, Colorado, USA, ARMA/USRMS 06-96, (June 17-21, 2006).
- Harpst, W. E. and E. E. Davis, "Rotary Percussion Drilling," *Oil and Gas Journal*, (November 1949), p. 10.
- Hartman, H. L., "The Effectiveness of Indexing in Percussion and Rotary Drilling," *International Journal of Rock Mechanics and Mining Science & Geomechanics Abstracts*, Vol. 3, No. 4, (November 1966), pp. 265-278.
- Hawkins, A. B. and B. J. McConnell, "Sensitivity of Sandstone Strength and Deformability to Changes in Moisture Content," *Quarterly Journal of Engineering Geology*, Vol. 25, (1992), pp. 115-130.
- Heins R. and T. Friz, "The Effect of Low Temperature on Some Physical Properties of Rock," Society of Petroleum Engineers, SPE 1714, (1967).
- Ho, H. S., "Prediction of Drilling Trajectory in Directional Wells Via a New Rock-Bit Interaction Model," Proc. SPE Annual Technical Conference and Exhibition, SPE 16658, (1987).
- Holt, R. M., "Permeability Reduction Induced by a Nonhydrostatic Stress Field," *SPE Formation Evaluation*, Vol. 5, No. 4, (Dec 1990), pp. 444-448.

- Huang, H. and E. Detournay, "Intrinsic length scales in tool-rock interaction," *Int. J. Geomechanics*, Vol. 8, No. 1, (January-February, 2008) pp. 39-44.
- Huang, H., E. Detournay, and B. Bellier, "Discrete Element Modelling of Rock Cutting," *Rock Mechanics for Industry*, Amadei B., Z. Kranz, G. A. Scott, and P. H. Smeallie, (Eds.) , Rotterdam, Balkema, (1999) pp. 123-130.
- Jaeger, J. C., N. G. W. Cook, and R. W. Zimmerman, *Fundamentals of Rock Mechanics*, Blackwell, Oxford, UK, 2007.
- John, M., "The Influence of Loading Rate on Mechanical Properties and Fracture Processes of Rock," Republic of South African CSIR, Meg. 1115, (1972), p. 28.
- Kemurdzhian, A. L., V. V. Gromov and V. V. Shvarev, "Investigation of the Physicomechanical Properties of Extraterrestrial Soils," *Soviet Progress in Space Studies: The Second Decade of Space Flight, 1967-1977*, Blagonravov, A. A. et al. (Eds.), Nauka, Moscow, (1978), pp. 352-380 (in Russian).
- King, M. S., "Static and Dynamic Elastic Moduli of Rocks under Pressure," Proceedings of 11th Symposium on Rock Mechanics, University of California, Berkely, CA, (June 1969).
- Kohata, Y., F. Tatsuoka, L. Wang, G. L. Jiang, E. Hoque, and T. Kodaka, "Modelling the Non-linear Deformation Properties of Stiff Geomaterials," *Geotechnique*, Vol. 47, No.3, (1997), pp.563-580.
- Kömle, N. I., G. Kargl, A. J. Ball, "Determination of Physical Properties of Planetary Sub-surface Layers by Artificial Impacts and Penetrometry," *Advances in Space Research*, Vol. 28, No. 10, (2001), pp. 1539-1549.
- Kong, J., C. Marx, and P. J. Palten, "Mathematical Simulation of a Spring-Free Hydraulic Drilling Hammer and Verification of the Results by Experiment," *Erdol Erdgas Kohle*, Vol. 112, No.1, (1996), pp.19-25.
- Kulhawy, F. H., and J. M. Duncan, "Stress and Movements in Oroville Dam," *Journal of the Soil Mechanics and Foundations Division*, Proceedings of the American Society of Civil Engineers, SM7, (July 1972), pp. 653-665.
- Lama, R. D. and V. S. Vutukuri, *Handbook on Rock Properties of Rocks*, Trans Tech Publications, (1978).
- Larson, D. A., and R. C. Olson, "Design Considerations of Mechanical Fragmentation Systems for Entry Development in Oil Shale," *Proc. 10th Oil Shale Symp.*, Colorado School of Mines Press, Golden, Colorado, USA, (April 1977), pp. 99-119.
- Le Pennec, T., K. Jørgen Måløy, E. G. Flekkøy, J. C. Messenger, and M. Ammi, "Silo Hiccups: Dynamic Effects of Dilatancy in Granular Flow," *Physics of Fluids*, Vol.12, No.12, (Dec.1998), pp. 3072-3079.
- Lebreton, J. P. and D. L. Matson, "The Huygens Probe: Science, Payload and Mission Overview," *Space Science Reviews*, 104, (2002), pp. 59-100.
- Lee, L. K. and H. B. Seed, "Drained Strength Characteristics of Sands," *Journal of the Soil Mechanics and Foundation Division*, Proceedings of the ASCE, SM6, (November 1967), pp.117-141.
- Leonard, R., "Features - Groundwater Development - Tough Down Hole Drilling Demands Expand Bit Options: Ralph Leonard of Numa Explains Drill Bit Options for Down Hole Percussion Drilling Applications," *Water and Wastewater International*, Vol. 16, No. 2, (2001), p. 17.
- Lhomme, T., *Frictional contact at a rock-tool interface: An experimental study*, Master's thesis, University of Minnesota, (1999).

- Liu, Y., C. Mavroidis, Y. Bar-Cohen and Z. Chang, "Analytical and Experimental Study of Determining the Optimal Number of Wedge Shape Cutting Teeth in Coring Bits Used in Percussive Drilling," *Journal of Manufacturing Science and Engineering, Transactions of the ASME*, Vol. 129, Issue 4, (August 2007), pp. 760-769.
- Lorenz, R.D. and A.J. Ball, "Review of Impact Penetration Tests and Theories," *Penetrometry in the Solar System*, Kömle, N. I., G. Kargl, A. J. Ball and R. D. Lorenz (Eds.), Austrian Academy of Sciences Press, (2001), pp. 25-39.
- LSPET (The Lunar Sample Preliminary Examination Team), "Preliminary Examination of Lunar Samples," *Apollo 17 Preliminary Science Report*, NASA Special Publication 330, Johnson Space Center, (1973), pp. 7-1 to 7-46.
- Maurer, W. C., "Bit Tooth Penetration Under Simulated Borehole Conditions," *Journal of Petroleum Technology, Transaction of AIME*, 234, (December 1965), pp.1433-1442.
- McGhee, E., "New Down-Hole Tool," *Oil and Gas Journal*, (August 1955), p. 67.
- McGregor, K., *The Drilling of Rock*, CR Books Ltd., London, UK, (1967).
- McKay, D. S., G. Heiken, A. Basu, G. Blanford, S. Simon, R. Reedy, B. M. French, and J. Papike, "The Lunar Regolith," *The Lunar Sourcebook*, Ed. Heiken, G. H. et al., Cambridge UP, New York, (1991), p. 285-356.
- Melamed, Y., A. Kiselev, M. Gelfgat, D. Dreesen, and J. Blacic, "Hydraulic Hammer Drilling Technology: Developments and Capabilities," *Journal of Energy Resources Technology*, Vol. 122, No. 1, (2000), pp. 1-8.
- Mellor, M., "Strength and Deformability of Rocks at Low Temperatures," CRREL RR 294, (1971).
- Miner, J. W., D. R. Heyse, and P. M. Boonen, "Initial Results from an Acoustic Logging-While-Drilling Tool," SPE Annual Technical Conference and Exhibition, Denver, Colorado, USA, SPE 36543, (October 6-9, 1996).
- Mission Evaluation Team, *Apollo 17 Mission Report*, Johnson Space Center, Houston Texas, (1973), p. 349.
- Mitchell, J. K., W. N. Houston, W. D. Carrier III, and N. C. Costes, "Apollo Soil Mechanics Experiment S-200," *Space Sciences Laboratory Series 15, Issue 7 University of California, Berkeley*, (1974), p. 135.
- Moore, H. J., R. E. Hutton, G. D. Clow, and C. R. Spitzer, "Physical Properties of the Surface Materials at the Viking Landing Sites on Mars," *U.S. Geological Survey Professional Paper 1389*, U.S. Government Printing Office, Washington, D.C., (1987), p. 222.
- Morita, N., K. E. Gray, F. A. A. Srouji, and P. N. Jogi, "Rock Property Changes During Reservoir Compaction," *SPE Formation Evaluation*, Vol. 7, No. 3, SPE 13099, (September 1992), pp. 197-205.
- Morris, R. V., H. V. Lauer, Jr., and W. A. Gose, "Characterization and Depositional and Evolutionary History of the Apollo 17 Deep Drill Core," *Proceedings of the 10th Lunar and Planetary Science Conference*, (1979), pp. 1141-1157.
- Nishimatsu, Y., "Theories of Rock Cutting," *Comprehensive Rock Engineering*, Ed. Hudson, J. A., Vol. 1, Pergamon Press Ltd., Oxford, (1993) pp. 647-662.
- Ostrovskii, N. P., "Deep-Hole Drilling with Explosives," *Gostoptekhzat*, Moscow, Trans. Consultants Bureau Enterprises, Inc., New York, (1960).
- Papamichos, E., M. Brignoli, and F. J. Santarelli, "An Experimental and Theoretical Study of a Partially Saturated Collapsible Rock," *Mechanics of Cohesive-Frictional Material*, Vol. 2, (1997), pp.251-278.

- Papike, J. J., S. B. Simon, and J. C. Laul, "The Lunar Regolith: Chemistry, Mineralogy, and Petrology," *Reviews of Geophysics and Space Physics*, Vol. 20, (1982), pp. 761-826.
- Parker, R. A., B. C. Gahan, R. M. Graves, S. Batarseh, Z. Xu, and C. B. Reed, "Argonne National Laboratory Laser Drilling: Effects of Beam Application Methods on Improving Rock Removal," *The SPE Annual Technical Conference and Exhibition*, Denver, Colorado, USA, SPE 84353, (October 5-8, 2003).
- Paterson, M. S. and T. F. Wong, *Experimental Rock Deformation – The Brittle Field*, 2nd Edition, Springer-Verlag, Berlin, (2005), p. 347.
- Paul, B. and D. L. Sikarskie, "A Preliminary Model for Wedge Penetration in Brittle Materials," *Transactions of the American Institute of Mine Engineers*, Vol. 232, (1965), pp. 373-383.
- Paul, B. and M. D. Gangal, "Why Compressive Loads on Drill Bits Produce Tensile Splitting in Rock," SPE 2392, (1969).
- Peng, S. S., "A Note on the Fracture Propagation and Time-Dependent Behaviour of Rocks in Uniaxial Tension," *International Journal of Rock Mechanics, Mining Science & Geomechanics Abstract*, Vol. 12, (1975), pp. 125-127.
- Phillips, D. W., "Tectonics of Mining," *Colliery Engineering*, Vol. 25, (1948), pp. 199-202.
- Pixton, D. and D. Hall, "Advanced Mud Hammer Systems," DOE project #DE-FC26-97FT34365, Novateck Inc., Provo, UT, USA, (2002).
- Plumb, R. A., "Influence of Composition and Texture on the Failure Properties of Clastic Rock," *Proceedings of EUROCK'94*, (1994), pp. 13-20.
- Podio, A. and K. E. Gray, "Single-Blow Bit-Tooth Impact Tests on Saturated Rocks under Confining Pressure: I. Zero Pore Pressure," *SPE Journal*, SPE 1056, (September 1965), pp. 211-225.
- Pollard, D. D. and R. C. Fletcher, *Fundamentals of Structural Geology*, Cambridge University Press, Cambridge UK, (2005), p. 500.
- Pratt, C. A., "Modifications to and Experience with Percussion Air Drilling," *The SPE/ IADC Drilling Conference*, New Orleans, Louisiana, USA, SPE/IADC 16166, (March 15-18, 1987).
- Priest, S. D., and S. Selvakumar, "The Failure Characteristics of Selected British Rocks," *Transport and Road Research Laboratory Report*, (1982).
- Raaen, A. M., K. A. Hovern, H. Jøranson, and E. Fjær, "FORMEL: a Step Forward in Strength Logging," *The SPE Annual Technical Conference and Exhibition*, Denver, Colorado, USA, SPE 36533, (October 6-9, 1996).
- Rabinowicz, E., *Friction and Wear of Materials*, Wiley, New York, (1965).
- Rao, K. S., G. V. Rao, and T. Ramamurthy, "Strength of Sandstones in Saturated and Partially Saturated Conditions," *Geotechnical Engineering*, Vol. 18, No. 1, (June 1987), pp. 99-127.
- Reichmuth, D. R., "Correlation of Force-Displacement Data with Physical Properties of Rock for Percussive Drilling Systems," *Rock Mechanics*, Ed. Fairhurst, C, Pergamon Press, Oxford, (1963), pp. 33-60.
- Ren, N. K., and J. C. Roegiers, "Differential Strain Curve Analysis - A New Method for Determining the Pre-existing In situ Stress State of Rock Core Measurements," *Proceedings of the 5th International Conference of the International Society of Rock Mechanics*, Melbourne, Australia, F117-F127, (1983).
- Reuss, A., "Berechnung der Fließgrenze von Mischkristallen auf Grund der Plastizitätsbedingung für Einkristalle," *Z. Angew. Math. Mech.* 9, (1929), pp. 49-58.

- Richard, T., C. Germy, and E. Detournay, "A Simplified Model to Explore the Root Cause of Stick-Slip Vibration in Drilling Systems with Drag Bits," *Journal of Sound and Vibration*, 305(3), (2007), pp. 432-456.
- Richard, T., *Determination of Rock Strength from Cutting Tests*, Master's thesis, University of Minnesota, (1999).
- Ridgeway, R. R., A. H. Ballard, and B. L. Bailey, "A Revised Mohs Hardness Scale," *Transactions of the Electrochemical Society*, Vol. 63, (1933), p 267.
- Roberts, A., *Applied Geotechnology – A Text for Students and Engineers on Rock Excavation and Related Topics*, Pergamon Press, (1981).
- Ruistuen, H., L. W. Teufel, and D. Rhett, "Influence of Reservoir Stress Path on Deformation and Permeability of Weakly Cemented Sandstone Reservoirs," *SPE Annual Technical Conference and Exhibition*, Denver, Colorado, USA, SPE 36535, (October 6-9, 1996).
- Samuel, G. R., "Percussion Drilling...Is It a Lost Technique? A Review," *The Permian Basin Oil & Gas Recovery Conference*, Mildland, Texas, USA, SPE 35240, (March 27-29, 1996).
- Santarelli, F. J. and E. T. Brown, "Failure of Three Sedimentary Rocks in Triaxial and Hollow Cylinder Compression Tests," *International Journal of Rock Mechanics and Mining Sciences*, Vol. 26, No. 5, (1989), pp. 401-413.
- Santarelli, F. J. and E. T. Brown, "Performance of Deep Wellbores in Rock with a Confining Pressure-Dependent Elastic Modulus," *Proceedings of the 6th International Congress on Rock Mechanics*, Montreal, II, (1987), pp. 1217-1222.
- Sarda, J. P., N. Kessler, E. Wicquart, K. Hannaford, and J. P. Deflandre, "Use of Porosity as a Strength Indicator for Sand Production Evaluation," *68th SPE Annual Technical Conference*, Houston, Texas, USA, SPE 26454, (October 3-6, 1993).
- Schlumberger manual, *Log Interpretation Principles/Applications*, Schlumberger Educational Services, Houston, Texas, (1987).
- Schmitt, L., T. Forsans, and F. J. Santarelli, "Shale Testing and Capillary Phenomena," *International Journal of Rock Mechanics, Mining Sciences and Geomechanics*, Vol. 31, No. 5, (1994), pp. 411-427.
- Schubert, H., "Capillary Forces – Modelling and Application in Particulate Technology," *Powder Technology*, Vol. 47, (1984), pp. 105-116.
- Simmons, G. and W. F. Brace, "Comparison of Static and Dynamic Measurements of Compressibility of Rocks," *Journal of Geophysical Research*, Vol. 70, (1965), pp. 5649-5656.
- Simon, R., "Transfer of Stress Wave Energy in the Drill Steel of a Percussive Drill to the Rock," *Journal of Rock Mechanics and Mining Science*, Vol. 1, (1964), pp. 397-411.
- Sinor, A. and T. M. Warren, "Drag Bit Wear Model," *SPE Drilling Engineering*, (June, 1989), pp. 128-136.
- Smith, F. W. and W. Kopczynski, "Oilfield Percussion Drilling," *The 32nd Annual California Regional Meeting of SPE*, Bakerfield, California, USA, SPE 222, (November 2-3, 1961).
- Smorodinov, M. I., E. A. Motovilov, and V. A. Volkov, "Determinations of Correlation Relationships between Strength and Some Physical Characteristics of Rocks," *Proceedings of the 2nd Congress of the International society for Rock Mechanics*, Vol. 2, No. 3-6, (1970), pp. 35-37.
- Somerton, W. H., A. Timur, and D. H. Gray, "Stress Behavior of Rock under Drilling Loading Conditions", *The 36th Annual SPE Fall Meeting*, Dallas, Texas, USA, SPE 166, (October 8-11, 1961).

- Surkov, Y. A., V. L. Barsukov, L. P. Moskalyeva, L. P. Moskaleva, V. P. Kharyukova, and A. L. Kemurdzhian, "New Data on the Composition, Structure, and Properties of Venus Rock Obtained by Venera 13 and Venera 14," Proceedings of the 14th Lunar and Planetary Science Conference, (1984), pp. 393-402.
- Swolfs, H. S., "Chemical Effects of Pore Fluids on Rock Properties, Underground Waste Management and Environmental Implications," Proceedings of the Symposium of American Association of Petroleum Geologists (AAPG), Memoir 18, (December 6-9, 1971), pp. 224-233.
- Taylor, G. I., "Stability of a Viscous Liquid Contained Between Two Rotating Cylinders," Philosophical Transactions of the Royal Society of London, A223, (1923), pp. 289-343.
- Taylor, G. J., R. D. Warner, and K. Keil, "Stratigraphy and Depositional History of the Apollo 17 Drill Core," Proceedings of the 10th Lunar and Planetary Science Conference, (1979), pp. 1159-1184.
- Taylor, J. M., "Pore Space Reduction in Sandstone," Bulletin of American Association of Petroleum Geology, Vol. 34, (1950), pp. 701-716.
- Tibbitts G. A., R. C. Long, B. E. Miller, A. Judzis, and A. D. Black, "World's First Benchmarking of Drilling Mud Hammer Performance at Depth Conditions," the IADC/SPE Drilling Conference, Dallas, Texas, USA, IADC/SPE 74540, (February 26-28, 2002).
- Tixier, M. P., G. W. Loveless, and R. A. Anderson, "Estimation of Formation Strength from the Mechanical-Properties Log," Journal of Petroleum Technology, Vol. 27, No. 3, SPE 4532, (March 1975), pp. 283-293.
- Tokle, K., P. Hosrud, and R. K. Bratli, "Predicting Uniaxial Compressive Strength from Log Parameters," 61st SPE Annual Technical Conference and Exhibition, New Orleans, Louisiana, SPE 15645, (October 5-8, 1986).
- Topanelian, E. Jr., "Effect of Low Frequency Percussion in Drilling Hard Rock," The SPE 32nd Annual Meeting, Dallas, TX, USA, AIME 1957, (October 6-9, 1957).
- Treadway, C., "Percussion and Down-The-Hole Hammer Drilling: Yesterday and Today," Water Well Journal, Vol. 51, No.7, (1997), pp.55-59.
- Tronvoll, J. and E. Fjær, "Experimental Study of Sand Production from Perforation Cavities," Investigation of Cavity Failures for Sand Production Prediction, University of Trondheim, Trondheim, Norway, (August 1993), pp.92-106.
- Vaniman, D. T., T. C. Labotka, J. J. Papike, S. B. Simon, and J. C. Laul, "The Apollo 17 Drill Core: Petrologic Systematics and the Identification of a Possible Tycho Component," Proceedings of the 10th Lunar and Planetary Science Conference, (1979), pp. 1185-1227.
- Villaescusa, E., M. Seto, and G. Baird, "Stress Measurements from Oriented Core," International Journal of Rock Mechanics & Mining Sciences, Vol. 39, (2002), pp. 603-615.
- Voigt, W., *Lehrbuch der Kristallphysik*, Teubner, Leipzig, (1910).
- Walsh, J. B. and W. F. Brace, "Cracks and Pores in Rocks," Proceedings of the 1st Congress of International Society of Rock Mechanics, Vol. 1, Lisbon, (1966), pp. 643-646.
- Wanamaker, J. A., "Rotary Percussion Drilling in West Texas," World Oil, (September 1951), pp. 182-187.
- Wang, Y. and M. B. Dusseault, "Borehole Yield and Hydraulic Fracture Initiation in Poorly Consolidated Rock Strata – Part II Permeable Media," International Journal of Rock Mechanics, Mining Science & Geomechanics Abstracts, Vol. 28, No. 4, (1991), pp. 247-260.

- Wang, Y. and M. B. Dusseault, "A Coupled Conductive-Convective Thermo-Poroelastic Solution and Implications for Wellbore Stability," *Journal of Petroleum Science and Engineering*, Vol. 38, No. 3-4, (2003), pp. 187-198.
- Warren, T. M. and W. K. Armagost, "Laboratory Drilling Performance of PDC Bits," *SPE Drilling Engineering*, (June 1988), pp. 125-135.
- Warren, T. M. and M. B. Smith, "Bottomhole Stress Factor Affecting Drilling Rate at Depth," *Journal of Petroleum Technology*, SPE 13381, (1985), pp. 1523-1533.
- Watters, T., *Planets: Smithsonian Guides*, Ligature, Inc., New York, (1995).
- West, G., "Effect of Suction on the Strength of Rock," *Quarterly Journal of Engineering Geology*, Vol. 27, (1994), pp.51-56.
- Whiteley, M. C. and W. P. England, "Air Drilling Operations Improved by Percussion-bit/Hammer-tool Tandem," *SPE Drilling Engineering*, SPE 13429, (October 1986), pp. 377-382.
- Wills, P. B., (and 8 others), "Active and Passive Imaging of Hydraulic Fractures," *The Leading Edge*, Vol. 11, No. 7, (July 1992), pp. 15-22.
- Yang, J. H. and K. E. Gray, "Single-Blow Bit-Tooth Impact Tests on Saturated Rocks under Confining Pressure: II. Elevated Pore Pressure," *Society of Petroleum Engineering Journal*, SPE 1702, (December 1967), pp. 389-409.
- Zacny, K., and G. Cooper, "Coring Basalt Rock under Simulated Martian Atmospheric Conditions," *Mars Journal*, Mars 3, (2007), pp. 1-11.
- Zarnecki, J. C., M. R. Leese, B. Hathi, A. J. Ball, A. Hagermann, M. C. Towner, R. D. Lorenz, J. A. M. McDonnell, S. F. Green, M. R. Patel, T. J. Ringrose, P. D. Rosenberg, K. R. Atkinson, M. D. Paton, M. Banaszkiwicz, B. C. Clark, F. Ferri, M. Fulchignoni, N. A. L. Ghafoor, G. n. Kargl, H. Svedhem, J. Delderfield, M. Grande, D. J. Parker, P. G. Challenor, and J. E. Geake, "A Soft Solid Surface on Titan as Revealed by the Huygens Surface Science Package," *Nature*, Vol. 438, (2008), pp. 792-795.
- Zarnecki, J. C., M. R. Leese, J. R. C. Garry, N. Ghafoor, and B. Hathi, "Huygens' Surface Science Package," *Space Science Reviews*, Vol. 104, (2002), pp. 593-611.
- Zoback, M. D, *Reservoir Geomechanics*, Cambridge University Press, Cambridge UK, (2007). p. 449.

2.7.1 Internet links

- Meyer, C., Lunar Sample Compendium, Apollo 17 samples 70001-70009, on-line resource <http://www-curator.jsc.nasa.gov/lunar/compendium.cfm>, accessed May 2008.
- Tempel 1, http://www.nasa.gov/mission_pages/deepimpact/main/index.html, (May 25, 2008).
- The International Society for Rock Mechanics lists many suggested methods for testing of rock. The American Society for Testing Materials also has established standards for rock and soils testing. Both these societies support refereed journals that publish articles related to rock testing.
- International Society of Rock Mechanics. <http://www.isrm.net/>. ASTM Geotechnical Testing Journal and Standards, <http://www.astm.org>.
- The following commercial sites are of interest. Also, many universities around the world have excellent testing facilities for petroleum rock mechanics.
- <http://www.sintef.no/>
- <http://www.terratek.com/>
- <http://www.corelab.com/PetroleumServices/Advanced/RockMech.asp>

<http://www.reslab.com>
<http://www.metarocklab.com>
<http://www.csiro.au/science/RockMechanicsTesting.html>